



Personalised 3D electromechanical models of the heart for cardiac resynchronisation therapy planning in heart failure patients

Gaëtan Desrues

► To cite this version:

Gaëtan Desrues. Personalised 3D electromechanical models of the heart for cardiac resynchronisation therapy planning in heart failure patients. Modeling and Simulation. Université Côte d'Azur, 2023. English. NNT : 2023COAZ4030 . tel-04220830

HAL Id: tel-04220830

<https://theses.hal.science/tel-04220830>

Submitted on 28 Sep 2023

HAL is a multi-disciplinary open access archive for the deposit and dissemination of scientific research documents, whether they are published or not. The documents may come from teaching and research institutions in France or abroad, or from public or private research centers.

L'archive ouverte pluridisciplinaire **HAL**, est destinée au dépôt et à la diffusion de documents scientifiques de niveau recherche, publiés ou non, émanant des établissements d'enseignement et de recherche français ou étrangers, des laboratoires publics ou privés.



THÈSE DE DOCTORAT

Modélisation électromécanique 3D personnalisée du cœur
pour la planification de la thérapie de resynchronisation
chez les patients en insuffisance cardiaque

Gaëtan DESRUES

INRIA, Équipe EPIONE

Thèse dirigée par Dr Maxime SERMESANT

Soutenue le 28 mars 2023

Présentée en vue de l'obtention du grade de DOCTEUR EN AUTOMATIQUE, TRAITEMENT
DU SIGNAL ET DES IMAGES de l'UNIVERSITÉ CÔTE D'AZUR.

Devant le jury composé de :

Pr Joakim SUNDNES	Simula Research Laboratory	Rapporteur
Pr Martyn NASH	University of Auckland	Rapporteur
Dr Serge CAZEAU	MicroPort CRM, Hôpital Saint-Joseph	Examineur
Dr Maxime SERMESANT	Inria Université Côte d'Azur	Directeur de thèse
Dr Delphine FEUERSTEIN	MicroPort CRM	Examineur
Dr Hervé DELINGETTE	Inria Université Côte d'Azur	Examineur

PHD THESIS

Personalized 3D electromechanical models of the heart
for cardiac resynchronisation therapy planning
in heart failure patients

Gaëtan DESRUES

INRIA, EPIONE Team

Supervised by Dr Maxime SERMESANT

Defended on March 28, 2023

Presented to obtain the title of DOCTEUR EN AUTOMATIQUE, TRAITEMENT DU SIGNAL ET
DES IMAGES of the UNIVERSITÉ CÔTE D'AZUR.

Jury:

Pr Joakim SUNDNES	Simula Research Laboratory	Reviewer
Pr Martyn NASH	University of Auckland	Reviewer
Serge CAZEAU MD	MicroPort CRM, Hôpital Saint-Joseph	Examiner
Dr Maxime SERMESANT	Inria Université Côte d'Azur	Supervisor
Dr Delphine FEUERSTEIN	MicroPort CRM	Examiner
Dr Hervé DELINGETTE	Inria Université Côte d'Azur	Examiner



Abstract

Heart failure is the final funnel of all cardiac diseases, currently affecting 8% of the general population living in developed countries and is expected to reach 11% by 2030. Despite major improvements provided by optimization of medical therapy and prevention, this disease still has a high mortality rate and represents 1-2% of the total medical expenses. Among the different new treatments that became available in the last years, Cardiac Resynchronization Therapy (CRT) has emerged as a very original technique used to correct mechanical abnormalities in these hearts, by direct stimulation of the myocardium in selected locations. Since the early times of CRT, identification of dyssynchrony has been based on the duration of the ventricular electrical activation (QRS) measured on a standard electrocardiogram (ECG) by the clinician. However, more advanced evaluation models may allow for a better understanding of the cause of dyssynchrony and therefore the ability to adapt the therapy to patient-specific conditions. For instance, recent scientific advances in mathematical modelling and numerical simulation nowadays allow us to develop personalized models of the patient cardiac function, as well as the use of patient data to describe dyssynchrony and predict the response to CRT.

This thesis describes the feasibility of a novel approach to use a digital twin in order to predict the response to CRT. The biophysical heart model is personalized from patient data measured in clinical routine using fast artificial intelligence (AI)-based methods, and the output simulation results are compared to clinical data provided by a cardiac devices manufacturer.

Briefly, we first propose a modelling work that allows us to construct a generic heart model including a three-dimensional mesh of the anatomy, the electrophysiological activity, as well as the complex dynamics of the heart through biomechanical models. This generic model is then personalized to the patient's health data: phenotype, echocardiography, ECG and haemodynamic measures. Next, an original method based on the optimization of a reduced model is proposed, allowing us to parameterise our digital twin. Finally, we have defined a stimulation protocol from the personalized model in order to study the response to CRT, and the *in silico* predictions of electromechanical measures are compared to patient data for different pacing configurations.

Overall, the work described in this thesis substantially contributes to the development of advanced non-invasive digital twin technologies that can be translated into routine clinical diagnostic and treatment planning procedures in order to increase the positive outcome and effectiveness of CRT (potentially resulting in slower progression towards advanced heart failure), and ultimately improving the quality of life of a large patient population.

Keywords: patient-specific simulation, digital twin, ECG, CRT, cardiac electrophysiology, biomechanics, finite element method, artificial intelligence.

Résumé

L'insuffisance cardiaque est la finalité de toutes les maladies cardiaques. Elle touche aujourd'hui 8% de la population générale vivant dans les pays développés et devrait atteindre 11% d'ici 2030. Malgré les améliorations majeures apportées par l'optimisation des thérapies et de la prévention, cette maladie a toujours un taux de mortalité élevé et représente 1 à 2% des dépenses totales dans le secteur de la santé. Parmi les différents nouveaux traitements disponibles ces dernières années, la thérapie de resynchronisation cardiaque (CRT) est apparue comme une technique très originale utilisée pour corriger certaines anomalies mécaniques de ces cœurs défaillants, par stimulation directe du myocarde dans des zones précises. Depuis les débuts de la CRT, l'identification de la désynchronisation est basée sur la durée de l'activation électrique ventriculaire (QRS) mesurée sur un électrocardiogramme (ECG) standard par le clinicien. Cependant, des modèles d'évaluation plus avancés permettent de mieux comprendre la cause de la désynchronisation et donc d'adapter le traitement. Les récentes avancées scientifiques en matière de modélisation mathématique et de simulation numérique permettent désormais de développer des modèles personnalisés de la fonction cardiaque du patient et d'utiliser les données cliniques pour décrire la désynchronisation et prédire la réponse à la thérapie de resynchronisation.

Cette thèse évalue la faisabilité de l'utilisation d'un jumeau numérique pour prédire la réponse à la thérapie de resynchronisation cardiaque. Le modèle est personnalisé à partir des données de routine des patients en utilisant des méthodes rapides basées sur l'IA. Les résultats sont comparés aux données cliniques fournies par un fabricant de dispositifs cardiaques. Un premier travail de modélisation permet de construire un modèle cardiaque générique incluant un maillage tridimensionnel de l'anatomie, l'activité électrophysiologique, ainsi que la dynamique complexe du cœur à travers des modèles biomécaniques. Ce modèle générique est ensuite personnalisé sur les données de santé du patient : morphologie, échocardiographie, ECG et mesures hémodynamiques. Une méthode basée sur l'optimisation d'un modèle réduit est proposée et permet de rapidement paramétrer le jumeau numérique. Enfin, nous avons mis en place un protocole de stimulation à partir du modèle personnalisé afin d'étudier la réponse à la thérapie de resynchronisation. Les prédictions des mesures électromécaniques sont comparées aux données des patients pour différentes configurations de stimulation.

Dans l'ensemble, les travaux décrits dans cette thèse contribuent au développement de technologies non-invasives avancées de jumeau numérique qui peuvent être utilisées pour le diagnostic clinique et la planification des traitements de santé afin d'augmenter

les résultats positifs et l'efficacité de la CRT, et finalement améliorer la qualité de vie d'une large population de patients.

Mots-clés: simulation personnalisée, jumeau numérique, ECG, CRT, électrophysiologie cardiaque, biomécanique, éléments finis, intelligence artificielle.

Acknowledgments

Financial Support

This work has been supported by the French government through the National Research Agency (ANR) Investments in the 3IA Côte d'Azur (ANR-19-P3IA-000) and by Microport CRM funding.

List of acronyms

AI	Artificial Intelligence
AV	Atrioventricular
BBB	Bundle Branch Block
BiV	Bi-Ventricular
CG	Conjugate Gradient
DCM	Dilated cardiomyopathy
DC	Diastolic Contraction [ms]
DOF	Degrees Of Freedom
EAT	Electrical Arrival Time [ms]
ECG	Electrocardiogram
EF	Ejection Fraction [%]
FEM	Finite Element Method
FPK	First Piola-Kirchhoff [Pa]
HPC	High Performance Computing
IVD	Interventricular Delay
IsoC	Isovolumetric Contraction [ms]
IsoR	Isovolumetric Relaxation [ms]
LAFB	Left Anterior Fascicle Block
LBbB	Left Bundle Branch Block
LHS	Latin Hypercube Sampling
LLW	Left Lateral Wall
LPEI	Left Pre-Ejection Interval [ms]
LPFB	Left Posterior Fascicle Block
LVET	Left Ventricle Ejection Time [ms]
LVFW	Left Ventricle Free Wall
MI	Myocardial Infarction
ML	Machine Learning
MVC	Mitral Valve Closure
ODE	Ordinary Differential Equation
Overlap	Overlap between onset of E wave and end of DC [ms]
PDE	Partial Differential Equation

PMJ Purkinje-Muscle Junction
QRSa QRS axis [°]
QRSd QRS duration [ms]
QRS-A Duration between start of QRS and end of A wave [ms]
QRS-E Duration between start of QRS and onset of E wave [ms]
RBBB Right Bundle Branch Block
RHS Right Hand Side
RPEI Right Pre-Ejection Interval [ms]
RVET Right Ventricle Ejection Time [ms]
RVOT Right Ventricular Outflow Tract
SA Sinoatrial
SD Systole Duration [ms]
SegC Segment Contraction [ms]
Sept Septal
SOFA Simulation Open Framework Architecture
SPK Second Piola-Kirchhoff [Pa]
WK Windkessel model

Contents

Abstract	v
Acknowledgments	ix
Financial Support	xi
List of acronyms	xiii
1 Introduction	1
1.1 Clinical context	1
1.1.1 The heart's function	2
1.1.2 Heart failure	10
1.1.3 Dyssynchrony	11
1.1.4 Cardiac Resynchronization Therapy (CRT)	12
1.2 Patient-specific cardiac modelling	12
1.2.1 Why building patient-specific models of the heart ?	12
1.2.2 Introduction to the IPRC project	13
1.3 Presentation of the datasets	14
1.3.1 Anatomies	14
1.3.2 ECGs dataset	15
1.3.3 Microport CRM dataset	15
1.4 Outline of the manuscript and contributions	17
2 Anatomical model	19
2.1 Input data	20
2.1.1 Meshing	21
2.1.2 Building a deformation model	22
2.1.3 From surface meshes to masks	24
2.2 Building the anatomical data	25
2.2.1 Local cardiac coordinates system	25
2.2.2 Cardiac fibers	26
2.2.3 AHA regions segmentation	27
2.2.4 Purkinje network generation	27
2.2.5 Conclusion	31

3	Electrophysiology model	33
3.1	Propagation of the electrical depolarization wave	35
3.1.1	A conduction model for the heart tissue	35
3.1.2	Conduction velocity	37
3.2	Fast model for 12-lead ECG generation	38
3.2.1	The heart as bioelectric source	38
3.2.2	Modelling the action potential	39
3.3	Signal processing on the ECG	40
3.3.1	ECG signal processing pipeline	40
3.3.2	QRS axis determination	43
3.4	Calibration of the electrophysiological model	44
3.4.1	Healthy and dilated geometries	44
3.4.2	Sensitivity analysis on the electrical parameters	46
3.5	Pathological simulations	52
3.5.1	Simulating bundle branch blocs	52
3.5.2	Simulating fascicular blocks	53
3.5.3	Simulating ischemia	53
3.5.4	Discussion	53
3.6	Pacing simulation	54
3.6.1	Cardiac stimulation and defibrillation	54
3.6.2	Implementation of cardiac stimulation	55
3.6.3	Simulating CRT	58
3.7	Conclusion	59
4	Electromechanical model	61
4.1	Solid mechanics	63
4.1.1	Lagrangian description of the finite strain theory	63
4.1.2	Elasticity theory	64
4.1.3	Balance equations	65
4.1.4	Weak formulation	65
4.1.5	Discretization of the weak formulation	66
4.1.6	Implicit integration scheme	68
4.2	Implementation in a simulation framework	70
4.2.1	Introduction to SOFA	70
4.2.2	Implementation's strategy	71
4.2.3	Biophysical material law	72
4.2.4	Active contraction	74
4.2.5	Heamodynamics	76
4.2.6	Constraint-based implementation of the valves system	78
4.2.7	Boundary conditions	80
4.2.8	Conclusion	81
4.3	Results	83

4.3.1	Normal heart	83
4.3.2	DCM with LBBB	85
4.3.3	Mechanical simulation of the CRT	85
4.3.4	Sensitivity analysis	86
4.3.5	Discussion	88
4.3.6	Computation time and influence of the discretization	89
5	Personalization of the electromechanical model	93
5.1	Personalization methods	95
5.1.1	Features extraction and dimension reduction	95
5.1.2	Personalized parameters	99
5.1.3	CMA-ES	102
5.1.4	Implementation of the optimization on a cluster	103
5.1.5	Regression with machine learning methods	103
5.2	Personalization of the model	106
5.2.1	Anatomical personalization	106
5.2.2	Electrophysiological personalization	106
5.2.3	Mechanical personalization	107
5.3	Prediction of the therapy response	108
5.3.1	Description of the protocol	108
5.3.2	Results	109
5.3.3	Discussion	110
6	Conclusions	113
6.1	Contributions	113
6.2	Models limitations	114
6.3	Further improving the computation time	116
6.3.1	Frame-based method	116
6.3.2	Physic-based deep learning	118
6.4	Conclusion	118
	Appendices	119
A	Differentiation of the biomechanical material laws	119
A.1	Material laws	119
A.1.1	Guccione material law	119
A.1.2	Fung material law	120
A.1.3	Mooney-Rivlin material law	120
A.2	Automatic differentiation	121
B	Mechanical model computations	123
B.1	Constraint-based implementation of the Windkessel 3-element model in SOFA	123

B.2	Volume's derivatives on an open mesh	125
B.3	Rotation of base vectors	126
B.4	Notations and tensor operations	127
B.4.1	Second order tensor	127
B.4.2	Forth order tensor	128
B.4.3	Tensor operations	128
Bibliography		131

Introduction

1.1	Clinical context	1
1.1.1	The heart's function	2
1.1.2	Heart failure	10
1.1.3	Dyssynchrony	11
1.1.4	Cardiac Resynchronization Therapy (CRT)	12
1.2	Patient-specific cardiac modelling	12
1.2.1	Why building patient-specific models of the heart ?	12
1.2.2	Introduction to the IPRC project	13
1.3	Presentation of the datasets	14
1.3.1	Anatomies	14
1.3.2	ECGs dataset	15
1.3.3	Microport CRM dataset	15
1.4	Outline of the manuscript and contributions	17

1.1 Clinical context

Heart failure is a progressive cardiac condition characterized by the inability of the heart to provide a cardiac output adapted to the needs of the body. Eventually, the heart fails to provide a cardiac output adapted to body's needs, leading to death. At the beginning symptoms may be absent, but later appear during exercise and further at rest, defining the traditionally functional classes (NYHA). Heart failure induces an increase of the pressures of the cardio-vascular system responsible for specific symptoms (dyspnea), and altered functional capacities. At the end, death occurs either by pump failure or sudden cardiac death (arrhythmia). Symptoms may vary, and have been deeply modified by the successive recent pharmacological advances. They include breathlessness, fatigue, pain or dizziness. Several underlying pathologies can cause heart failure including cardiomyopathy, coronary heart disease or arrhythmia.

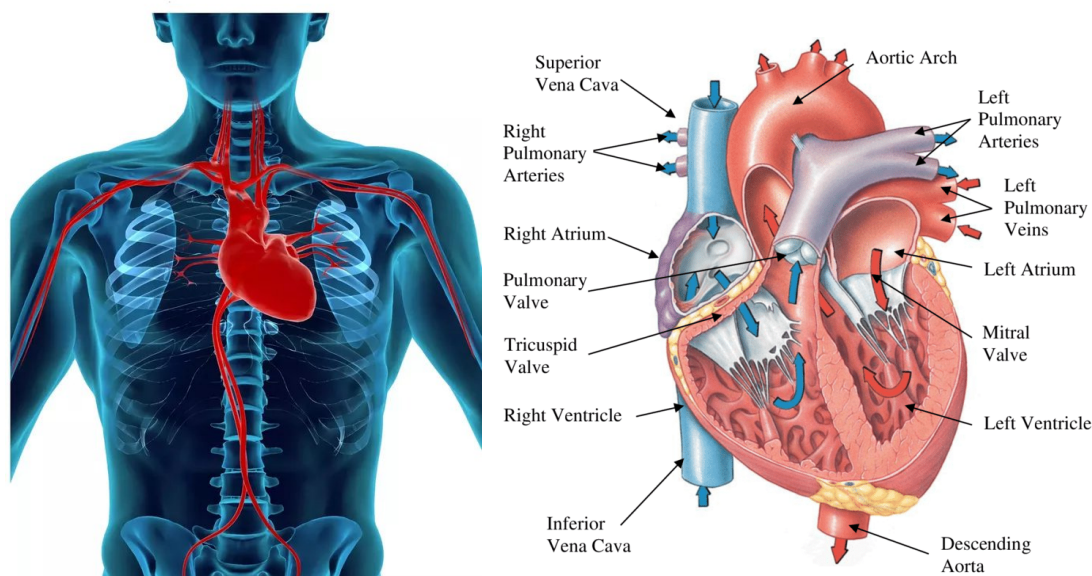
This thesis focuses on electromechanical dyssynchrony induced by abnormalities in the propagation of electrical activation within the myocardium in these altered hearts. This dyssynchrony is then at least partly responsible for the pump inefficiency. Despite the efforts of CRT to alleviate heart failure symptoms and improve mortality, approximately

30% of treated patients are non-responders. Patient selection, leads placement and device tuning are not sufficiently optimized due to the lack of understanding of the underlying physiological phenomena.

1.1.1 The heart's function

Anatomy

The heart is a muscular organ and beats continuously to pump blood in order to provide oxygen and nutriment to the body. All mammals have a four-chambered heart with



(a) Position of the heart in the human body. (b) Anatomy of the heart.

Fig. 1.1.: Position and anatomy of the human heart.

two ventricles and two atria. In the human body, it is located between the two lungs, slightly behind and to the left of the sternum. Its longitudinal axis is oblique downwards, forwards and to the left. The left lung is slightly smaller to make room for the heart in the left chest.

Generally, the adult heart weighs about $300 \pm 50\text{g}$ and beats approximately 70 times per minute, 100 000 times per day or 2.5 billion in a lifetime [Shaffer et al., 2014]. In the adult heart, the mean length is $12 \pm 2\text{cm}$ and width $8 \pm 2\text{cm}$ [Mohammadi et al., 2016].

Cardiovascular system

The human circulatory system is a closed circuit, in which the blood travels through veins and arteries. It is supplied by the left ventricle, ejecting blood through the aortic valve and the aorta. The oxygenated blood coming from the lungs arrives in the left atrium

through the pulmonary veins, and enters the left ventricle. After the oxygenated blood is consumed, the deoxygenated blood returns to the heart and enters the right atrium through the inferior and superior vena cava. The right atrial contraction fills up the right ventricle, which empties itself in the pulmonary arteries, leading to the lungs. The oxygenated blood coming from the lungs arrives in the left atrium through the pulmonary veins, and enters the left ventricle. The heart's contraction causes both ventricles to eject blood, and the cycle repeats itself.

The blood's circulation inside the heart is controlled by several valve orifices, surrounded by fibrous collagen [Hinton et al., 2011]. The mitral and tricuspid atrioventricular (AV) valves separate the atria from the ventricles, while the aortic and pulmonary semilunar valves separate the ventricles from the great arteries.

Histology

Cardiac muscle (or myocardium) makes up the thick middle layer of the heart, see Fig. 1.2, and is located between the endocardium and the epicardium [Saxton et al., 2021]. It consists of two types of cells: cardiac muscle cells (cardiomyocytes) and fibroblast. Cardiomyocytes function will be described in section 1.1.1, they are the cells responsible for the heart contraction.

A fibroblast is a type of cell that contributes to the formation of connective tissue, a fibrous cellular material that supports and connects other tissues or organs in the body. It synthesizes the extracellular matrix and the collagen protein, which helps maintain the structural framework of tissues.

False tendons are fibrous, fibrous-muscle or muscle structures, variable in length and thickness, found in the left ventricular (LV) cavity, generally located between the free wall of the left ventricle or a papillary muscle and the interventricular septum, without connection to the mitral valves.

Pericardium

The heart is located in a thin fibroelastic envelope called the pericardium and consisting in three layers: the fibrous, the visceral and the parietal pericardium, see Fig. 1.2.

1. The outer layer, the fibrous pericardium, provides support and protection for the heart, it connects to the diaphragm, the sternum and the vertebral column [Rehman et al., 2021].
2. The parietal pericardium is mainly composed of collagen, offering high extensibility at low levels of stress with an abrupt transition to relative inextensibility at higher stress, due to the shortening of collagen bundles.

3. The visceral layer of the serous pericardium is called the epicardium and delimits the myocardium [Watkins et al., 1993].

The pericardial cavity contains fluids necessary to lubricate the heart during the contraction.

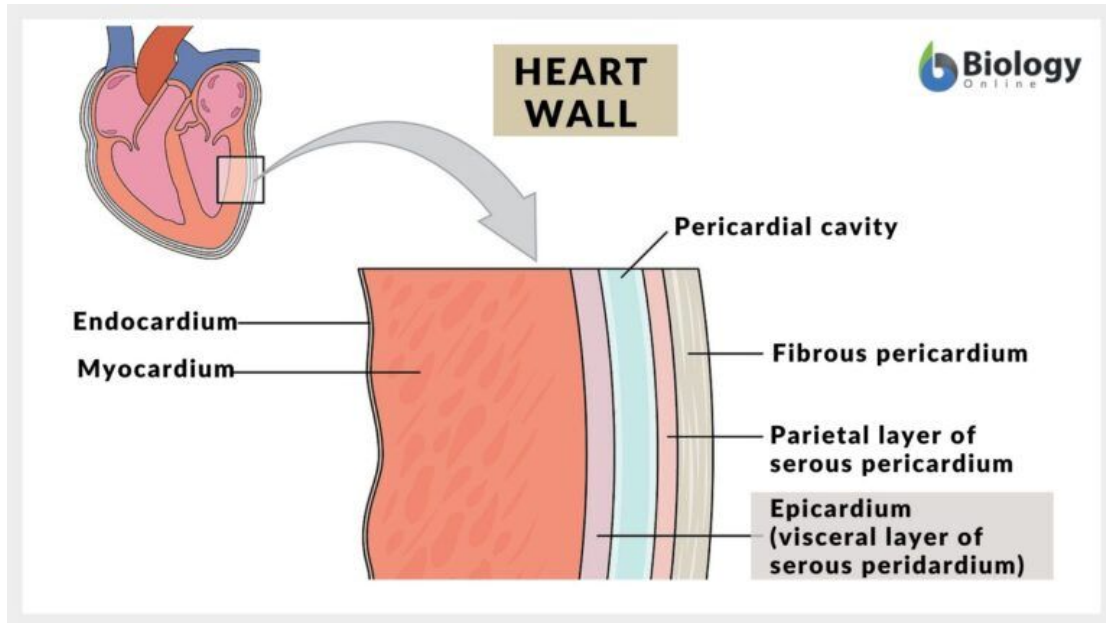


Fig. 1.2.: The three layers of the heart wall. Source: BiologyOnline.com.

Conduction system

The cardiomyocytes contraction is activated by electrical activity. Achieving a coordinated biatrial and biventricular contraction greatly depends on the signal propagation throughout the heart.

Cardiac cells, like all living cells in the body, exhibit an electrical potential across the cell membrane (namely, a transmembrane potential). The resting potential is approximately -90mV. The electrical potential is determined by the concentration of ions across the membrane, which shows varying permeability to each of the ions, mostly potassium (K^+), sodium (Na^+) and calcium (Ca^{2+}). Ions cross the membrane through specialized ions channels, which can be opened or closed. The membrane potential regulates the voltage-gated channels and allows for ions movement [Hodgkin et al., 1952], and for cells' contraction, see section 1.1.1.

In cardiac physiology, an action potential occurs when the membrane potential of a cell rapidly depolarizes and then repolarizes back to its resting state. We can distinguish two types of cardiac action potential:

- non-pacemaker action potentials are triggered by depolarizing currents from adjacent cells. Individual myocytes are joined together by low-resistance gap junctions located at the intercalated disks, and for this reason the ionic currents can flow between two adjoining cells. When these ionic currents (i.e., moving ions through gap junctions) are sufficient to rapidly depolarize the adjacent cell above its threshold potential, an action potential is elicited in the second cell, and so on.
- pacemaker cells are capable of spontaneous action potential generation.

Cells within the sinoatrial (SA) node, located within the posterior wall of the right atrium, constitute the primary pacemaker site within the heart. When a depolarisation occurs, the electrical signal propagates through the atria, leading to its contraction. Because atria and ventricles are electrically isolated from each other by connective tissue, the atria depolarisation does not directly affect the ventricles. The electrical signal is conducted to the atrioventricular (AV) node, located at the lower back section of the interatrial septum, near the opening of the coronary sinus. It then enters the ventricles through the bundle of His and is further separated into the left and right bundle branches. More distally the bundles ramify into Purkinje fibers and finally enters the myocardium through

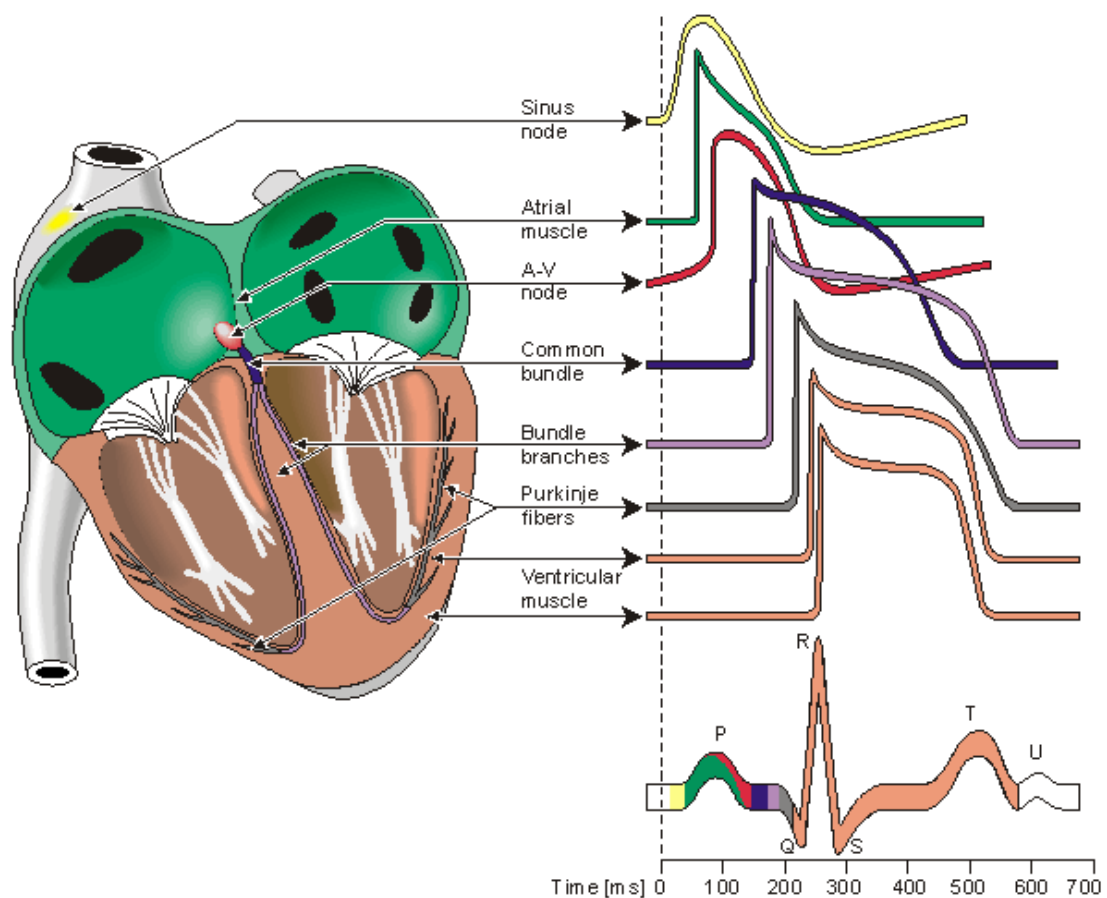


Fig. 1.3.: Potential at the specialised cells of the heart. Source: [Malmivuo et al., 1995].

Purkinje-muscle junction points. His bundle branches and Purkinje fibers are part of the fast conduction network, they transmit the signal between 2 and 4 m/s [Malmivuo et al., 1995; Sahli Costabal et al., 2016].

While most of the Purkinje network is located subendocardially, it is known that some Purkinje bundle are free running, without being attached to the ventricle surface. Such cells can be found in the false tendon, see Fig. 1.4b and [Cha et al., 2020; Boyden et al., 2010; Martinez et al., 2018; Hwang et al., 2011].

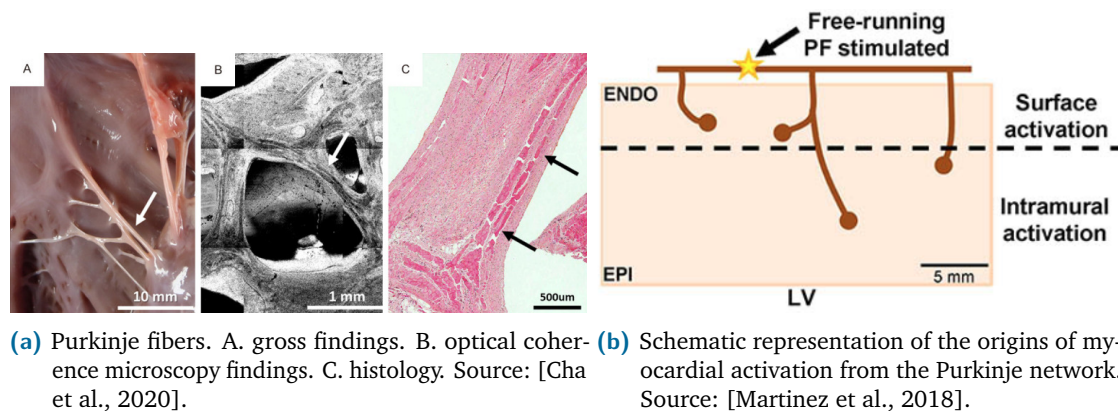


Fig. 1.4.: Evidence of free-running Purkinje fibers.

Cardiomyocytes

Cardiomyocytes are connected muscular cells responsible for the contractile force of the heart, see Fig. 1.5. The contraction-relaxation cycle of cardiomyocytes is regulated by the varying ions concentration, mainly Ca^{2+} ions [Kosta et al., 2021].

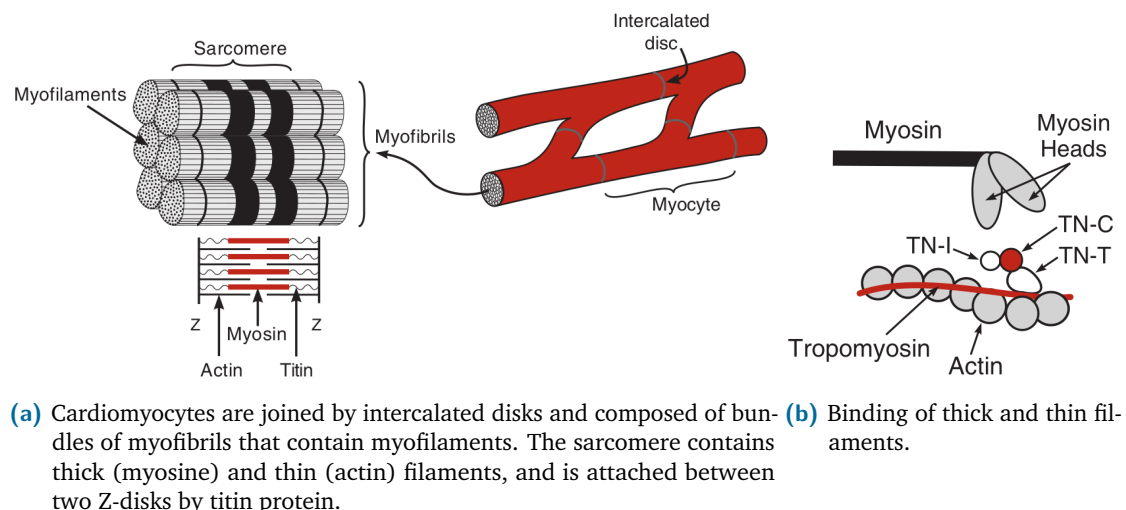


Fig. 1.5.: Structure of the sarcomere and force generation process. Adapted from [Klabunde, 2012].

Electrocardiogram

The electrocardiogram (ECG) is a recording of the heart's electrical activity, measured using ten electrodes placed on the torso. It captures the small electrical changes throughout the cardiac cycle, conveying a large amount of information about the structure of the heart and the conduction system.

The ECG signals are traditionally recorded on standard paper travelling at a rate of 25mm/s. The paper is divided into large squares, each measuring 5mm wide (which is typically equivalent to 0.2s). Each large square has five small squares within its width, and each small square is 1mm wide (i.e. equivalent to 40ms). ECG recordings provide important information concerning electrical activation of the heart (pattern, duration) related to potential diseases.

Besides duration, an important measure that can be extracted from the ECG is the QRS axis, (see Fig. 1.6), which represents the sum of depolarisation vectors generated by individual cardiac myocytes. Several calculation methods are possible, either from the ECG wave or from the activation map. Since it identifies the mean electrical depolarisation path, it can give a preliminary determination on the heart's condition, see section 3.3.2.

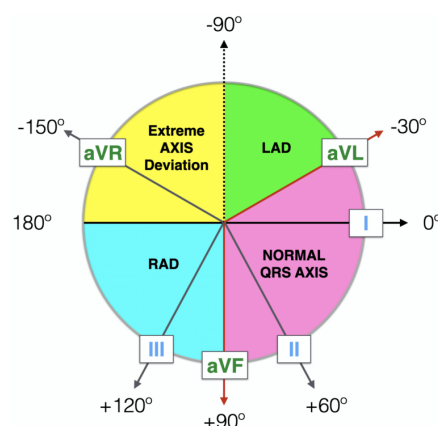


Fig. 1.6.: Abnormal QRS axis can indicate an underlying pathology.

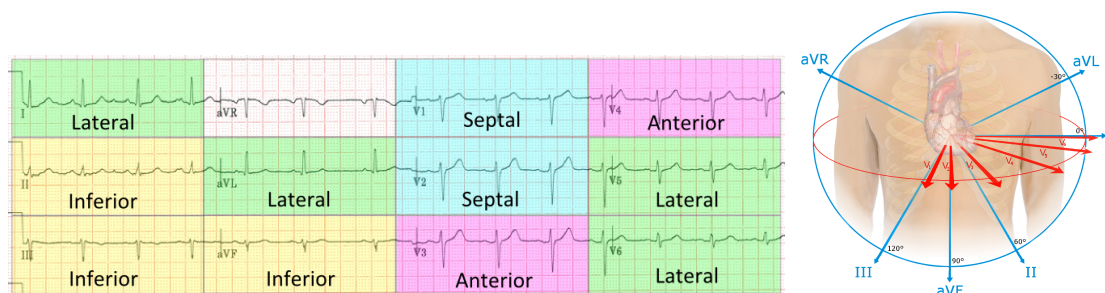


Fig. 1.7.: ECG leads and heart axis.

The six chest leads (V1 to V6) record the electrical activity of the heart in the horizontal plane, see Fig. ???. The information from the limb electrodes is combined to produce the six limb leads (I, II, III, aVR, aVL, and aVF), corresponding to the vertical plane of the heart. The information from these 12 leads is combined to form a standard electrocardiogram Fig. ???. A normal ECG wave from a healthy subject is presented in Fig. 1.8, characterized by a width of the QRS interval certainly shorter than 120ms (ideally close to 80ms).

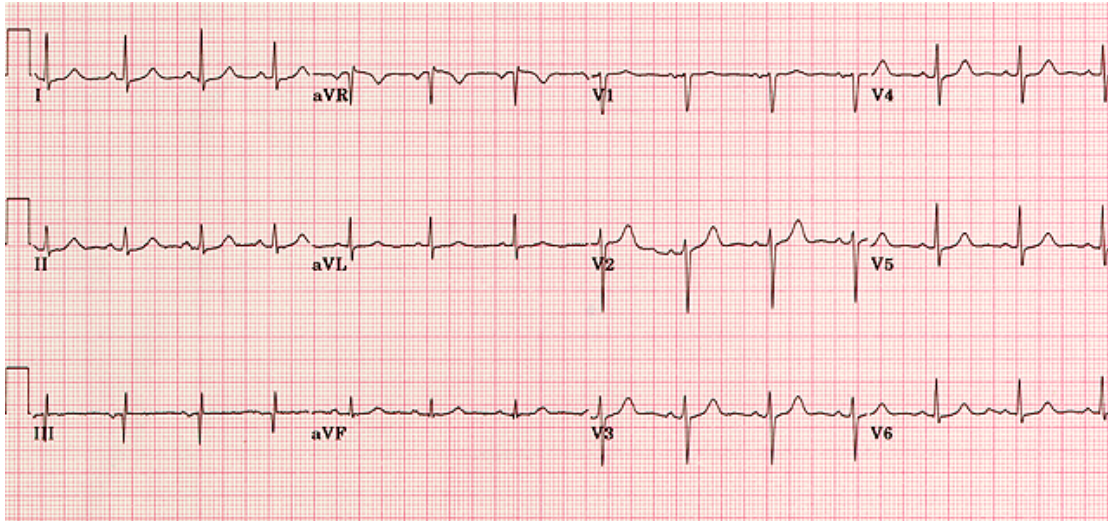


Fig. 1.8.: Normal ECG. Sinus rhythm; QRS width $\approx 80\text{ms}$; QRS axis $\approx +30^\circ$; small septal Q waves in I, aVL, V6; large S wave in V1-V2 which transitions to large R wave in V4-V6. Source: https://elentra.healthsci.queensu.ca/assets/modules/ts-ecg/normal_ecg.html.

The cardiac cycle

The primary function of the heart is to pump blood throughout the body, delivering nutrients and removing wastes from each organ. It consists in two major phases: the diastole when the heart muscle relaxes and fills with blood, and the systole, when it contracts and ejects blood to the arteries and the cardiovascular system (Fig. 1.9).

We can define four distinct phases, which repeat about 100 000 times a day: filling, isovolumetric contraction, ejection, and isovolumetric relaxation. Initially, the ventricles fill with blood from the atria. The atria then contract and push blood into the ventricles. The valves between the atria and ventricles close, creating the first sound of a heartbeat, and the ventricles contract. The pressure in the ventricles increases until it exceeds the pressure in the arteries, causing the valves in the arteries to open. Blood is then expelled into the arteries, and the pressure decreases as the ventricles relax. When the pressure in the ventricles drops below the pressure in the arteries, the valves in the arteries close, creating the second sound of a heartbeat, and the relaxation phase begins. The process then repeats, with the atria filling the ventricles once more.

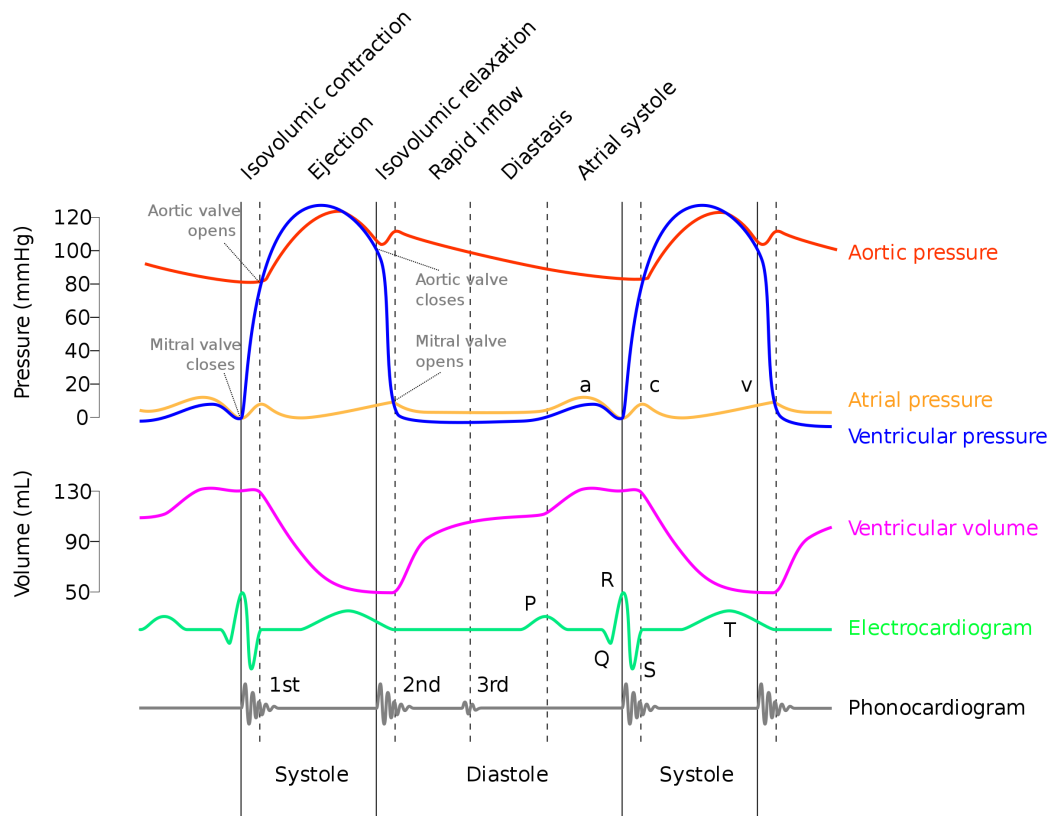


Fig. 1.9.: A Wiggers diagram illustrates events and details of the cardiac cycle. The ventricular diastole, or relaxation, begins with the isovolumic relaxation phase, then proceeds through three sub-stages of inflow, namely: rapid inflow, diastasis, and atrial systole. During the diastole, the ventricular volume increases, beginning at the aortic valve closing and ending after the atrial filling phase. The ventricular systole (i.e., the contraction), begins with the isovolumic contraction when the AV valve closes. It ends after the ejection phase, when the aortic valve closes. During the ejection, the ventricular volume decreases to its least amount as the ventricles pump blood to the pulmonary arteries and to the aorta. Source: Wikimedia Commons.

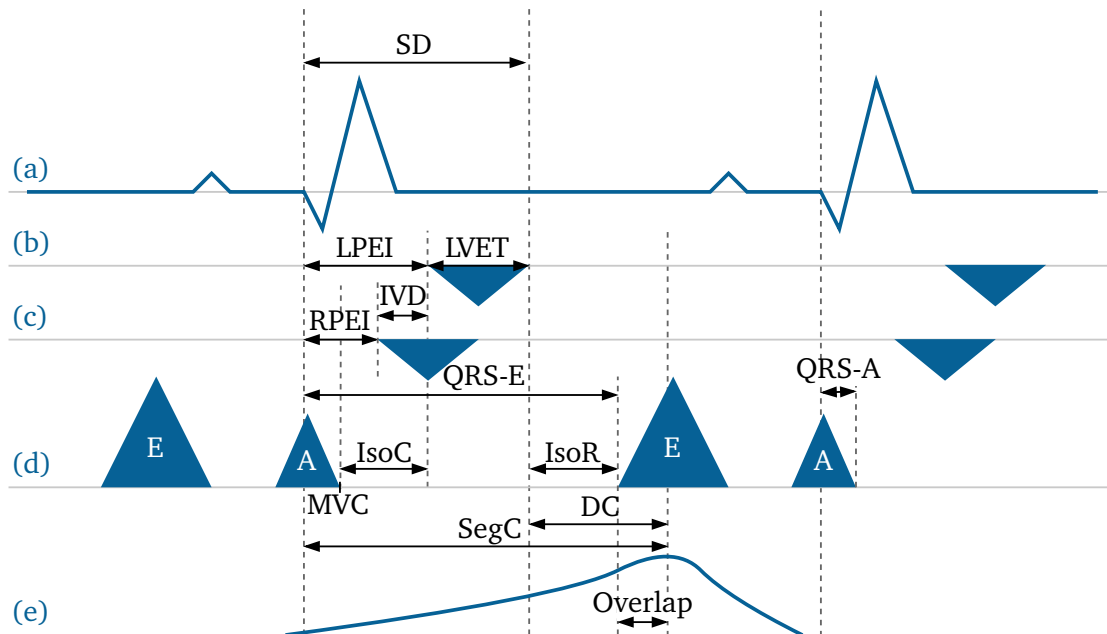


Fig. 1.10.: Introduction to notations with a schematic cardiac cycle.

1.1.2 Heart failure

Heart failure is a syndrome in which the heart is unable to pump enough blood to meet the body's needs for oxygen and nutrients. The condition can be classified as either systolic or diastolic heart failure, depending on whether the problem is with the heart's pumping ability (systolic) or its capability to fill with blood (diastolic). The New York Heart Association (NYHA) functional classification is a system used to categorize the degree of functional impairment a person with heart failure may have, see Table 1.1. This index is clinically determined based on the patient's self-reported symptoms during ordinary physical activity.

Diastolic heart failure, also known as heart failure with preserved ejection fraction (HFpEF), is a type of heart failure in which the heart's ability to be filled is altered and decreased, but the systolic function is normal. Impaired relaxation function of the myocardium may be due to stiffer myocardial tissue, for example in the case of hypertrophic cardiomyopathy with increased fibrosis. It may also come from a diminished capacity to restore a low resting Ca^{2+} during the isovolumetric relaxation phase [Morgan et al., 1990].

The contraction of the ventricles can also be defective during systole, leading to a decreased stroke volume. It can be caused by a reduced contractility of the cardiac muscle, either locally (e.g. due to myocardial infarction) or globally (e.g. for example in the case of dilated cardiomyopathy). Other electrophysiological disorders can lead to a failing heart, such as dyssynchrony.

Class	Functional capacity
I	Patients with cardiac disease but without resulting limitation of physical activity. Ordinary physical activity does not cause undue fatigue, palpitation, dyspnea, or anginal pain.
II	Patients with cardiac disease resulting in slight limitation of physical activity. They are comfortable at rest. Ordinary physical activity results in fatigue, palpitation, dyspnea, or anginal pain.
III	Patients with cardiac disease resulting in marked limitation of physical activity. They are comfortable at rest. Less than ordinary physical activity causes fatigue, palpitation, dyspnea, or anginal pain.
IV	Patients with cardiac disease resulting in inability to carry on any physical activity without discomfort. Symptoms of heart failure may be present even at rest. If any physical activity is undertaken, discomfort is increased.

Tab. 1.1.: The 1994 New York Heart Association (NYHA) Classification system. Source: [Bennett et al., 2002].

1.1.3 Dyssynchrony

Dyssynchrony is a condition in which the segments of the heart do not contract in harmony (i.e. simultaneously), leading to a reduced ejection fraction. Such condition can classically be observed on the ECG recordings displaying a prolonged QRS duration, although dyssynchrony is much more complex and involves mechanical and hemodynamical mechanisms.

From an electro-mechanical view, dyssynchrony can be modelled in three different types:

- **Atrioventricular (AV) dyssynchrony**

AV dyssynchrony results in a reduction of the filling duration. Classically, it is due to delayed conduction through the AV node due to a first-degree AV Block. The result is a reduced ventricular diastolic filling with the summation of the protodiastolic component of filling (E wave on doppler examination) and end diastolic component (A wave) due to atrial contraction. It results in a decreased LV preload that jeopardizes stroke volume (due to the failure of the Starling mechanism). Another mechanism responsible for AV dyssynchrony is IntraV dyssynchrony (cf further). Significant AV dyssynchrony potentially correctable by CRT is defined by a LV filling time (LVFT) indexed to R-R interval < 40% [CAZEAU et al., 2000; Serge, 2000].

- **Interventricular dyssynchrony**

Interventricular dyssynchrony describes an important delay in activation between the RV and the LV, resulting in a lack of coordinated contraction. Significant InterV

dyssynchrony is defined when the interval is greater than 40 ms [CAZEAU et al., 2000].

- **Intraventricular dyssynchrony**

Intraventricular dyssynchrony describes a delay within ventricle segment's propagation, resulting in delayed or slowed contraction. It is typically evaluated by M-mode, pulsed tissue Doppler, speckle tracking, or 3D echocardiography.

Intraventricular dyssynchrony may occur when the conduction system fails to deliver the electrical depolarisation signal to all segments of the ventricle. Rupture in the His bundle conduction system and branches or infarcted areas are possible causes of electrical intraventricular dyssynchrony. Definition varies according the authors. Some are focusing on delays measured between different segments, others focus on the amount of ventricular mass still contracting after the closure of the aortic valve, prolonging the duration of the systole, and therefore delaying the timing of the next E wave, resulting in a decrease on filling duration [Cazeau et al., 2000].

1.1.4 Cardiac Resynchronization Therapy (CRT)

The CRT procedure consists in the implantation of pacing leads that ensures an improvement in the coordination of the contraction of the cardiac muscle. Although this technique has been shown to be effective in some patients, it is difficult to predict the response to CRT in each patient due to individual variability in cardiac function and propagation. Observational data increasingly suggest that patients suffering from congestive heart failure in presence of modest QRS widening could also be benefiting from CRT but this has not been validated. With this respect, some patients can be significantly improved clinically after system implantation despite no apparent change in QRS width [Cazeau et al., 2019; GHIO, 2004].

1.2 Patient-specific cardiac modelling

1.2.1 Why building patient-specific models of the heart ?

Numerical simulation can be defined as a sequence of calculations performed on a computer, in order to solve complex solutions of mathematical models, that usually describe a physical system and its response after a perturbation. Building models for a particular application is a difficult task and requires a strong knowledge of the dynamical system. Their complexity depends largely on the studied system, and is directly linked to the ability of the model to represent the reality.

The heart is not only one of the most complex organ of the body, but also one of the most studied because of its vital functions. Having a sufficiently realistic cardiac simulation framework is a real opportunity for researchers, clinicians, or even the patients themselves. Understanding the cardiac function, in-silico trials, CRT device optimization, surgical planning, communication, research and development, are possible outcomes of patient-specific simulation.

Multinational industrial companies such as Philips, General Electric Healthcare or Dassault Systems (The Living Heart Project) are currently developing health digital twins to bring simulation into the clinical routine. Their modelling approaches are based on extremely detailed multi-scale observation of the heart function. However, while this procedure yields highly precise measures of the cardiac function, the simulations require tremendous hardware resources and computation time to run. Moreover, most of these models rely on highly accurate patient data, generally processed from expensive medical devices such as Magnetic Resonance Imaging (MRI), which is not a commonly used procedure for heart failure patients.

Our method, on the contrary, is based on low-cost routine patient data that is usually acquired during cardiologist examination, such as those from ECG or echocardiographic measurements. The models and methods developed in this thesis are focused on explainable parametrisation, limited computation time and resources, scalability and portability. The patient-specific simulation framework presented hereafter targets daily usage by clinicians on large cohort of patients, and its integration within a fully automatic pipeline.

1.2.2 Introduction to the IPRC project

In this thesis, clinical constraints are considered and evaluated from the beginning to build a complete modelling framework, compatible with clinical use. IPRC stands for Industrialization of Cardiac Resynchronization Personalization and is a global industrial project aiming at incorporating cardiac models and personalization methods into the clinical workflow. This project starts when a patient is diagnosed with heart failure (or more precisely cardiac dyssynchrony) and follows the treatment for several years after implantation of a CRT device, and its principal goal is to use routine non-invasive data to make fast patient-specific therapy predictions.

This thesis work is part of the long-term IPRC project, led by Microport CRM and focuses on bringing digital twins to the clinical world. The IPRC project is composed of five blocks, developed independently:

1. extraction of echographic numerical patient data: this is done by using specialized AI-based analysis of standard echocardiographic views,

2. automatic analysis of the data and stratification of heart failure patients via an heterogeneous database (INSERM Rennes),
3. personalization of a cardiac model to fit sinus rhythm patient data, prediction of the CRT leads implantation location (INRIA),
4. assistance to leads implantation using specific sensors and automatic device optimization,
5. long-term followup of cardiac remodelling, potentially linked to drug treatment and device programming optimization via a clinical followup application linked to the heterogeneous database and various others (CPAM, INSEE).

The third block of this project consists in the development of a cardiac digital twin and is presented in this manuscript. The output of the two preceding blocks (i.e. the patient data), is clearly identified and serves as input to this digital twin. The first objective of this thesis is to build a complete cardiac model, simple enough to be customized in a time compatible with the clinical constraints, and detailed enough to represent well the cardiac function of the patient. Once the electromechanical model has been personalized and validated against the patient known data, different stimulation configurations are considered, optimized and sent to the practitioner to plan the implantation of the leads.

1.3 Presentation of the datasets

Several datasets are used in this thesis, they come from different sources and were extracted with different modalities. Having good patient data is prevailing to build robust models by restricting the possible outcomes and build more accurate and realistic simulations of the cardiac function. Although the data is heterogeneous and no complete set of patient data was found, it is possible to aggregate this real-world data to assess the personalization of the model.

Note that since the machine learning algorithms developed in this thesis are focused on learning the relations between the input and the outputs of reduced representations of the model, they do not rely on these datasets but rather on simulated data, where both the parameters and the simulation's output were available.

1.3.1 Anatomies

The anatomical model presented in chapter 2 relies on a healthy biventricular template geometry that has been segmented from cine MRI by a Siemens Healthineers team with a combination of the methods described in [Wang et al., 2012] and [Jolly et al., 2012], as mentioned in [Mollero, 2017]. A dozen of these geometries were available but only one of them was manually corrected to serve as the template mesh. Pathological geometries can

then be generated with a deformation model, without losing the labels of the anatomical structures of this biventricular geometry, see section 2.1.2.

Moreover, a statistical shape model described in [Rodero et al., 2021] offers the possibility to generate realistic four-chamber heart models. Their publication is supplemented by one thousand meshes generated by their model. Although this data has not been used in this thesis, it provides a complete description of labelled anatomical meshes and could help in making realistic simulations.

1.3.2 ECGs dataset

The dataset that is used to calibrate the electrophysiology model presented in chapter 3 is composed of 827 ECG tracings from different patients, annotated by several cardiologists, residents and medical students [Ribeiro et al., 2020]. In addition to healthy cases, it contains six different ECGs abnormalities: 1st degree AV block, sinus bradycardia, atrial fibrillation, sinus tachycardia, Left Bundle Branch Block (LBBB) and Right Bundle Branch Block (RBBB). In this work we are only focusing on healthy and BBB cases, all other abnormalities are excluded. After processing these tracings and selecting only BBB, it remains 483 ECG. Based on the algorithms presented in section 3.3.1, QRS have been extracted and some measures are described in Tab. 1.2. The envelope of the QRS extracted from these tracings is presented in Fig. 1.11.

	Healthy	LBBB	RBBB
Count	459	8	16
QRSd [ms]	96.2 (3.0)	116.2 (17.2)	100.9 (2.2)
Axis iso [°]	36.3 (65.6)	22.5 (41.7)	5.6 (74.5)
Axis I-aVF [°]	-41.7 (24.9)	-30.3 (16.0)	-12.2 (49.3)
Axis I-III [°]	11.1 (44.5)	-26.1 (9.8)	-16.8 (67.7)

Tab. 1.2.: Computed values on the 483 ECG tracings extracted from the data provided by [Ribeiro et al., 2020]. Data given as ‘mean (std)’.

1.3.3 Microport CRM dataset

This dataset includes data from ninety patients undergoing CRT implantation, and is provided by Microport CRM. Measurements of electromechanical indices using echocardiography were made at five steps of the procedure, corresponding to different pacing configurations: entry (the presence or absence of an implanted stimulation device is indicated), RV stimulation, LV stimulation, standard BiV stimulation, Final BiV or triple site stimulation after optimization of leads placement. The final step is optionally a last stimulation configuration, referred as BiVOpt or TIV, for optimized CRT.

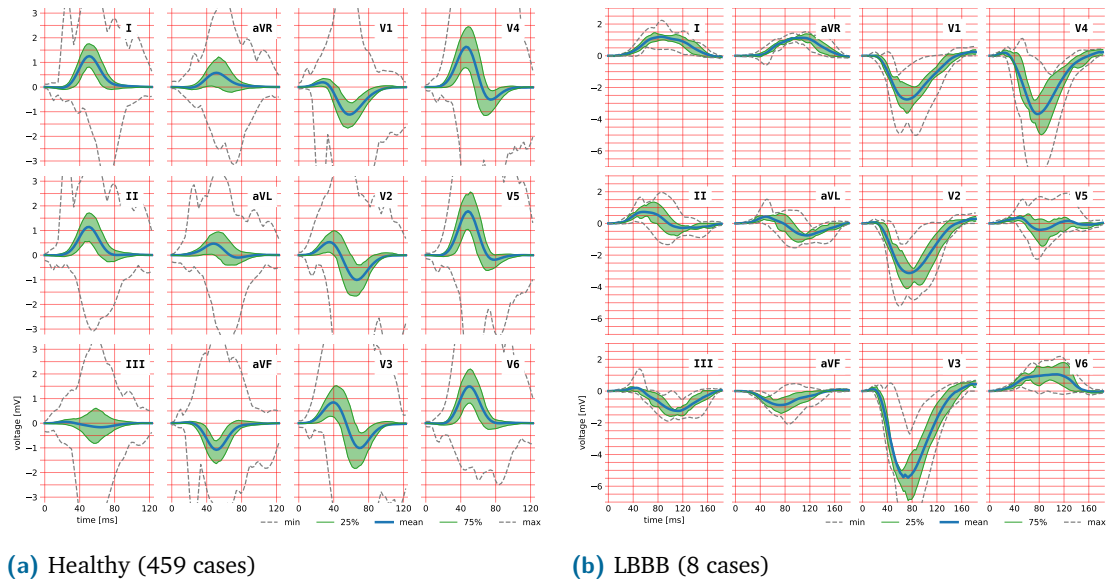


Fig. 1.11.: Envelope of the 12-lead recordings from [Ribeiro et al., 2020].

For each step of the implantation, for each pacing configuration, the following electromechanical indices are measured: R-R interval, Diastolic Filling Time (DFT), DFT ratio (percentage of filling as compared to R-R interval), QRS-E, RPEI, LPEI, InterV delay (IVD), Total Systole Duration (TSD), isovolumetric contraction duration (IsoC), isovolumetric relaxation duration (IsoR), left ventricular ejection time (LVET), $\frac{LPEI}{LVET}$, delay between the beginning of the QRS and the end of the atrial filling wave (QRS-endA), contraction times of the septum and left ventricle free wall (LVFW), diastolic contraction of the septum and LVFW as well as the overlap of these contractions (when the aortic and pulmonary valves are closed) and the delay of contraction between the septum and the LVFW. Additionally, the dataset also provides the areas of the mitral and tricuspid valves but are not used in this study. See Fig. 1.10 for a schematic representation of these indices.

	Entry	Final
Age [years]	70.6 (11.8)	
Sex	8 female (30.8%), 18 male	
EF [%]	27.8 (9.1)	38.2 (10.6)
QRS axis [°]	-32.3 (57.6)	-5 (122.3)
QRSd [ms]	172.7 (31.0)	150.4 (25.5)

Tab. 1.3.: Selection of 26 patients among the data provided by Microport CRM, with DCM and sinus rhythm. Data given as ‘mean (std)’.

1.4 Outline of the manuscript and contributions

The present manuscript follows the order of the realized works. First we describe the modelling of the heart's function, through the three following sub-models: anatomy, electrophysiology and biomechanics. Once the generic model has been implemented and calibrated both on healthy and pathological scenarios, the personalization methods and results are presented. Finally, the last part introduces the stimulation protocol and shows the prediction to CRT response results.

Contributions

Here are the main contributions of this PhD work with the corresponding sections in parenthesis:

- implementation of a semi-automatic labelling pipeline for input geometry using the ray-tracing method and anatomical prior knowledge (2.1),
- construction of a shape model and implementation of a personalized anatomical pipeline (2.1.2),
- electrical model for fast generation of the activation map, including Purkinje-based propagation, conduction disorders (BBB, ischemia), and pacing (3.1 and 3.6),
- implementation of the coupling between the Purkinje network and the activation map (3.6.2),
- fast and fully automatic ECG waves generation framework (3.2),
- new finite element implementation of the cardiac mechanical model, using SOFA (Simulation Open Framework Architecture), an open source framework primarily targeted at real-time physical simulation, with an emphasis on medical simulation (4.2),
- corrected formulation of the 3-element Windkessel model and implementation of the Crank-Nicolson numerical scheme within a constraint-based framework (4.2.5),
- personalization of the prediction to the resynchronization therapy response (chapter 5),
- producing a personalized modelling framework, suitable for various types of cardiac 3D simulations, including High Performance Computing (HPC) support (5.1.4),
- frame-based model order reduction formulation for cardiac mechanics (6.3.1).

Anatomical model

2.1	Input data	20
2.1.1	Meshing	21
2.1.2	Building a deformation model	22
2.1.3	From surface meshes to masks	24
2.2	Building the anatomical data	25
2.2.1	Local cardiac coordinates system	25
2.2.2	Cardiac fibers	26
2.2.3	AHA regions segmentation	27
2.2.4	Purkinje network generation	27
2.2.5	Conclusion	31

This chapter introduces two contributions, the first one being the development of a deformation model that is able to generate dilated and hypertrophic geometries. It relies on meaningful deformation modes for the selected cardiomyopathies and allows for fine-tuning of the geometrical properties such as septal thickness and the reduction of the RV due to the dilatation of the LV. Additionally, heterogenous meshing helps in optimizing the number of tetrahedra in the geometry.

The second contribution consists in the development of efficient algorithms related to the free-running Purkinje network. A robust generation method is derived from an existing implementation and allows to adapt the discretization of the network based on the curvature of the endocardial surface. Also, because the network's topology can be altered by BBB or myocardial infarction, the geodesic distance can be difficult to compute and a fast parallelized implementation is used.

Cardiac simulations are based on numerical methods that require the definition of a finite domain for subsequent computations. In this manuscript, several physiological structures are considered: the cardiac muscle is the main organ but some models require additional elements such as the pericardium and the torso. Each of these structures is described as a set of connected points lying in space, called a mesh. A mesh is a discretisation of a geometric domain into small simple shapes, such as triangles (2D) and tetrahedra (3D).

The anatomy of the patient’s heart is the first fundamental block needed when building patient-specific simulations. The biventricular myocardium can be extracted from non-invasive methods of 3D cardiac imaging such as MRI (which offers the best contrast but is generally expensive and time-consuming) and CT (which offers the best spatial sub-millimetric resolution, but uses ionizing radiation). The heart anatomy is extracted using segmentation algorithms, which are more and more available thanks to deep learning approaches.

However, myocardial segmentation methods still require highly tuned and performant algorithms in order to yield adequate results that are clinically acceptable, due to the complexity of the heart’s anatomy (trabeculae, right ventricle wall thickness, continuous motion, etc.). Furthermore, these methods are expensive and rarely used in clinical routine. In this framework we instead rely on a template biventricular mesh and use a shape model to deform the mesh and generate a new geometry, with required features such as ventricular volume or wall thickness.

Note that the atria are not included in our 3D model, but their interactions with the ventricles are modelled in different ways, see sections 3.1 and 4.2.7.

The anatomical model [Desrues, 2022b] is included in the `ELecModel` pipeline.

2.1 Input data

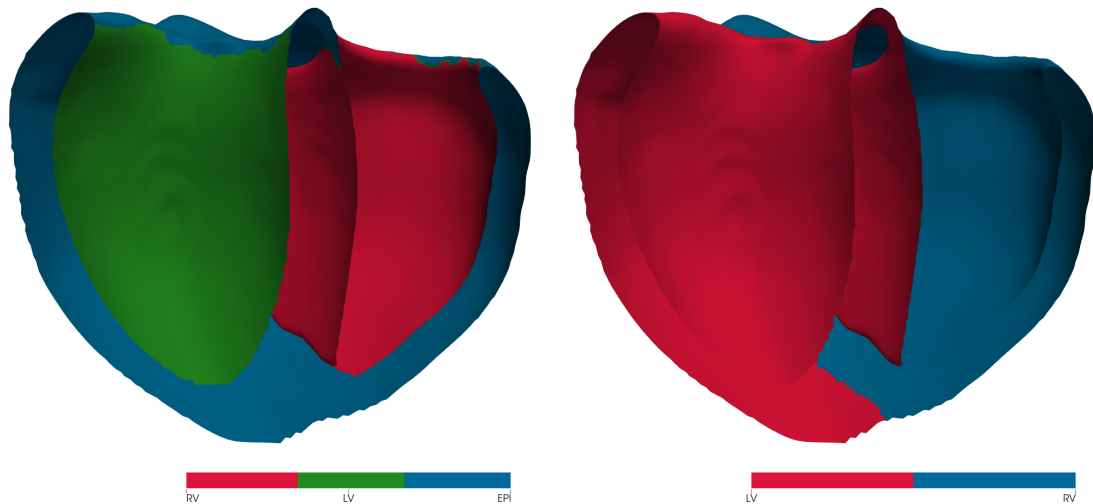


Fig. 2.1.: Required labels. Surface labels: endocardium and epicardium (left) and ventricular labels: left or right ventricle (right).

This section describes the minimal required data and the preprocessing pipeline to perform a 3D electromechanical simulation. Any mesh can be transformed into a polydata,

compatible with this framework. For example, the marching cubes algorithm [Lorensen et al., 1987] can be used to create a triangular surface from the 3D image extracted from the segmentation of medical images.

A polydata represents a geometric structure consisting of vertices, lines, polygons, and/or triangle strips [Schroeder et al., 2006a], it is associated with surface topologies. This surface polydata must be labelled as per Fig. 2.1, namely endocardium (RV in red, LV in green on the figure), epicardium (EPI, blue) and ventricular labels. The data can be stored on points (`vtkPointData`) or on cells (`vtkCellData`) ; the preferred file format is VTK [Schroeder et al., 2006b]. Several tools allow to manually (ParaView, pyvista) or semi-automatically (MeshObject) [Desrues, 2022a] segment the input polydata. Note that the septum on the right ventricle is labelled as left ventricle.

2.1.1 Meshing

Meshing a closed 3D surface mesh consists in dividing the inner volume of the polydata into multiple tetrahedral elements. Several solutions to generate tetrahedral meshes exist (gmsh, CGAL) but they do not yield sufficient results, see Fig. 2.2. We use MMG [Dobrzynski, 2012], an open source remesher, for all meshing operations.

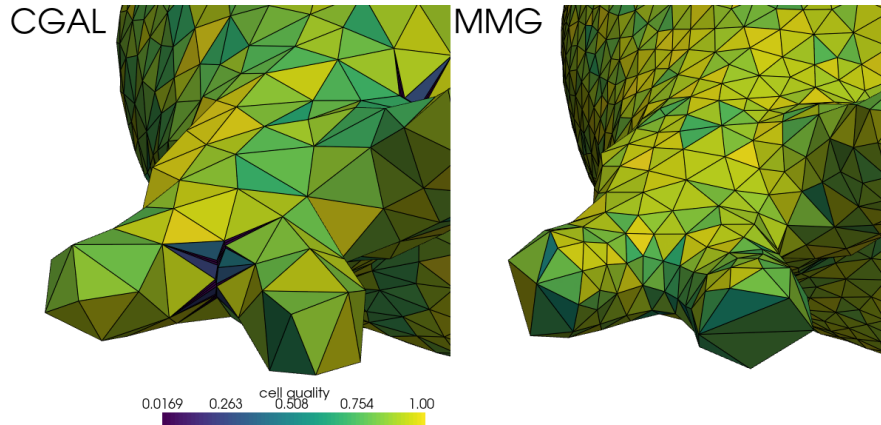


Fig. 2.2.: Comparison of surface triangular meshing results on an atrial mesh: CGAL introduces very small elements that are not present with the MMG remeshing. The color map indicates the quality of the elements with a scalar between zero (bad) and one (acceptable).

The MMG software allows us to pass in a tensor field, prescribing a length and a direction for the edges, so that the resulting meshes will be anisotropic. This feature is beneficial when working with heart meshes as the myocardium walls can be thin (up to 3mm [Kawel et al., 2012]) and too many small elements can be problematic. This is illustrated in Fig. 2.3: small elements are present on the thin right ventricle free wall but the edge length on the hypertrophic left ventricle is increased to have at least 3 elements in the cross-section, leading to 12% reduction in the number of tetrahedra compared to

isotropic meshing. Optimizing the number of elements is important to keep the size of the numerical systems to solve small.

Note that other types of elements do exist but are usually more complex to implement. Hexahedra are known to be more suitable for incompressibility and large-deformation hyperelasticity. See [Oliveira et al., 2016] for a comparison between tetrahedral and hexahedral meshes for finite element simulation of cardiac electro-mechanics. For the sake of simplicity and compatibility with available software, tetrahedral elements are preferred in this thesis.

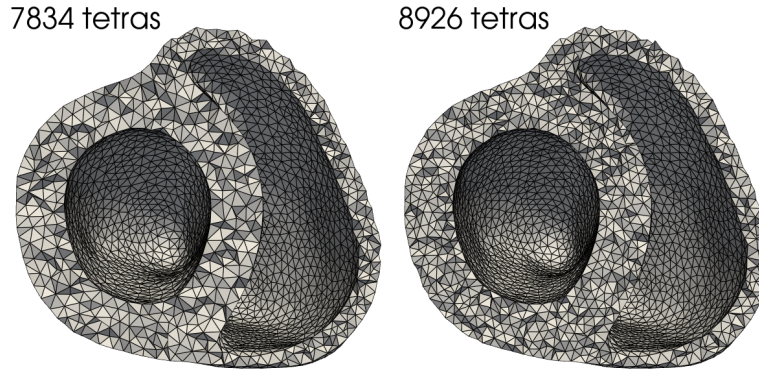


Fig. 2.3.: Anisotropic and isotropic meshing. By optimizing the number of cross-wall elements, the number of tetrahedra is reduced by 12% on the left.

2.1.2 Building a deformation model

In addition to the generated mesh, tools were developed to virtually modify the anatomy, in order to increase the number of healthy and pathological cases available, as well as to correct any inaccuracies from the segmentation method. As opposed to [Rodero et al., 2021] where deformation modes are found automatically, they are here defined based on meaningful deformations for the selected cardiomyopathies. This allows to parameterize the deformations with only three parameters: k_r and k_z control the radial and longitudinal scaling respectively while k_{dilate} controls both the thinning of the LV wall in case of DCM and its thickening in case of hypertrophy. The k_{dilate} deformation field is aligned with the LV radial directions, as shown in the first column of Fig. 2.4.

	V_{LV}	V_{RV}	AB dist.	Diameter	Sept. thick.
k_{dilate}	0.779 (0.0)	-0.686 (0.0)	0.193 (0.0)	0.758 (0.0)	-0.963 (0.0)
k_r	0.405 (0.0)	0.645 (0.0)	-0.013 (0.64)	0.500 (0.0)	0.035 (0.0)
k_z	0.242 (0.0)	0.319 (0.0)	0.970 (0.0)	0.003 (0.93)	-0.002 (0.95)

Tab. 2.1.: PRCC between parameters and the computed features. p -values are indicated in parentheses.

To account for the minimum wall thickness of 3mm mentioned in the previous section, the deformation is further scaled depending on the local wall thickness of the template mesh. This is visible on Fig. 2.4, the coefficient k_{dilate} is reduced near the LV apex, minimizing the effect of dilatation in these thin areas.

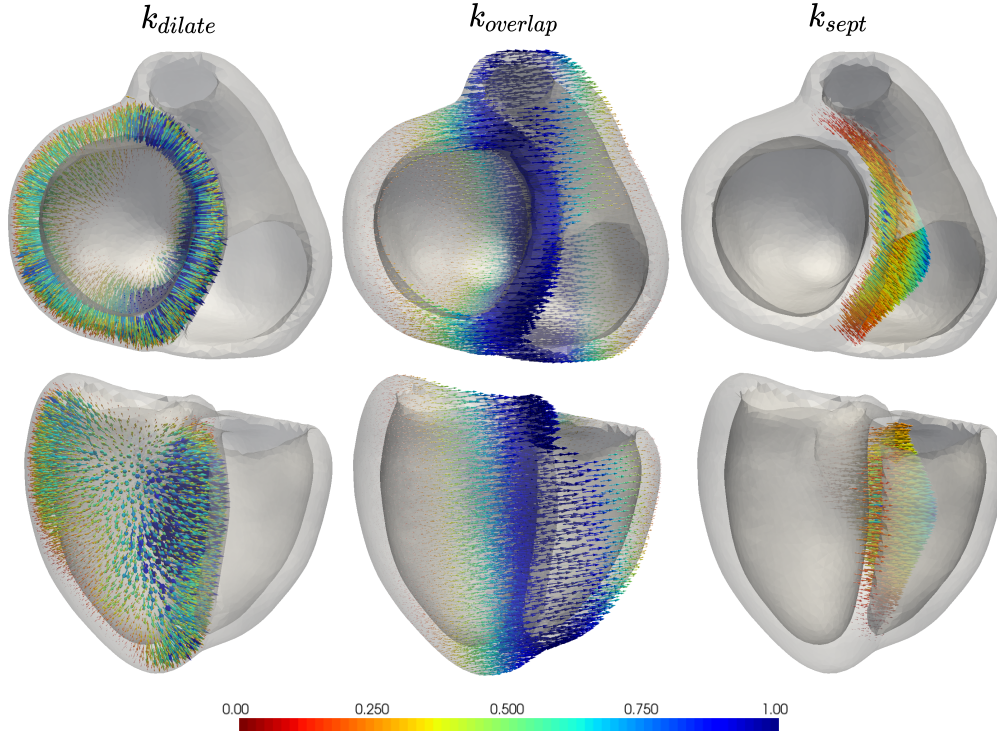


Fig. 2.4.: Deformation modes of the shape model. Left: dilatation of the left ventricle, modelling either hypertrophy (>0) or dilated (<0) cardiopathies). Center: septal overlap, allows to simulate the displacement of the dilated LV over the RV. Right: septal coefficient, controlling the thickness of the septum independently. The color bar indicates the norm of each vector in the deformation field.

To evaluate this model, two hundred sets of parameters have been sampled with the Latin Hypercube Sampling (LHS) method, in a parameter space representing both healthy, DCM and hypertrophic cases. The Partial Rank Correlation Coefficient (PRCC) method is then used to compute the correlation between the deformation model parameters and the computed features, as presented in Tab. 2.1. These correlation coefficients are effective measures to ensure that the model behaves correctly. For instance, the dilatation coefficient k_{dilate} is positively correlated with the LV volume and negatively correlated with the septal thickness. As the apicobasal distance is not influenced by radial deformations, the heart diameter and septal thickness are not impacted by longitudinal deformations. However, the fact that k_{dilate} is negatively correlated does not only comes from the dilatation deformation. Other deformations are to be considered but they are not parameterized directly.

Two other parameters can be defined to gain finer control on the septal deformation: $k_{overlap} = \alpha \max(0, k_{dilate})$ is used to enlarge the LV while overlapping the RV (keeping a

constant volume for both cavities, only available for DCM) ; and $k_{sept} = \beta \max(0, k_{dilate})$ which can be used to manage the thickness of the setpum. These deformation modes are also presented by the vector fields visible on Fig. 2.4, in the center and right panes. α is the overlap factor and β the septal mode coefficient. Best results were found using $\alpha = 2$ and $\beta = 0.5$ but these values could eventually be modified in a learning algorithm scenario to increase the number of generated geometries and their variability.

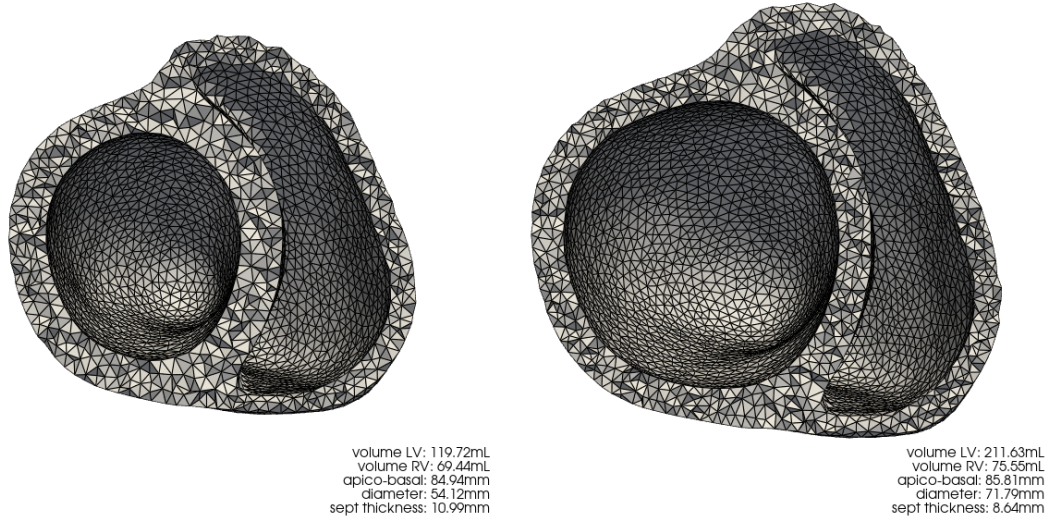


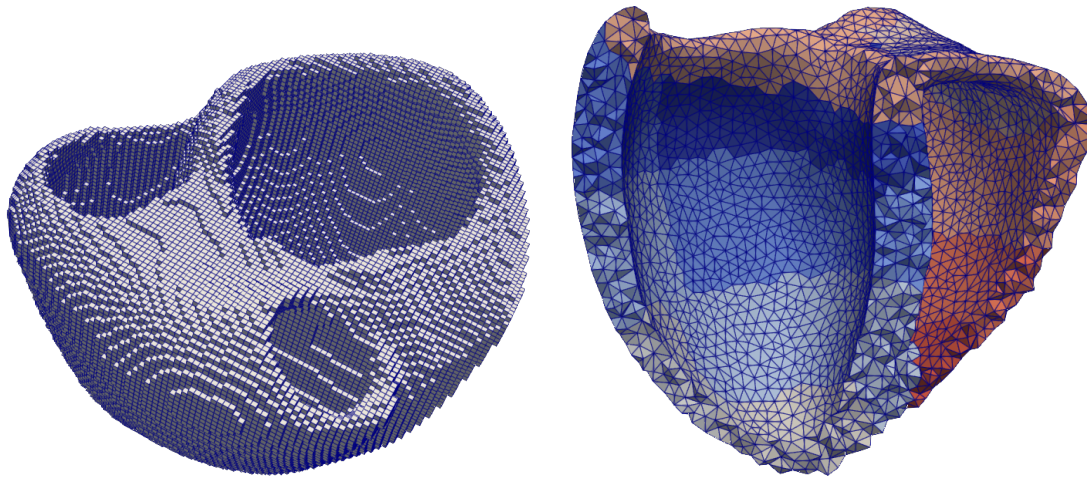
Fig. 2.5.: Normal (left) and dilated geometry (right).

An example of the mesh generated by the deformation model is presented in Fig. 3.1a, where the right ventricle volume has been reduced by 20%. Several pathological cases could be generated similarly from a healthy heart geometry, for example dilated (Fig. 2.5) or hypertrophic cardiomyopathies.

Other use of shape models have been reported, for example in [Lorenz et al., 2006] and [Pekar et al., 2001], shape models are used for the segmentation of cardiac images, adding an anatomical prior knowledge.

2.1.3 From surface meshes to masks

In the following example, the binary mask from the segmentation (Fig. 2.6a) is resampled into $1 \times 1 \times 1mm^3$ voxels and contains the labels for left and right ventricles. The labels for endocardium, myocardium and epicardium are built with a ray-tracing method, emerging from each ventricle barycentre. A tetrahedral mesh is built using the remeshing software MMG [Dapogny et al., 2014] (Fig. 2.6b), resulting in a mesh of approximately 90k tetrahedra and 20k vertices, respectively.



(a) Image extracted using the segmentation algorithms (\approx one million voxels). (b) Generated mesh ($\approx 90k$ tetrahedra).

Fig. 2.6.: Generated topologies.

2.2 Building the anatomical data

Now that we have a suitable tridimensional tetrahedral mesh and its corresponding uniform grid, the end of this chapter will be focused on computing the remaining structural and functional data, namely the local cardiac coordinates, the fibers orientation and the His-Purkinje conduction network.

2.2.1 Local cardiac coordinates system

Cardiac local coordinates are a system of reference used to describe the position and orientation of structures within the heart. The long-axis coordinate system is defined in each ventricle as the line connecting the apex to the center of the heart base. The second one is defined by the direction toward the other ventricle's barycenter in the transverse axis, forming an orthogonal basis at the barycenter of each cavity. The spherical cardiac coordinates are automatically found using the work from [Cedilnik, 2018], by fitting an ellipsoid to each endocardial surface. This approach is also used in the definition of AHA regions, Section 2.2.3.

A transmural metric is also necessary to compute the depth of any point within the myocardial tissue and the local thickness of the cardiac wall. The method described in [Yezzi et al., 2003] defines a smooth vector field between the boundaries (endocardium and epicardium) and solves a pair of Partial Differential Equations (PDEs) to get the shortest distance to each boundary. The thickness map is then given by the sum of these distances and normalizing one by the thickness map gives the normalized radial coordinate which is null on the endocardium and equal to one on the epicardium.

This radial coordinate is used to define smooth gradients for conduction velocity (see section 3.1.2), to create spatially varying Action Potential Duration (APD) or in the definition of the fiber directions.

2.2.2 Cardiac fibers

The spatial orientation of the muscle fibres plays a major role in the excitation and contraction of the heart [Streeter et al., 1969]. We assume that the fibre helix angle varies from $-\alpha$ to $+\alpha$ across the myocardial wall and remains constant throughout the cardiac cycle, neglecting the angle variations in any other direction.

Based on the cardiac coordinates system and the radial direction defined in the previous section, a local orthonormal basis is build on each point. The fibre directions are given by the circumferential basis vector, rotated by an angle $\alpha_f \in [-\alpha, +\alpha]$ along the radial direction (Fig. 2.7). In this framework, the angle variation is chosen to linearly increase from the endocardium ($\alpha_f = -80^\circ$) to the epicardium ($\alpha_f = 80^\circ$). Note that the septum is considered as left ventricle for the fibres generation.

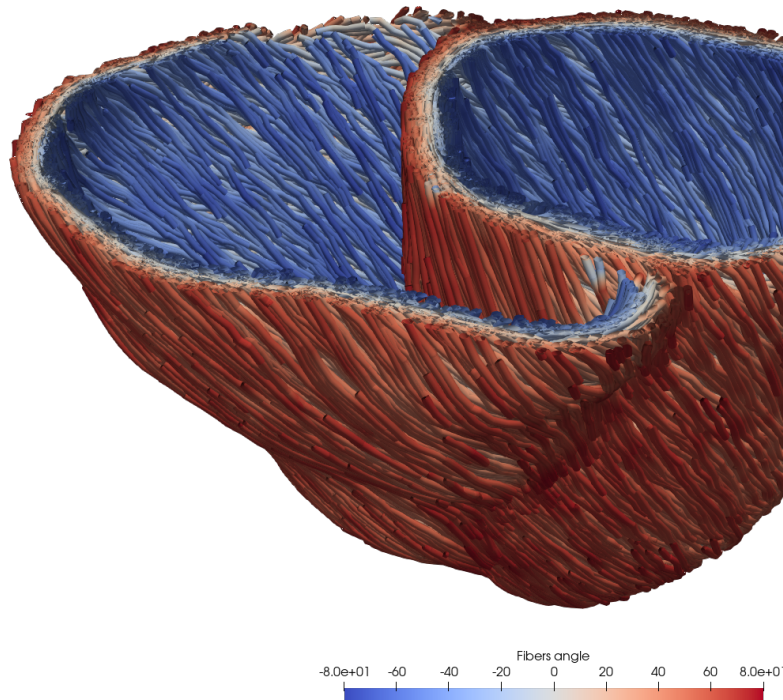


Fig. 2.7.: Short-axis clipped view of the fibers direction. The double helix is clearly visible from endocardium (blue) to epicardium (red).

2.2.3 AHA regions segmentation

The 17 American Heart Association (AHA) segments are defined as per a standardized segmentation of the left ventricle proposed in [Manuel D Cerqueira et al., 2002]. We can extend this to 29 regions (Fig. 2.6b) by including the RV to obtain the whole myocardial tissue. These segments are mostly used in the mechanical simulation. They can also give a good insight into the regional properties such as stress and strain ; thus, helping us assessing intraventricular dyssynchrony.

To build these regions for each ventricle, we let an ellipsoid fit the ventricle endocardial vertices and use the spherical coordinates to generate the regions on the ellipsoid. Finally, the segments are projected onto the tetrahedral mesh [Cedilnik, 2018]. At the base of the mesh, a stiffer and less electrically conductive region is introduced to model the valves fibrous tissue (beige region at the top of the mesh in Fig. 2.6b).

2.2.4 Purkinje network generation

The Purkinje is a fast conduction network with specialised cells, which is generated by growing it starting from the basal points on the endocardium, close to the SA node. The Purkinje generation method presented in this section is inspired from [Sahli Costabal et al., 2016]. Several tools to increase the robustness of the method, compute the distances, extract the PMJ points, or delete nodes and branches have been implemented.

Fig. 2.8 presents the growing procedure of the network. For each ventricle, the coordinates and direction of the first branch are sufficient to grow the network, see Fig. 2.9. The network increases by generations in which each branch creates two new branches, based on the initial direction and the distances from all other branches. A repulsivity coefficient controls the global distance between branches. Each branch is built with several small

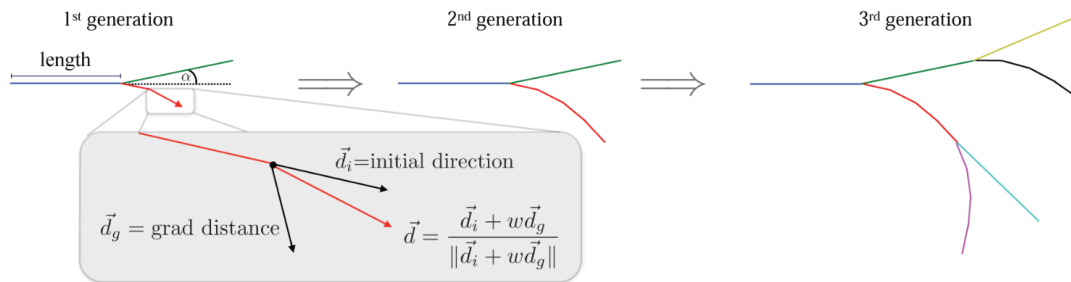


Fig. 2.8.: Growing Purkinje network. At each generation, the next branch is computed based on the current direction and the direction of all other branches with the gradient distance ; the coefficient w controls the repulsivity of the new branch. Source: [Sahli Costabal et al., 2016].

segments. Together with branch length and number of segments per branch, they control the density of the network.

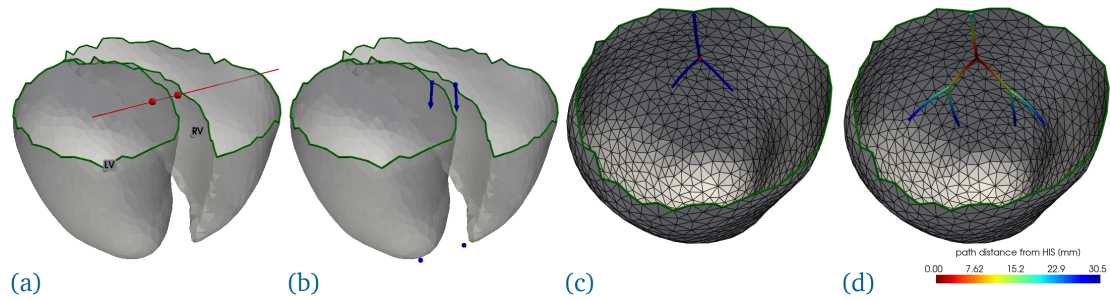


Fig. 2.9.: Procedures for the generation of the Purkinje network. (a) for each endocardial surface, in the direction of LV-RV barycenters, the intersection is performed near the base. (b) two nodes are found on the endocardium boundary edges and directions are found using the apex. (c) starting from this node, the network starts to grow. (d) the geodesic distance can be computed from any node.

In the process of creating a new branch segment, the generated node is projected on the endocardial surface, using the triangle normals. If the projection fails, the progression of the network is stopped at this point, a behavior which is not desired. Particularly with dilated geometries, the right ventricle can be quite tight near the apex and the meshes have sharp edges, leading to the projection error. To overcome this issue, the proposed method consists in using the curvature of the input endocardium to:

1. remesh the endocardial surface, discretizing the highly curved areas with very small triangles,
2. locally adapt the network segment length, proportionally to curvature.

Because the segment length is much smaller in curved areas, there is necessarily a triangle on which to project the new point. The phenomenon is visible on Fig. 2.10 where the use of small elements near the apex is beneficial for the network growth. Additionally, the endocardial surface is remeshed using a curvature-based metric in order to obtain small triangles in curved areas, which facilitates even more the projection of new points and the growth of the network.

Using curvature-based discretizations for both the triangular endocardial surface and the network's segments allows to optimize the number of nodes in the Purkinje graph, while keeping a robust growth and avoiding the projection error. The number of nodes in the graph greatly affects the computation time of the geodesic distance.

Fast computation of the geodesic distance

The geodesic distance defines a metric on the generated Purkinje network, it allows to compute the shortest path from any point on the network to the ventricle's atrioventricular node. Because the network is closed, the computation of this geodesic distance can be

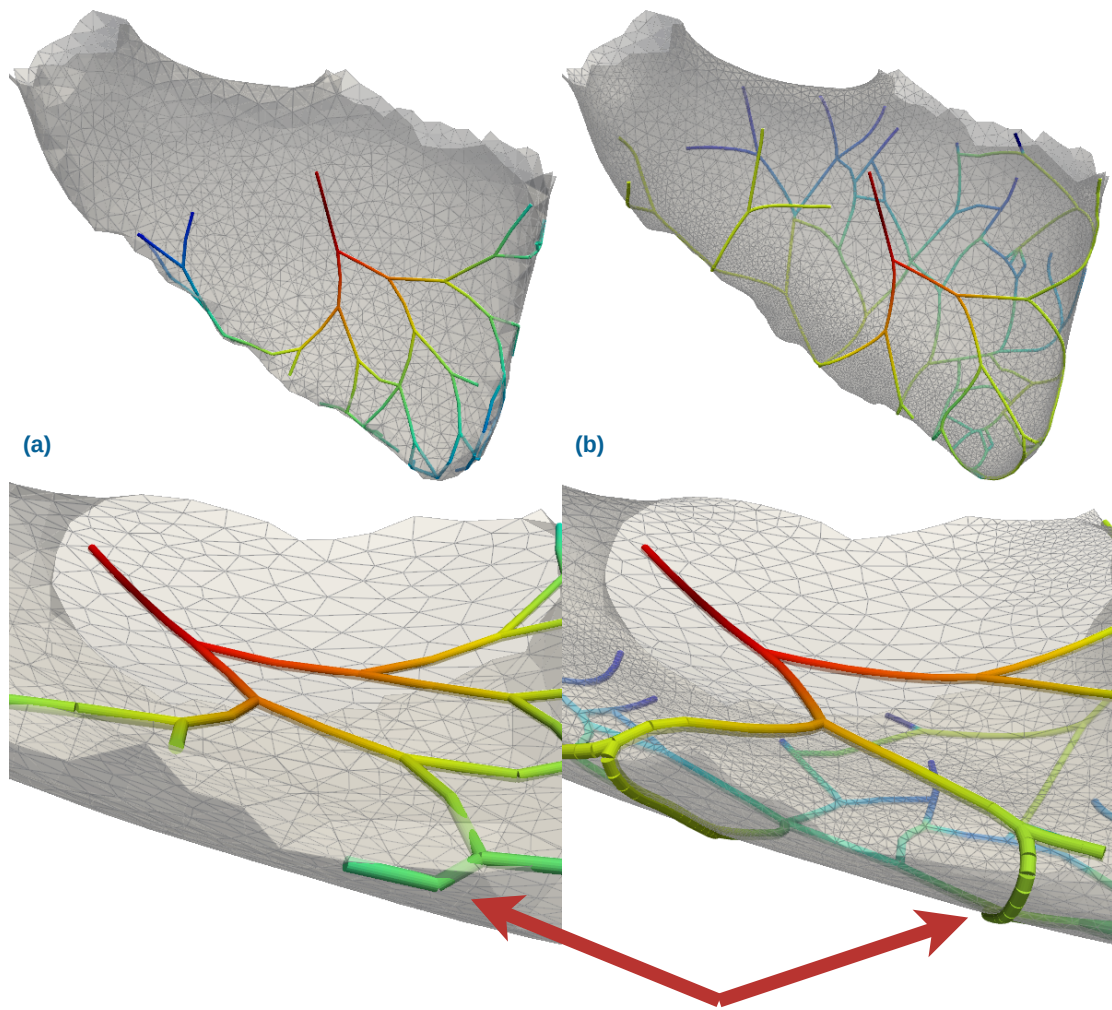


Fig. 2.10.: Right ventricle endocardium and grown Purkinje network with zoomed view on the transition septum-free wall. Comparison between the old method (a) and the curvature-based method (b). The network grows better on the RVFW when both the surface discretisation and branch length are computed from curvature.

difficult, even more so if the network connectivity is altered (e.g. defining an infarcted tissue area that may locally remove branches from the network).

An algorithm similar to the Dijkstra's algorithm [Dijkstra, 1959] is implemented in C++ and is included in the ElecModel pipeline through python bindings. The geodesic distance computation on the network is implemented in parallel and is quite fast, taking 10s for both ventricles on an Intel Core i5-4430 CPU @ 3.00GHz laptop. Without the parallelism and the C++ bindings, the pure python solution takes more than two minutes per ventricle.

In the electrophysiology model (chapter 3), this metric will be used to compute the arrival time of the electrical signal on the network's nodes. Note that the conductivity of

each point on the purkinje can be defined either locally or globally, the latter being the default implementation.

Fascicle identification for fascicular BBB simulation

To be able to simulate fascicular blocks, it is possible to identify either the anterior or posterior segments of the network. To do so, the His node is first identified (black node on Fig. 2.11), as well as the two consecutive nodes, belonging to the posterior and anterior fascicles. Then, for any point on the graph, the shortest path to either one of these nodes will give the fascicle of the current point.

Being able to monitor specific segments of the network is paramount to simulating fascicular blocks, referred as Left Anterior Fascicle Block (LAFB) and Left Posterior Fascicle Block (LPFB), in which case they can be deactivated but still functional (complete block) or removed from the graph (DCM, MI). An example of a LPFB is presented Fig. 3.17.

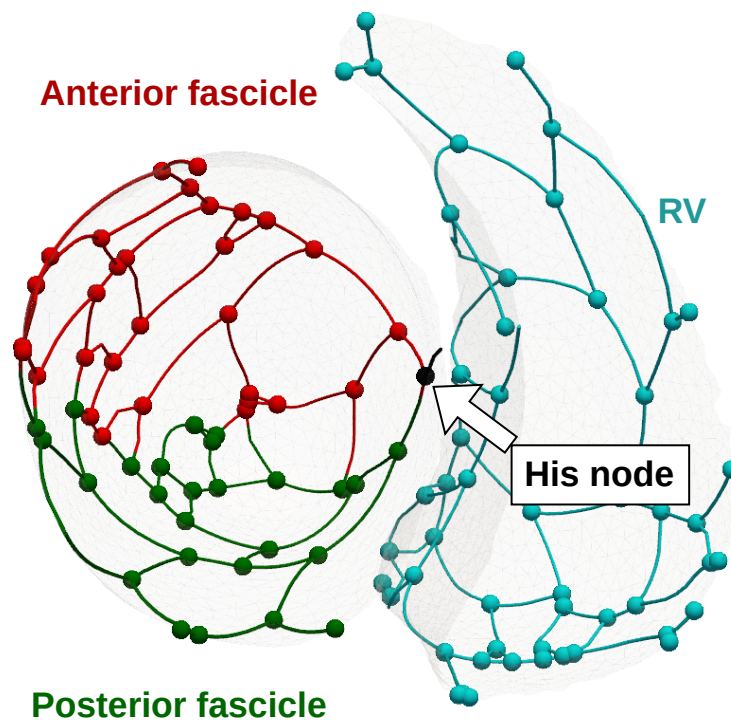


Fig. 2.11.: PMJ nodes and network labels. The black node represents the His node, the cyan is the RV Purkinje network. In the LV, the anterior fascicle is shown in red and posterior in green.

2.2.5 Conclusion

The anatomical model presented in this chapter is able to generate realistic geometries among the selected cardiomyopathies. The deformation model relies on a few number of parameters that have a meaningful significance and five modes of deformation, allowing for a fine-tuning of the geometry. Then, all the geometric quantities are computed, including the cardiac coordinates, the ventricles' volume and wall thickness. The deformed mesh is remeshed using a heterogeneous metric to optimize the size and number of elements depending on the wall thickness. This reduction in the number of elements allows to reduce the time required for the resolution of the FEM dynamical system, presented in chapter 4. The cardiac coordinates are also used for the generation of the double-helical arrangement of the myocardial fibers, and the segmentation of the AHA regions.

This model also accounts for the fast-running Purkinje fibers, being able to robustly grow a Purkinje network on a given endocardial surface, compute the geodesic distance between two nodes, remove the PMJ nodes affected by an infarct and eventually locally deactivate the network. Note that the fast-running Purkinje fibers only account for the extramural conduction system. The intramural Purkinje fibers are also included in the cardiac model and will be presented in section 3.1.2.

Additionally to the geometry and the generated cardiac structures, the torso of the patient has also been included in this framework. It allows for precise localization of the ECG leads, but also the orientation of the heart within the body. Elongated and thin torsos are associated with more vertically oriented hearts, while the apex is higher and the heart more horizontal in shorter people.

The anatomical data is generated in less than a minute (without the deformation model), a description of the resources used for its computation is presented Fig. 3.21. If a transformation of the template mesh is required, the deformation model takes less than thirty seconds.

Globally, the anatomical model sets up the computational domain and spatial parameters for the electrophysiological simulation.

Electrophysiology model

3.1	Propagation of the electrical depolarization wave	35
3.1.1	A conduction model for the heart tissue	35
3.1.2	Conduction velocity	37
3.2	Fast model for 12-lead ECG generation	38
3.2.1	The heart as bioelectric source	38
3.2.2	Modelling the action potential	39
3.3	Signal processing on the ECG	40
3.3.1	ECG signal processing pipeline	40
3.3.2	QRS axis determination	43
3.4	Calibration of the electrophysiological model	44
3.4.1	Healthy and dilated geometries	44
3.4.2	Sensitivity analysis on the electrical parameters	46
3.5	Pathological simulations	52
3.5.1	Simulating bundle branch blocs	52
3.5.2	Simulating fascicular blocks	53
3.5.3	Simulating ischemia	53
3.5.4	Discussion	53
3.6	Pacing simulation	54
3.6.1	Cardiac stimulation and defibrillation	54
3.6.2	Implementation of cardiac stimulation	55
3.6.3	Simulating CRT	58
3.7	Conclusion	59

This chapter is partly based on the following paper:

Personal-by-design: a 3D Electromechanical Model of the Heart Tailored for Personalisation. *Gaëtan Desrues, Delphine Feuerstein, Thierry Legay, Serge Cazeau, Maxime Sermesant.* FIMH 2021 - 11th International Conference on Functional Imaging and Modeling of the Heart, Jun 2021, Stanford, CA, United States.

This chapter introduces one contribution, concerning the implementation of the stimulation method and the coupling between the free-running Purkinje network and the myocardial tissue. Indeed, because the specialised His-Purkinje network is

more conductive than cardiac tissue and blood, the electrical signal can travel at high speed to distal regions of the heart and initiate depolarization points (myocardium to Purkinje activation) that would have been depolarized later with pure cell to cell conduction. It is also possible that some myocardial cells activate the Purkinje network, allowing for fast propagation of the electrical signal and earlier activation of distal tissue (Purkinje to myocardium activation). In both cases, special care must be paid to the activation map so that all depolarization follow the correct order ; this is done by iteratively recomputing the activation map.

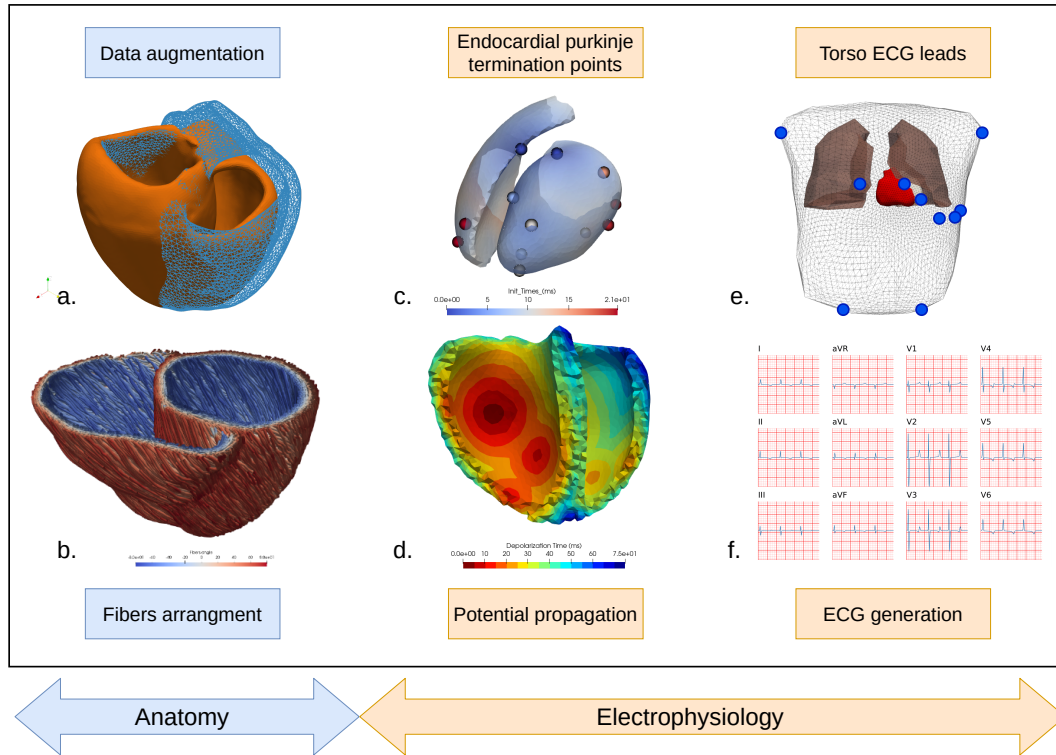


Fig. 3.1.: Pipeline for patient-specific electrophysiology simulation. a. Initial and modified geometries. b. Fibre directions. c. Activation points and activation times on the endocardial surfaces. d. Activation map. e. Leads location on a virtual torso. f. 12-lead ECG. This pipeline generates all the data required to run the mechanical simulation.

The electrophysiology plays an important role in the cardiac function as it triggers the biomechanical contraction of the cardiac tissue. In physiological conditions, the electrical pathway is well known as described in 1.1.1. Harmonized propagation of the depolarization wave ensures that all cardiac segments contract altogether to produce the maximum stroke volume with minimum energy consumption. However, various conditions can affect this usually optimised machinery and force the heart to adapt. This part will focus on a few electrophysiological causes of dyssynchrony, such as complete or partial BBB or local ischemia.

This chapter introduces a fast propagation model for the depolarization wave, including some complex structures of the heart such as the His-Purkinje network. Then, a simple ECG generation method is proposed and allows one to compute the twelve-lead electrocardiogram within seconds, based on the electromagnetic activity of the heart. This measure of the cardiac activity is primordial in this thesis work as it constitutes a reliable connection between the model's behavior and the real-world clinical data and expertise. Finally, the implementation of the pacing protocol is detailed and the results on calibrated cases are discussed.

3.1 Propagation of the electrical depolarization wave

At each cardiac cycle, the mechanical contraction of the heart is driven by the electrical activation. The electrical signal emerging from the atrio-ventricular node is conducted along the bundle of His and the Purkinje network to the endocardium (Fig. 3.1c). The numerous termination points of the Purkinje fibers on the endocardium are reduced to a dozen of points (Fig. 3.1d) and selected to match a real endocardial map (Fig. 3.2). To account for the fast potential propagation due to the Purkinje fibers, a thin endocardial layer is assigned a higher isotropic conductivity.

Since the present biventricular geometry does not have atria, the propagation of the electrical signal from the sino-atrial to the auriculo-ventricular node is not simulated. However, atria are included in the biomechanical model, see for example 4.2.7. This chapter only focuses on the electrophysiological ventricular activity, originating from auriculo-ventricular node. Thus, no P wave is present on the ECG.

3.1.1 A conduction model for the heart tissue

As described in section 1.1.1, the depolarization of cardiac cells consists in a change of the transmembrane potential by exchange of ions inside and outside the cell. Mathematical models describing this complex biochemical activity do exist [Tusscher et al., 2004; Kosta et al., 2021] and include several ions concentrations at the cellular scale, as well as their flux through specific ion channels across in the membrane. This type of electrophysiological model is known to accurately describe the cardiac cell behavior but is computationally demanding. Another type of bidomain electrophysiological model are the phenomenological ones, that try to reproduce the shape of the action potential using a non-linear system of ODEs [Mitchell, 2003; Aliev et al., 1996]. With fewer parameters, they are much faster than biophysical ionic models, but they still allow to simulate the variations of the transmembrane potential and the propagation of the depolarization wave. However, eikonal models are much faster and only describe the activation front of the electrical signal with isochronous surfaces. They have been used

in cardiac simulations in the past [Talbot et al., 2013; Wallman et al., 2012; Sermesant et al., 2007].

In the present work, the potential propagation is computed using a fast marching method [Mirebeau et al., 2019] and solving the anisotropic eikonal equation for each mesh vertex:

$$\sigma \sqrt{\nabla T^T D \nabla T} = 1 \quad (3.1)$$

where σ is the local conduction velocity, D the anisotropy tensor and T the arrival time of the depolarization wave.

After a short period of time (duration of the QRS), all the myocardial cells are activated and contract until the repolarization wave arrives. The action potential duration (APD) is linearly interpolated from the endocardium to the epicardium (shorter on the epicardium), using a wall depth map.

Our eikonal model has been compared with an endocardial map acquired with catheter mapping, see Fig. 3.2. After manual selection of the onsets points on the endocardial surface, the results show a good correspondence between the depolarized areas in the real and simulated cases. The activation map indicates the Electrical Arrival Time (EAT) on any point of the mesh. If not mentioned otherwise, $t = 0$ corresponds to the first node being depolarized on the mesh, and is referred as the His node, as seen in Fig. 2.11.

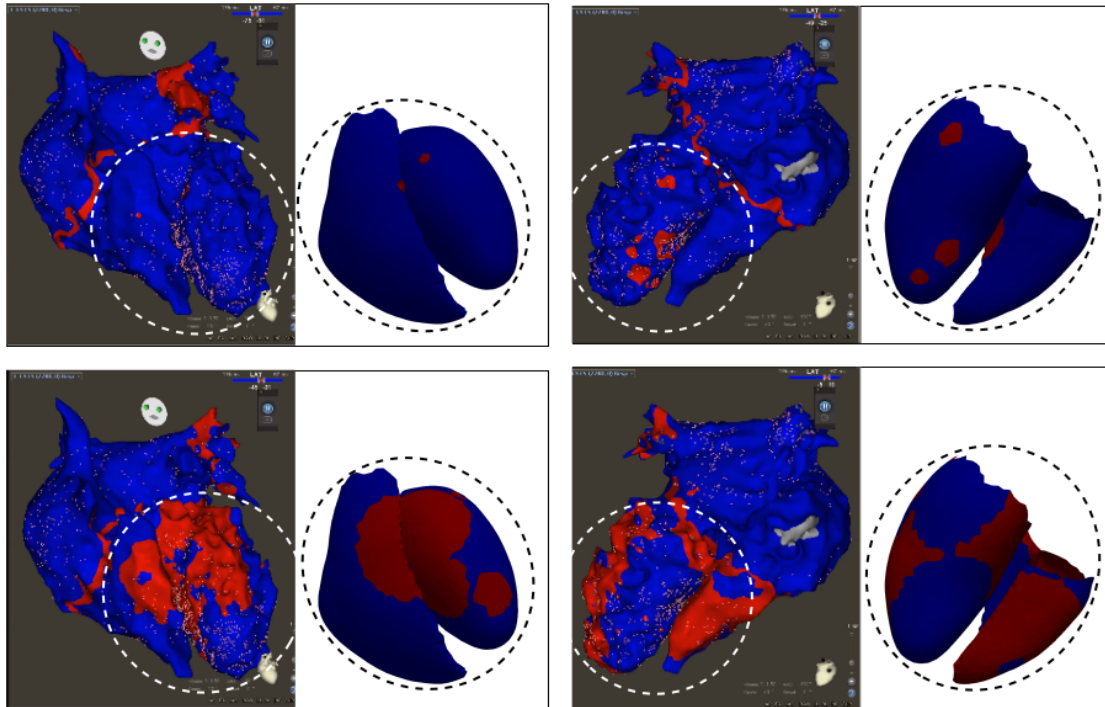


Fig. 3.2.: Real endocardial activation map (courtesy of Dr.Mouhoub) and their computed homologous, at different points in time. The computed map (white background) shows both ventricles endocardium (no atria) and the fast isotropic propagation wave.

This experiment showed that the location and activation timing of these onset points is quite significant in the electrical pathway, and that all onsets are relevant when matching the real-world data. These observations have led to the development of the His-Purkinje network, for physiological arrangement and timing of the onset activation points. Moreover, note that the endocardial propagation is chosen to be isotropic (D is set to identity), this will be discussed in the next section.

Beside the anisotropy tensor D , that is based on local fibers arrangement, the local conduction velocity σ must be defined on the computational domain and has a primary role in the eikonal propagation wave.

3.1.2 Conduction velocity

Conduction velocity is known to be deeply heterogeneous in the heart, even within the myocardial tissue. The combined presence of highly conductive purkinje fibers in the cellular matrix, fibrotic tissue, or even ischemic regions that do not, or poorly transmit signal, makes the modelling of local conductivities rather complex.

Determination of the local map of electrical conductivities has been studied in recent years, involving the acquisition of invasive data, such as the activation map [Pheiffer et al., 2017; Chinchapatnam et al., 2008], or with non-invasive data, such as the Body Surface Potential Mapping (BSPM) [Giffard-Roisin et al., 2017] or the ECG [Zettinig et al., 2014].

The approach used in this thesis relies on the ability to explain each parameter, while keeping a total number of significant parameters low. To this end, the conduction velocity is set to a uniform value in the whole myocardium, typically the measured conductivity in the cardiac tissue, see table 3.1. Then, based on the observations made in [Martinez et al., 2018] that account for the presence of subendocardial activation, a different conduction velocity value is assigned to a thin region (1-4mm) on the endocardium. Because of the high density of this subendocardial Purkinje network and its independence to cardiomyocytes preferential propagation direction, the endocardial region is isotropic see Fig. 3.3, with a greater velocity as compared to pure myocardium. Finally, this procedure is applied to either one of both ventricles, leading to six parameters defining the local velocity of the propagation wave, on the whole biventricular computational domain.

3.2 Fast model for 12-lead ECG generation

The electrocardiogram (ECG) is a non-invasive measure of the heart's activity and a routine practice in clinics. Being able to monitor the electrophysiological simulated activity on the torso is primordial.

3.2.1 The heart as bioelectric source

The ECG records the bioelectric activity of the cardiac cells by measuring the electrical potential at the 6 precordial leads placed on the patient's torso and 3 (or 4) limb leads

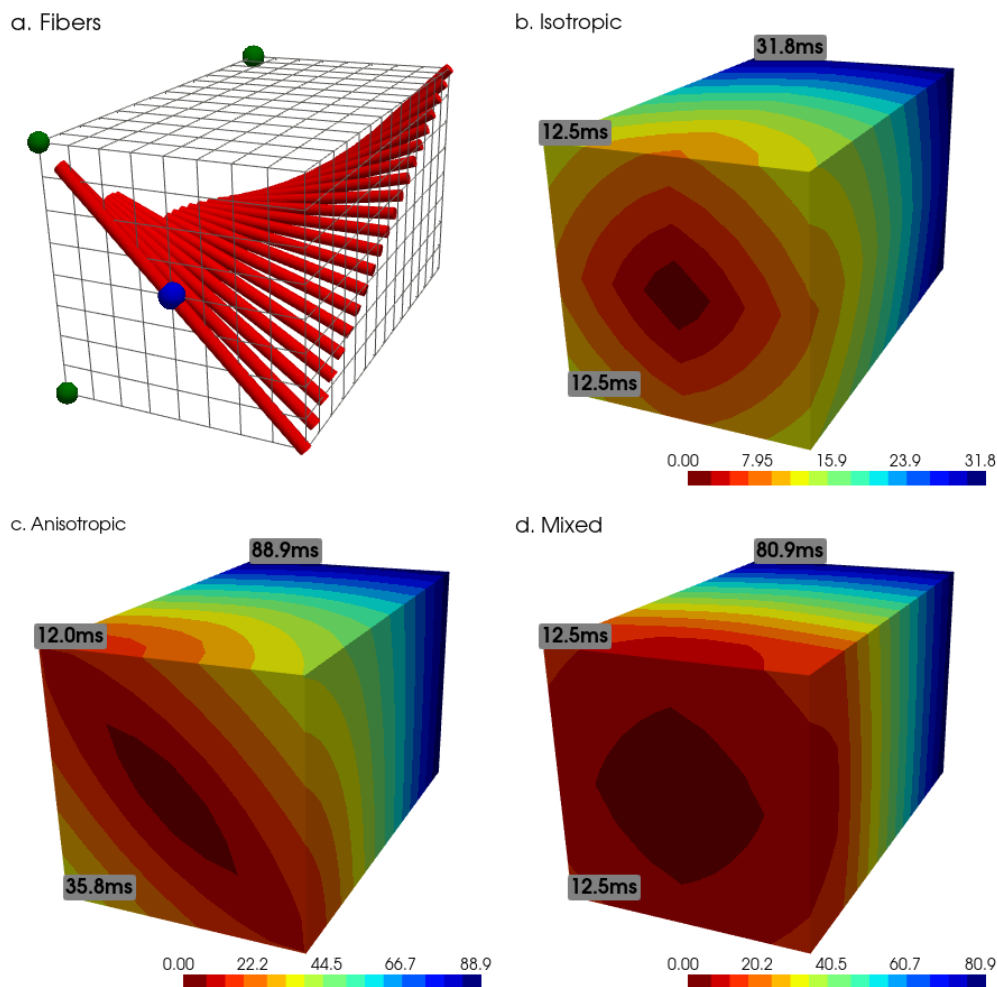


Fig. 3.3.: Examples of activation maps for different scenarios on a $8 \times 8 \times 15$ mm myocardial cross-section with endocardial pacing. Endocardium is in the front while the epicardium is in the back. a. Fibers arrangement linearly varying from -45° on endocardium to 45° on epicardium, and the stimulation point (blue). Reference points (green) are used to compare the arrival time of the depolarization wave in ms. b. Isotropic propagation. c. Anisotropic propagation with anisotropy ratio of 0.3. d. Isotropic endocardial propagation (3mm) and anisotropy in the remaining myocardium. The color bar indicates the EAT, in ms.

	Myocardium	Endocardium	His	Purkinje
[Malmivuo et al., 1995]	0.3-0.8	-	1.0-1.5	3.0-3.5
[Sermesant et al., 2012]	0.5	4-5	-	-
[Tusscher et al., 2008]	0.7	-	-	3.0
[Barber et al., 2021]	-	-	-	1.7-2.2

Tab. 3.1.: Conduction velocities (along fibers for the myocardium) found in the literature for healthy human hearts [m/s].

(Fig. 3.1e). In order to simulate this electrical activity, we consider each voxel of the image as a dipole of current density $\mathbf{j}_{\text{eq}} = -\sigma \nabla v$ where ∇v is the spacial gradient of the potential v [Cedilnik et al., 2019]. By using the chain rule, we obtain:

$$\mathbf{j}_{\text{eq}} = -\sigma \frac{\partial v}{\partial T} \nabla T \quad (3.2)$$

where σ is the local conductivity, ∇T the gradient of the activation map and $\frac{\partial v}{\partial T}$ is given by solving the Mitchell-Schaeffer model [Mitchell, 2003] using a forward Euler scheme. We suppose here that the body is a homogeneous material with constant conductivity σ_T . The electrical potential at a distance r from the source is developed in [Malmivuo et al., 1995] and is given by:

$$\Phi(r) = \frac{1}{4\pi\sigma_T} \int_V \mathbf{j}_{\text{eq}} \cdot \nabla \left(\frac{1}{r} \right) dV \quad (3.3)$$

We finally derive the potential contribution of each voxel with the Einthoven triangle to obtain the augmented leads and plot the electrocardiogram Fig. 3.1f.

3.2.2 Modelling the action potential

Since the Eikonal model only yields the arrival time of the depolarization wave, it is not possible to compute the gradient of the action potential, required to express the current density \mathbf{j}_{eq} . To compute this gradient, we used a forward Euler scheme to solve the monodomain version of the Mitchell-Schaeffer cardiomyocyte action potential model [Mitchell, 2003], as in [Talbot et al., 2013].

The Mitchell-Schaeffer model defines two variables, the transmembrane potential v and h , a secondary variable controlling the repolarization phase. Note that the coefficient τ_{close} mainly affect the APD90 duration, or 90% of the action potential duration. This

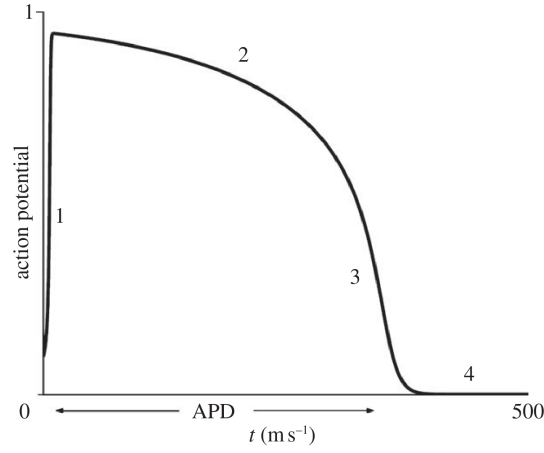


Fig. 3.4.: Normalised transmembrane potential as described in [Mitchell, 2003]. 1: depolarization, 2: plateau phase, 3: repolarization, 4: rest potential.

parameter is also important for the mechanical simulation since it controls the contraction duration of the cardiac cells, and thus influence the duration of the ejection phase.

$$\begin{cases} \partial_t v = \text{div}(D \nabla v) + \frac{zv^2(1-v)}{\tau_{in}} - \frac{v}{\tau_{out}} + J_{stim} \\ \partial_t h = \begin{cases} \frac{1-h}{\tau_{open}} & \text{if } v < v_{gate} \\ \frac{-h}{\tau_{close}} & \text{if } v > v_{gate} \end{cases} \end{cases} \quad (3.4)$$

3.3 Signal processing on the ECG

Since the ECG constitutes the main interface between the patient's cardiac activity, the practitioner and the cardiac model, a special attention is given to its automated analysis. This section introduces the ECG features that will be used for the remaining of this thesis, such as the five waves of the QRS complex and the QRS axis.

Note that since we are primarily focused on the propagation of the depolarizing wave, only the QRS complex will be extracted and studied. Atria depolarization (P) wave and ventricular repolarization (T) wave are not considered in the present manuscript, although the model is able to produce T waves.

3.3.1 ECG signal processing pipeline

ECG filtering and sampling

Although the typical ECG generated by the model may be quite smooth, real-world ECGs are often noisy and may be altered by the following: movement of the patient (either

breathing or muscles artifacts), electrical interference from surrounding equipment, or signal corruption by any processing such as analog to digital conversion. Simple linear filtering is used here, applying both low and high bandpass filters to remove undesired frequencies in the frequencies' spectrum, see Fig. 3.5. Typical values found in the literature for cutoff frequencies are 0.05-40Hz [Clifford et al., 2006; Karraz et al., 2006] so that information is preserved at 0.3Hz, the accepted low frequency limit of the informative signal range [Berson et al., 1966]. In 1990 the American Heart Association (AHA) established a standard 0.05 to 150 Hz bandwidth for the routine recording of 12-lead ECG and authors have been using values ranging from 40 to 150Hz for the high pass. However, as demonstrated in [Ricciardi et al., 2016] and observed in our analysis, 40Hz high pass filtering does not affect ECG clinical interpretation and allows better quality of tracings.

After filtering, signals are resampled from 400Hz to 1000Hz using linear interpolation. Note that the ECGs generated by the model are already sampled at 1000Hz.

Finding the cardiac cycle in an ECG recording

Detecting the cardiac cycle is perhaps the most common practice in ECG analysis and is usually done by identification of the R wave of the QRS complex [Nacif et al., 2011]. Simple peak-detection algorithms can roughly identify the QRS complex and extract one cardiac cycle that contains it.

Deriving the QRS complex

Once the cardiac cycle has been extracted from the signal, a series of signal processing operations are performed to segment the QRS complex. The depolarization of the ventricles is the principle electrical activity observed on the ECG recording and is characterized in particular by a high voltage on the Q and R waves. Taking the absolute value of gradient thus magnifies these variations, see Fig. 3.5. Finally, we use a moving window as in [Augustyniak, 2010; Jokic et al., 1970] to extract the relevant parts of the signal by averaging the gradient. Best results were found using a window length of 100ms. This method yields the beginning and final time stamps of the QRS, as shown Fig. 3.5 and Fig. 3.6a.

Consensus for the 12-lead ECG

The QRS complex is extracted from all twelve derivations and aggregated to give a final segmentation for the whole ECG. Having a consensus between the twelve leads increases the robustness of the segmentation, in particular for isoelectric or noisy derivations.

Let v_s and v_l be the 12-length vectors of timestamps for QRS start and length respectively. The consensus is given by the q^{th} quantile of each vector, $q = 0.1$ for v_s and $q = 0.9$ for v_l .

Working with the quantiles instead of the values ensures that segmentation artefacts are not included in the final decision. Finally, this method yields the starting time and duration of the QRS complex, for the twelve derivations of the ECG.

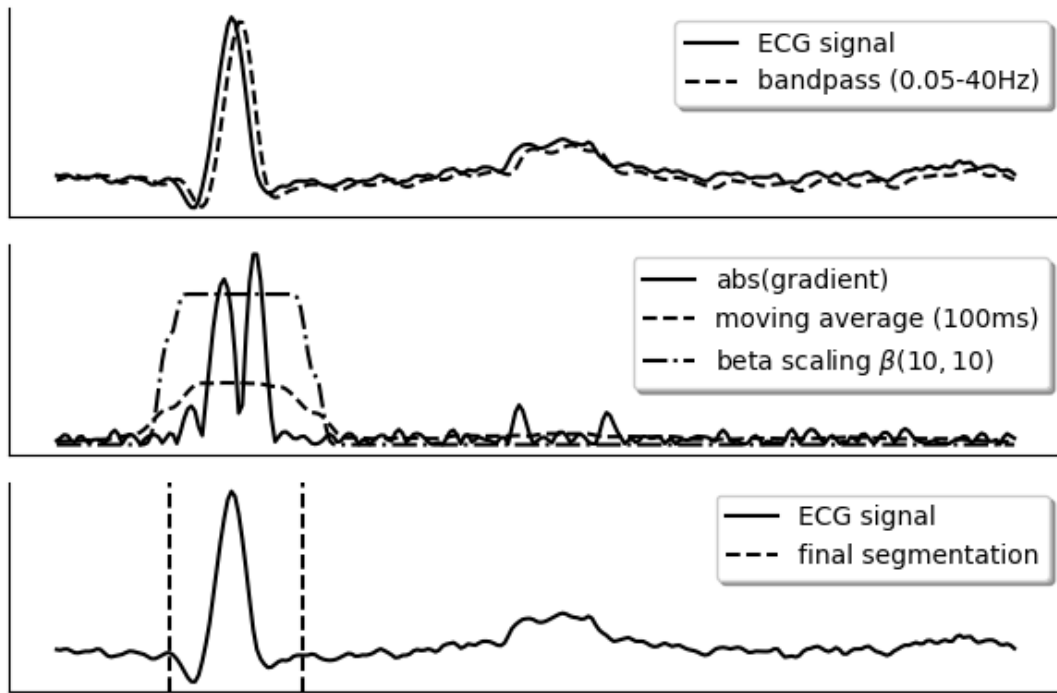
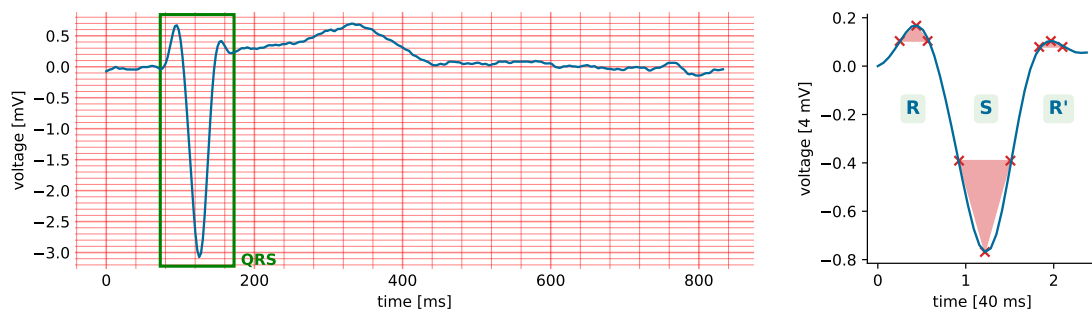


Fig. 3.5.: ECG signal processing and QRS detection. The signal is first filtered to remove any artifacts, then a moving window of 100ms is applied and extracts the range of values where the signal varies the most, giving the QRS complex. A consensus is then made on the twelve derivations.

Extraction and identification of the QRS complex

At this step of the pipeline, the QRS complex is identified and segmented on a signal sampled at 1000Hz. It gives the voltages measured on the torso during the ventricular depolarization, lasting between 70 and 90ms for healthy patients and up to 200ms for desynchronized patients. Again using a peak detection algorithm constrained on width



(a) Segmentation of the QRS complex in a one beat signal

(b) QRS waves identification

Fig. 3.6.: Signal processing on the ECG.

and prominence, all the waves are localized on the signal. They are successively labelled as Q, R, S, R', and S' waves, depending on their sign and order. All remaining waves are ignored. Moreover, it is possible that one or more waves are not present in the signal, especially for healthy patients, as seen in Fig. 3.6b.

At this step, the ECG processing pipeline has extracted at most 60 labelled waves with their time location, amplitude and prominence, as well as the QRS duration. The next section will detail the determination of the QRS axis, another meaningful feature that can be extracted out of an ECG.

3.3.2 QRS axis determination

The QRS axis represents the mean current flow during ventricular depolarization, projected on the frontal plane, see Fig. 1.6. The normal axis points mostly downward and to the left because the more muscular left ventricle generates a stronger depolarizing current that overwhelms that generated by the less bulky right. Right and Left Axis Deviation (RAD and LAD respectively) may indicate an underlying pathology such as hypertrophied or infarcted tissue, or a conduction disorder affecting one side of the heart, for example a bundle branch block.

Physiologically, a positive deflection on an ECG derivation means that the electrical forces are moving towards the lead, while negative deflection indicates the current is moving away. Minimal deflections will be formed when the electrical forces are moving perpendicular to the lead. These observations allow clinicians to quickly compute the QRS axis from an ECG.

Classical axis determination method

This is the preferred method used by clinicians as it gives a good approximation of the QRS with a glance at the ECG. The most isoelectric derivation is chosen among the limb leads, it corresponds to the perpendicular direction of the mean current flow. This isoelectric direction may be located in between two leads if no derivation is found isoelectric, see Fig. 1.6. Then, the perpendicular lead gives the mean direction of QRS depolarization. The sign of the deflection on the corresponding ECG derivation finally gives the QRS vector, that can be reported on the hexaxial reference system to find the QRS axis.

From the standard derivations

The previous method, while quite adapted for the human eye and the experienced clinician, is not appropriate for computers. This method is not robust to ECG artifacts such as misplacement of the leads, and extrapolation whenever an isoelectric derivation

is not found can be difficult to implement. The protocol to numerically compute the QRS axis is based on reporting the voltage from two standard derivations on the hexaxial system presented in Fig. 1.6, either leads I and aVF or I and III. Although the perfect QRS axis determination method is still lacking [Gao et al., 2020], they have been extensively discussed [Martinez-Diaz et al., 2008; Mitra et al., 2007] and tend to favour leads I and aVF. Also, because a computer can measure the areas of ECG waves, whereas interpreters necessarily use their amplitudes, the computer is always more accurate [Spodick et al., 2008].

From the activation map

Whenever the activation map is available, it is the best method to approximate the QRS axis since it has a direct meaning related to the electrical activation pathway. To this end, the mean gradient of the arrival times is projected onto the frontal plane and yields the exact QRS axis.

Discussion

Although the QRS axis is an important feature of the ECG and clinically meaningful, its precise value is not required for the classification of normal or deviated axis. All methods yield similar results (see Fig. 3.11).

3.4 Calibration of the electrophysiological model

Calibration is an important step in the development of a mathematical model, it ensures that the output quantities are those expected by the user. Calibration consists in finding a set of parameter values such that the model predictions are similar to the observed data. It also gives the interval of parameter values in which the model's output is valid and meaningful. This section describes the different strategies that are adopted to this end.

Previous work used the Unscented Transform algorithm as an automatic calibration method [Marchesseau et al., 2012], but it still requires a lot of simulations and results are not granted. Instead, the calibration is here performed manually with a clinical validation and allows for finer tuning of the parameters.

3.4.1 Healthy and dilated geometries

This section presents the sinus rhythm simulation results of the electrophysiological model, for the two geometries displayed in Fig. 3.7.

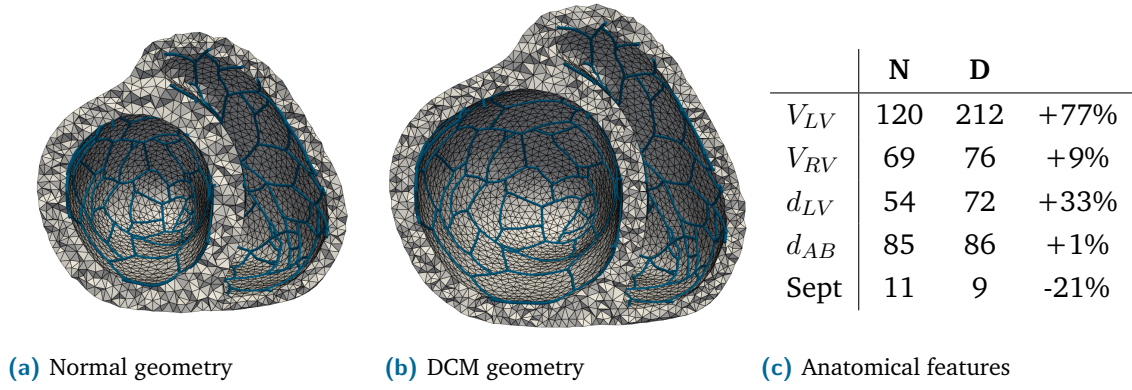


Fig. 3.7.: Baseline anatomical geometries. V : ventricular volume [mL], d_{LV} : diameter [mm], d_{AB} : apico-basal distance [mm], Sept: septal thickness [mm]. N: normal geometry, D: DCM. The last column of the table indicates the evolution of the features as compared to the normal geometry.

Healthy

The geometry in Fig. 3.7a constitutes the healthy baseline result of the anatomical model, featuring a 120mL LV volume and septal thickness of 11mm. The Purkinje network has also been generated on the endocardial surfaces of this geometry.

Fig. 3.8 presents the activation map and the corresponding 12-lead ECG, focused on the QRS complex tracings. The computed QRS duration is 77ms while the axis is 7° , thus classified as normal axis and duration. Several features of a healthy heart are also visible on the ECG, such as the negative to positive transition of the signal in the precordial leads, with the transitional zone in lead V3. A large positive deflection -R wave- is present in leads I, II, V4-V6 as well as a large S wave in leads aVR, V1 and V2. This experiment shows that the model is able to simulate a healthy depolarization, as seen on the ECG. It is also compatible with the ventricular activation described in [Durrer et al., 1970].

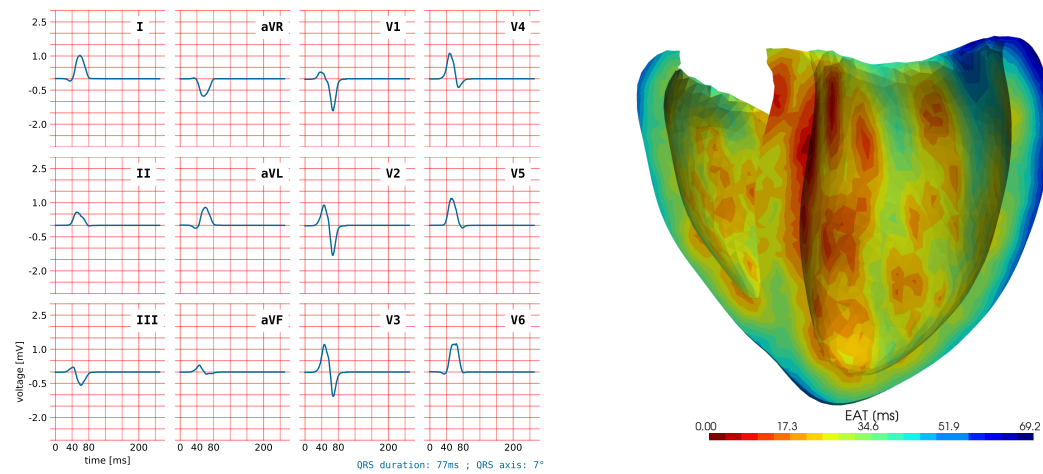


Fig. 3.8.: Electrophysiological simulation of the healthy heart, showing the QRS tracings (left) and the activation map (right). QRSd=77ms, QRSa= 7° , max (EAT)=69.2ms.

Dilated cardiomyopathy

Applying the deformation model presented in section 2.1.2 to the healthy geometry leads to the dilated geometry in Fig. 3.7b, featuring a 212mL LV volume and thinned LV wall. The Purkinje network has been projected using barycentric coordinates from the normal geometry to the dilated one so that simulation contexts are as close as possible. Moreover, since dilatation is often associated with an increase in fibrotic tissue in global reduction of the conductive property of the myocardial tissue, all conductivities are reduced by 25%.

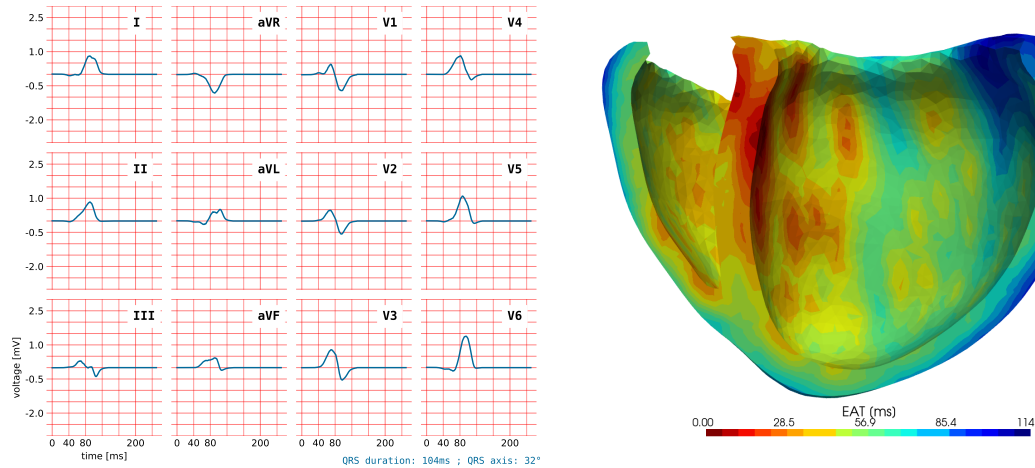


Fig. 3.9.: Electrophysiological simulation of a DCM with spontaneous activation. Note that the dilatation of the heart is a sign of an underlying pathology, which is not included in this simulation. QRSd=104ms, QRSa=32°, max (EAT)=114ms.

Fig. 3.9 shows the resulting ECG and activation map on the dilated geometry. The 124ms QRS is wider but the axis remains normal (30°). Note that this experiment only shows the impact of the dilatation on the depolarization but does not represent real-world cases since dilatation is always resulting from an underlying pathology such as conduction disorders, e.g. BBB. Nonetheless, it shows that the model is able to simulate a sinus rhythm propagation on a dilated geometry and that decreasing conductivities is necessary to obtain QRS durations that are close to the ones observed in diseased hearts.

3.4.2 Sensitivity analysis on the electrical parameters

The sensitivity analysis represents the behavior of the model relative to each parameter. First, a scalar interval is assigned to each of the n parameters, centered on the baseline value calibrated in the previous section. Then, m values are uniformly sampled on the interval, thus giving $n \times m$ sets of parameters, and $n \times m$ simulations to run in parallel. For each simulation, $n - 1$ parameters are fixed to their baseline value and one parameter is sampled within a defined interval.

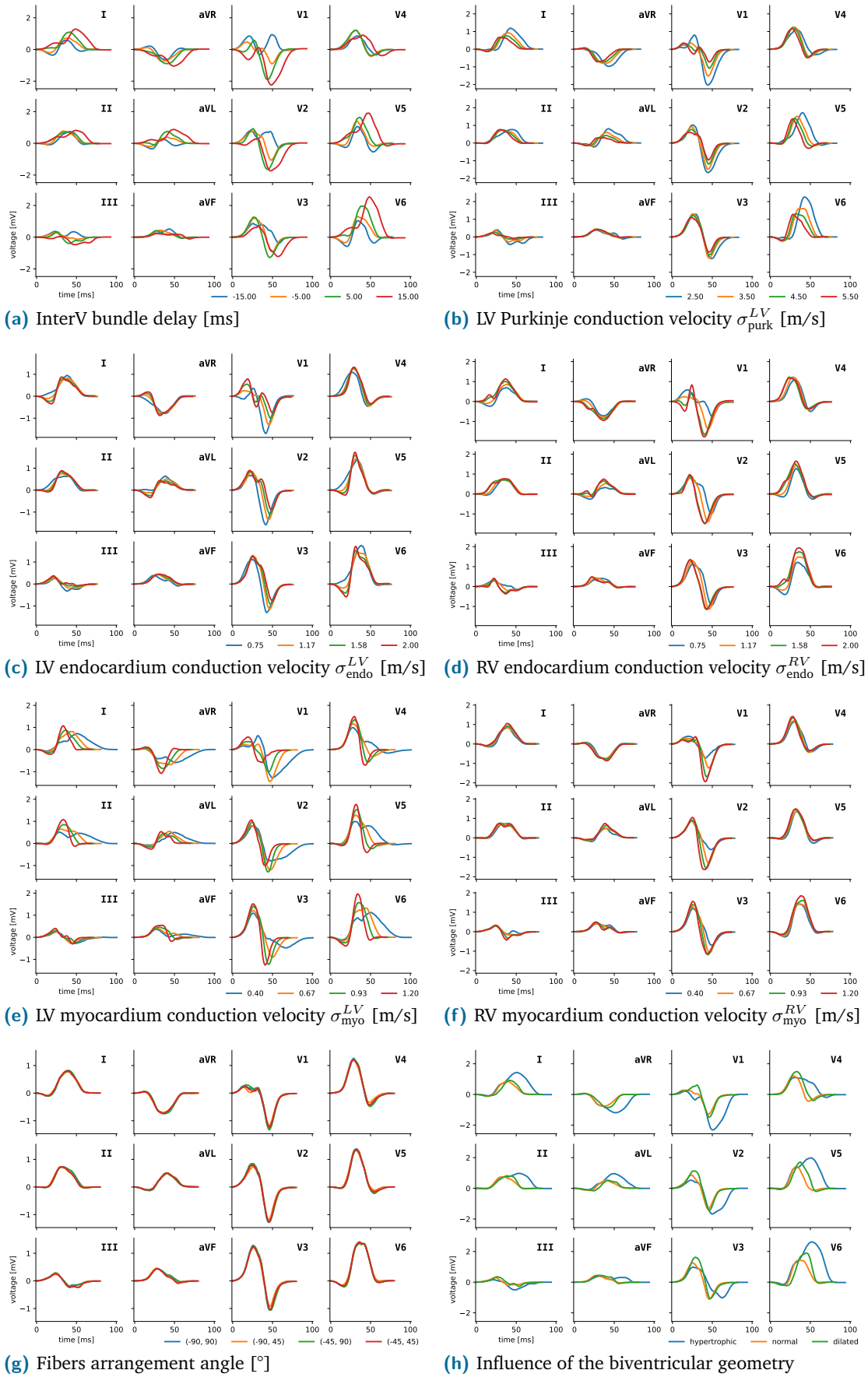


Fig. 3.10.: Results of the sensitivity analysis showing the impact of each parameter of the electrophysiological model on the 12-lead ECG.

Influence on the 12-lead ECG

The results of this experiment are presented in Fig. 3.10. All simulations are run on the healthy geometry (Fig. 3.7a) except mentioned otherwise. As a general remark, we can notice that all selected parameters are relevant given the variations on the ECG that can be observed when they are modified, except for the fibers angles, which does not seem to affect the way the depolarization wave propagates. In fact, it can be seen on Fig. 3.3 that the transmural propagation induces homogeneous activation times on the epicardium, be the propagation isotropic or purely anisotropic. Furthermore, the isotropic metric set on the endocardium helps in propagating the electrical signal all over the ventricle, thus reducing the effect of a preferred direction that slows down the signal in some areas.

On the contrary, the interventricular bundle delay has a great influence on the shape of the QRS waves. Because it modifies the direction of the early septal propagation, its influence is quite visible on the first wave in leads V1 and V2. When negative, the first onset point is located on the LV and propagates mainly towards the RV, thus giving a positive deflection on V1. Inversely, a positive interventricular bundle delay will yield a negative deflection (Q wave) on V1, the depolarization wave propagating from the RV to the LV, through the septum.

Regarding the LV Purkinje network conduction velocity, Fig. 3.10b, the shape of the QRS is not altered but this parameter rather influences the duration of the ventricular activation. Indeed, a slower conduction velocity leads to a late activation of the LV lateral wall, which can be seen on leads I, aVL, V5 and V6, extending the QRS by thirty milliseconds. The same observation can be made for the RV Purkinje conduction velocity (not plotted) with less influence, given the smaller mass of the RV as compared to the LV.

As for the interventricular bundle delay, the endocardial conduction speed impacts mostly the beginning of the QRS and the depolarization through the septum (figures 3.10c and 3.10d). Even for the slowest conduction velocity, the electrical signal is transmitted mainly with the Purkinje network to the distal segments of the heart, allowing to have an almost constant QRS duration.

The myocardial conduction speed, however, greatly burdens the duration of the QRS complex, mostly for the LV, as it is seen in the latest parts of the QRS signal in Fig. 3.10e. The RV, much thinner, benefits from the endocardial layer of rather fast conductive tissue to balance the lower myocardial conduction rate, see Fig. 3.10f.

Finally, the influence of the anatomical geometry is presented in Fig. 3.10h. As for Fig. 3.10e with a reduced conduction speed, the LV hypertrophic geometry causes a delay in the LVFW activation, visible in all derivations with a large, lasting wave. For the dilated

geometry, as opposed to Fig. 3.9, baseline conductivities have not been altered, leading to only small differences as compared to the normal geometry. Only a small LV delay can be observed.

Influence on the computed ECG features

Fig. 3.11 shows the results of the sensitivity analysis on the QRS duration and axis. As mentioned previously, endocardial conduction velocity does not affect the QRS duration, as opposed to the myocardial LV one. This prolonged QRS duration can also be observed when the LV is depolarized long after the RV due to a significant interventricular bundle delay.

Regarding the QRS axis, it can be noticed that it increases (towards a right axis deviation) when the LV conduction is faster and conversely, decreases (towards left axis deviation) when the RV conduction is faster.

Another interesting takeaway observation that can be made on Fig. 3.11 is the fact that the QRS axis values are always very close to each other, except when computed from leads I and III. The QRS axis computed from the activation map, which is considered to be the reference computation method, are well correlated from the computations made with leads I and aVF. This observation reinforces the suggestion that this method is the to be preferred when the activation map is not available. The standard clinical QRS axis estimation method (iso) is not very far either but can only yield values at $\pm 15^\circ$, without interpolation. From now on, unless explicitly mentioned, all QRS axis computed from ECG will be computed based on leads I and aVF.

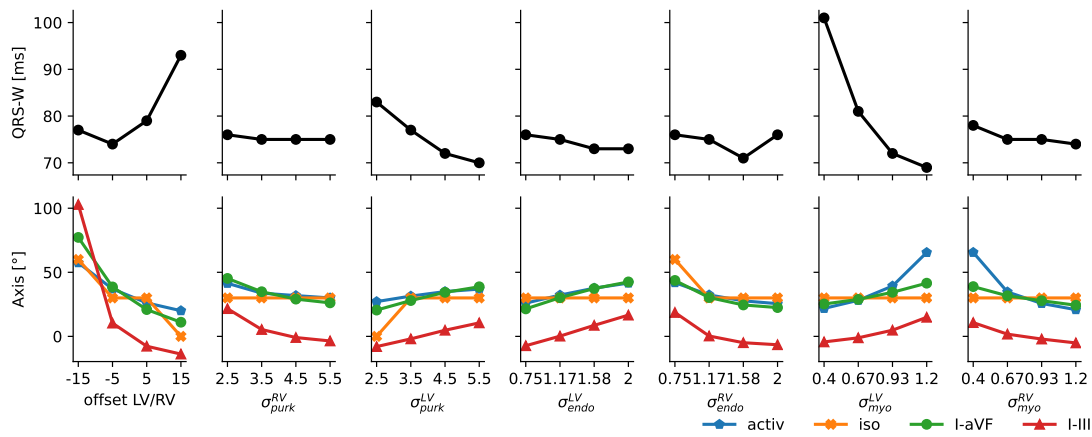


Fig. 3.11.: Variations of the QRS duration and axis for relevant parameters. The geometry and variation intervals are those of healthy simulations. The colors indicate the computation method for the QRS axis: from the activation map (blue), from the most isoelectric derivation (orange), from leads I and aVF (green) and from leads I and III (red).

Statistical study

In addition to the previous study, this section presents a deeper analysis of the correlation that exists between the electrophysiological model parameters and the waves extracted from the ECG. A total of 2000 simulations were run, allowing a complete exploration of the parameters space and a comprehensive understanding of the model's behavior when multiple parameters vary at the same time.

The parameters are taken from a Latin Hypercube Sampling (LHS) method. This method is flexible because it does not make any assumptions on the number of samples and furthermore ensures that the set of random parameter values is representative of the multidimensional dataset.

Discussion

The sensitivity analysis performed on the model show that all the selected parameters have significant influence on the simulation results. However, it can be noted that the real world ECG tracings have a much higher variability than those generated by the model, as presented in Fig. 3.14 for healthy cases.

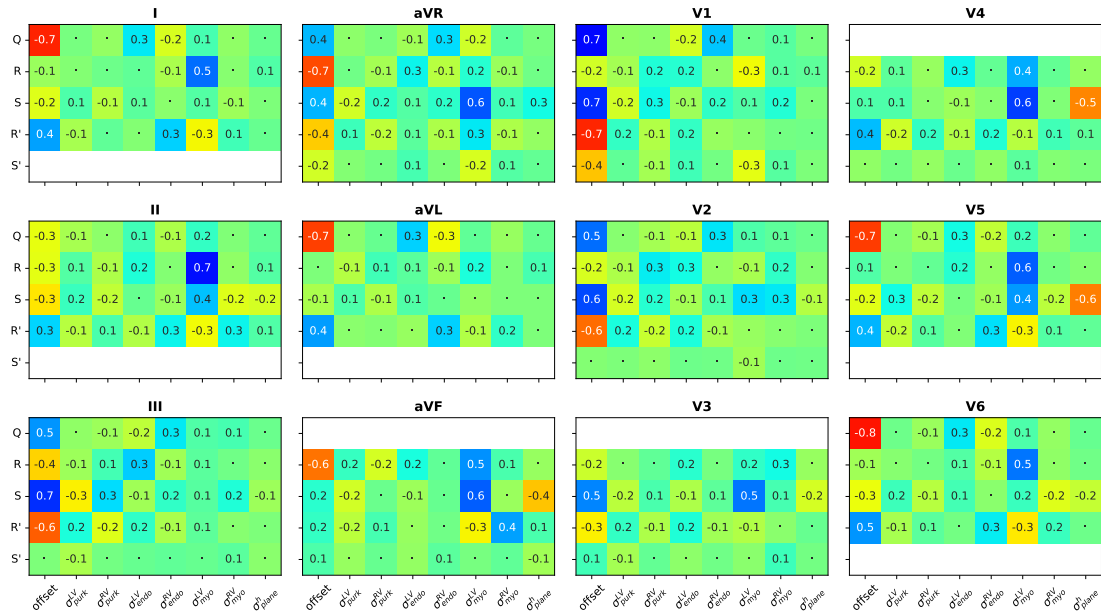


Fig. 3.12.: Correlation between the QRS waves (Q, R, S, R', S') and the model's parameters. Coefficients are replaced with '.' when not significant (p -value > 0.001) and left blank when no wave is present in the derivation. Please refer to Fig. 3.13 for the color scale.

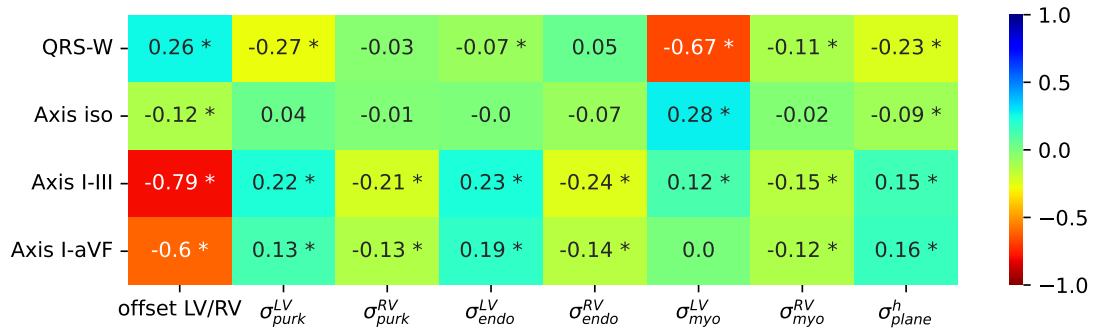
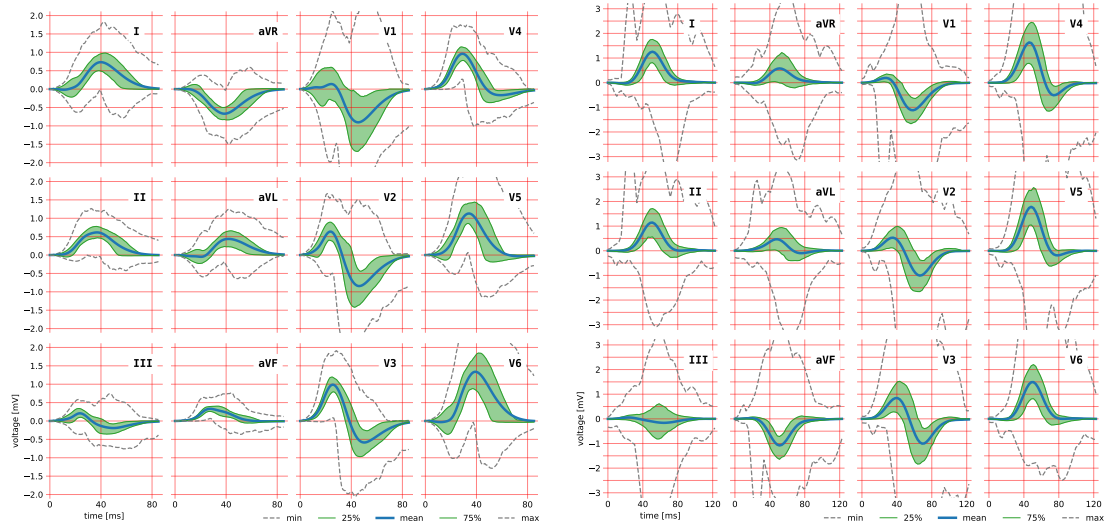


Fig. 3.13.: Correlation between the computed ECG features and the model's parameters. Significant results (p -value<0.001) are indicated with “*”.



(a) Envelope of the ElecModel 12-lead recordings for 2000 healthy simulations. **(b)** Envelope of the 459 healthy 12-lead recordings from [Ribeiro et al., 2020].

Fig. 3.14.: Comparison between the ECG tracings obtained with the model and those from the database presented in section 1.3.2.

3.5 Pathological simulations

The electrophysiological model presented in this chapter has been calibrated on healthy and DCM geometries. This section is dedicated to the study of how electrical condition affects the output.

3.5.1 Simulating bundle branch blocs

This section presents the simulation results of complete BBB on DCM geometry. Despite the global reduction of the conduction velocities associated with the dilation of the ventricles, it is assumed that both the muscle and Purkinje network are still functional and not altered further the block. In this sense, the Purkinje network still transmits the electrical signal at a high speed to the distal myocardial tissue, whenever it is activated. In the case of complete BBB in one side of the heart, the depolarizing wave, typically coming from the healthy His bundle, crosses the septum and activates the other Purkinje network, propagating the signal in the remaining tissue. This is particularly visible on the ECG tracings, where the signal is notched and exhibits ‘M’ or ‘W’ shapes, reflecting the fact that ventricles have been activated sequentially.

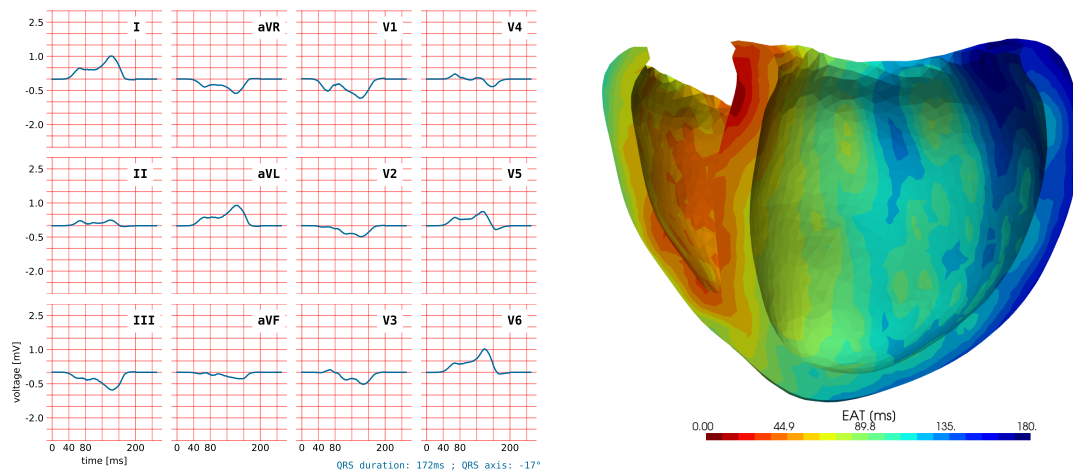


Fig. 3.15.: Electrophysiological simulation of a complete LBBB, QRSd=172ms, QRSa=-17°, max (EAT)=180ms.

Fig. 3.15 shows the ECG tracings and activation map resulting from a LBBB. The QRS duration is 172ms and axis -17°. The LLW has a delayed activation, visible in dark blue in the activation map. The ECG shows a dominant S wave in V1 and large R wave in leads I, aVL, V5 and V6. We can note the absence of Q wave in leads I, V5 and V6. Finally, the notch, visible in V1 and V6, is typically associated to complete LBBB with preserved conduction properties, for instance without myocardial infarction.

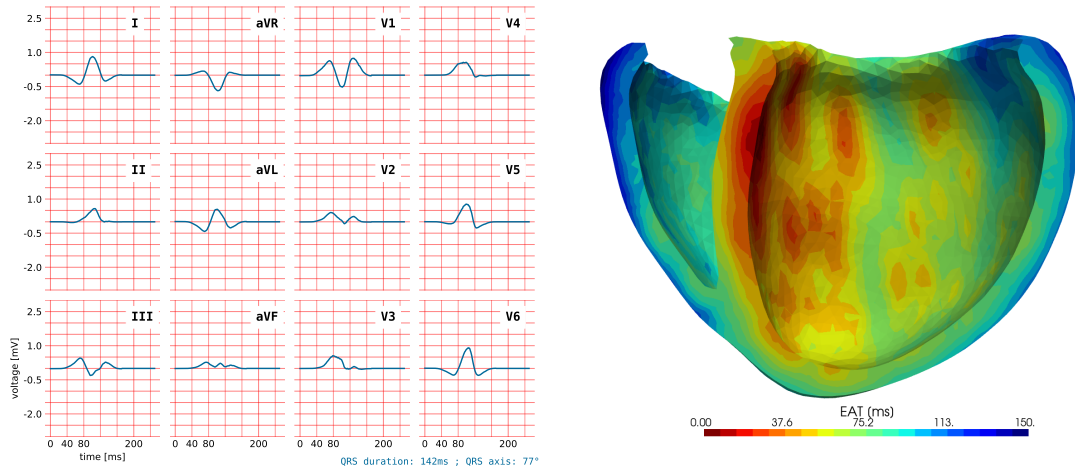


Fig. 3.16.: Electrophysiological simulation of a complete RBBB. $QRS_d=142\text{ms}$, $QRS_a=77^\circ$, $\max(EAT)=150\text{ms}$.

Similarly, a complete RBBB is presented Fig. 3.15, resulting in a 142ms QRS duration and 77° QRS axis. Again, the RSR' pattern observed in leads V1-3 with an 'M-shaped' signal is typically associated with RBBB.

3.5.2 Simulating fascicular blocks

Based on the identification of the Purkinje end nodes visible in Fig. 2.11, it is possible to induce a fascicular block, either on the anterior branch (LAFB) or posterior one (LPFB) of the IV.

3.5.3 Simulating ischemia

Simulating infarcted areas is also possible within the ElecModel. This consists in locally modifying the conduction velocities, near the infarcted area. Several methods for defining the areas are implemented, either growing from a seed given its 3D coordinates and area size, or based on the AHA regions (Fig. 2.6b). Defining a gradient for smooth transition between healthy and diseased tissue is also implemented.

3.5.4 Discussion

These simulation results show that the electrophysiology model is able to reproduce simple pathologies observed in heart failure patients such as complete and incomplete BBB, as well as myocardial infarction. The ECG tracings exhibit behaviors typically associated with these conditions. However, two notable limitations can be made on these results. First, the axis computed from the BBB simulations are classified as normal, although it should have been classified as right or left axis deviation for RBBB and LBBB

respectively. Instead, they lie in the border of the $[-30^\circ, 90^\circ]$ range associated with normal axis. This lack of variability of the QRS axis is also visible on Fig. 3.11 where almost all QRS axis are within the normal range, in spite of using parameters normally associated with pathological simulations. This behavior may be related to the important restrictions in the conduction pathways possibly used by the depolarizing wave, and could be explained by the following points:

1. the Purkinje systems used in these simulations do not vary much and offer only one preferred pathway for the propagation of the electrical signal. Since the first activation on the endocardium occurs on the septum and since the Purkinje network is mostly oriented towards the apex, the posterior and anterior walls, the propagation is mainly oriented towards the apex ;
2. the short-axis plane defined as the limit for the endocardial conductivity may influence the way the wave propagates to the basal part of the heart. For instance in RBBB, the pathway of the depolarizing wave is not purely left to right (leading to an axis close to 150°), but also presents an apical to basal current flow on a direction perpendicular to the latter one, diminishing the weight associated to lateral propagation.

3.6 Pacing simulation

3.6.1 Cardiac stimulation and defibrillation

The electrical stimulation of cardiac tissue has three clinical applications: cardiac pacing, cardiac defibrillation, and cardiac resynchronization. Cardiac pacing, on the other hand, is used to maintain a physiological activation in case of failing or interrupted conduction system. Defibrillation is used to stop uncontrolled multiple reentrant activation causing fibrillating muscle contractions and falls out of the scope of the current manuscript. Resynchronization is used for reCOORDINATING cardiac segments not contracting at the appropriate timing within the cardiac cycle.

Modern CRT devices embed electronic components including a microprocessor and a battery with a lifespan up to six to twelve years [Munawar et al., 2018]. Efficient algorithms allow the controller to adjust pulses to make them as physiological as possible and deliver the required cardiac output. Rate modulation rely on minute ventilation, heart contractility or other factors, in order to adapt the pacing.

Leads are plugged in the CRT device and carry the electrical signal to the electrodes, at the pacing sites. They are insulated wires inserted through veins and placed or screwed in the cardiac muscle with the help of a removable stylet. The ideal location for the

electrodes is the endocardium because of the high density of Purkinje fibers that allow the signal to spread rapidly. Implanters typically enter the lead in the right ventricle through the atria. Entering the LV directly is more challenging given the high pressures in the arterial system, and the introduction of a lead through the left valves may cause further complications. In routine, today the coronary sinus route provides an elegant way to stimulate the left ventricle, but epicardially [Daubert et al., 2017]. In case of failure of placing the LV electrode by the coronary sinus route, surgical epicardial pacing approach can be an alternative. Recent re-discovery of direct His-bundle pacing or left bundle branch pacing are re-emerging. It is the best location in case of complete block (if the global conduction properties of the free-running Purkinje fibers are preserved) since it would rapidly propagate the signal to all segments of the heart.

3.6.2 Implementation of cardiac stimulation

This section is dedicated to the modelling of cardiac stimulation and more globally, on the implementation of the electrophysiological model. Indeed, the stimulation is the last action altering the activation map, as it occurs on top of the spontaneous activation. After the latter has been computed once, any stimulation point added to the simulation can drastically change the activation map. For instance, if the pacing occurs before the spontaneous activation, then all propagations have to be recomputed, including the myocardium and the Purkinje network. Moreover, because the propagation is faster in the Purkinje network than in the myocardium and the endocardium, distal tissue might be activated by a Purkinje-Muscle Junction (PMJ) node before the cell-to-cell depolarization. In that case, this PMJ becomes a new source for cell-to-cell depolarization. In this scenario, the PMJ node is treated as a pacing point.

We can distinguish two types on pacing points, whether they are located within the myocardium, or on the Purkinje network.

Myocardial pacing

When the pacing occurs in the myocardium, the pacing points are added to the onset points list without any further modification. In this case, an electrical depolarization will occur at the pacing time and start to propagate to neighbouring cells. If this propagation reaches a Purkinje node that has not been depolarized yet, it can be activated and initiate a propagation. In this case, this point becomes a Purkinje pacing point.

Purkinje pacing

For any point $p_k \in \Omega$ labelled as Purkinje pacing, it is projected to the nearest purkinje node (P_k). If it is already on the graph, $p_k = P_k$. Then, P_k is used to compute a geodesic distance on the network, stored as $d_k = D(P_k)/\sigma_{P_k} + t_k$ where D is the distance operator

giving the distance from P_k to the network's nodes, σ_{P_k} the purkinje speed and t_k the pacing time.

The final Purkinje activation map is obtained by taking the minimum arrival time for all Purkinje points: $d = \min_k d_k$. Then, the PMJ points are extracted and added to the onsets points list. An example of a Purkinje stimulation on a LPFB simulation is presented Fig. 3.17. The stimulation is located on the anterior part of the LVFW and leads to the reactivation of the anterior fascicle, as well as the optimized recomputation of the activation time for the surrounding PMJ points.

The complete electrophysiological pipeline is represented Fig. 3.18. It shows how the activation map is iteratively recomputed in the case where a point on the Purkinje network is activated after the closest point on the myocardium. Indeed, the earliest myocardial depolarization should have activated the network. The global propagation is then recomputed until no such case exists.

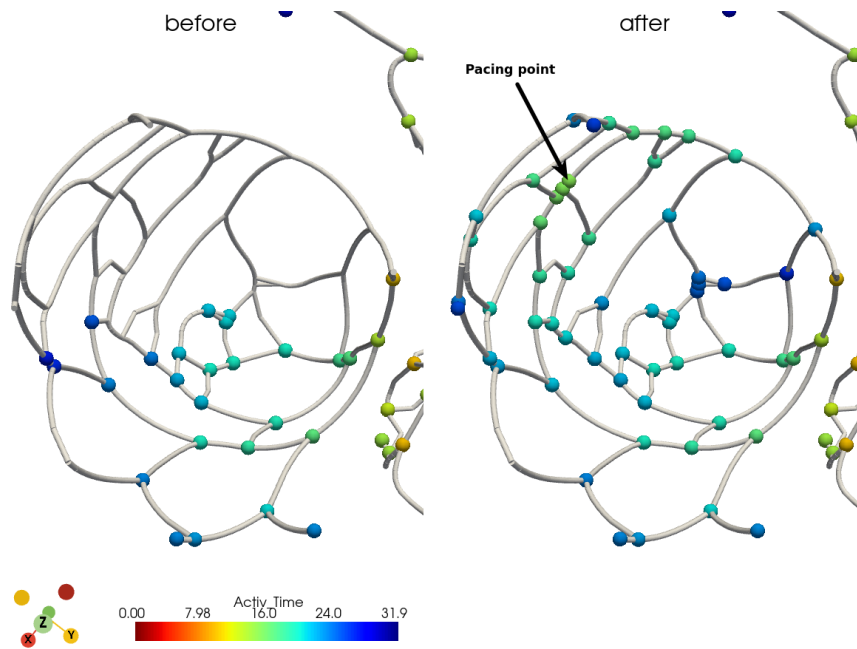


Fig. 3.17.: Onset points before and after applying the pacing protocol on a LPFB. In this figure, IV is activated on the septum at $t=10\text{ms}$ and the pacing occurs at $t=15\text{ms}$. The activation time of each point is derived from the shortest distance to either the physiological His point or the pacing point.

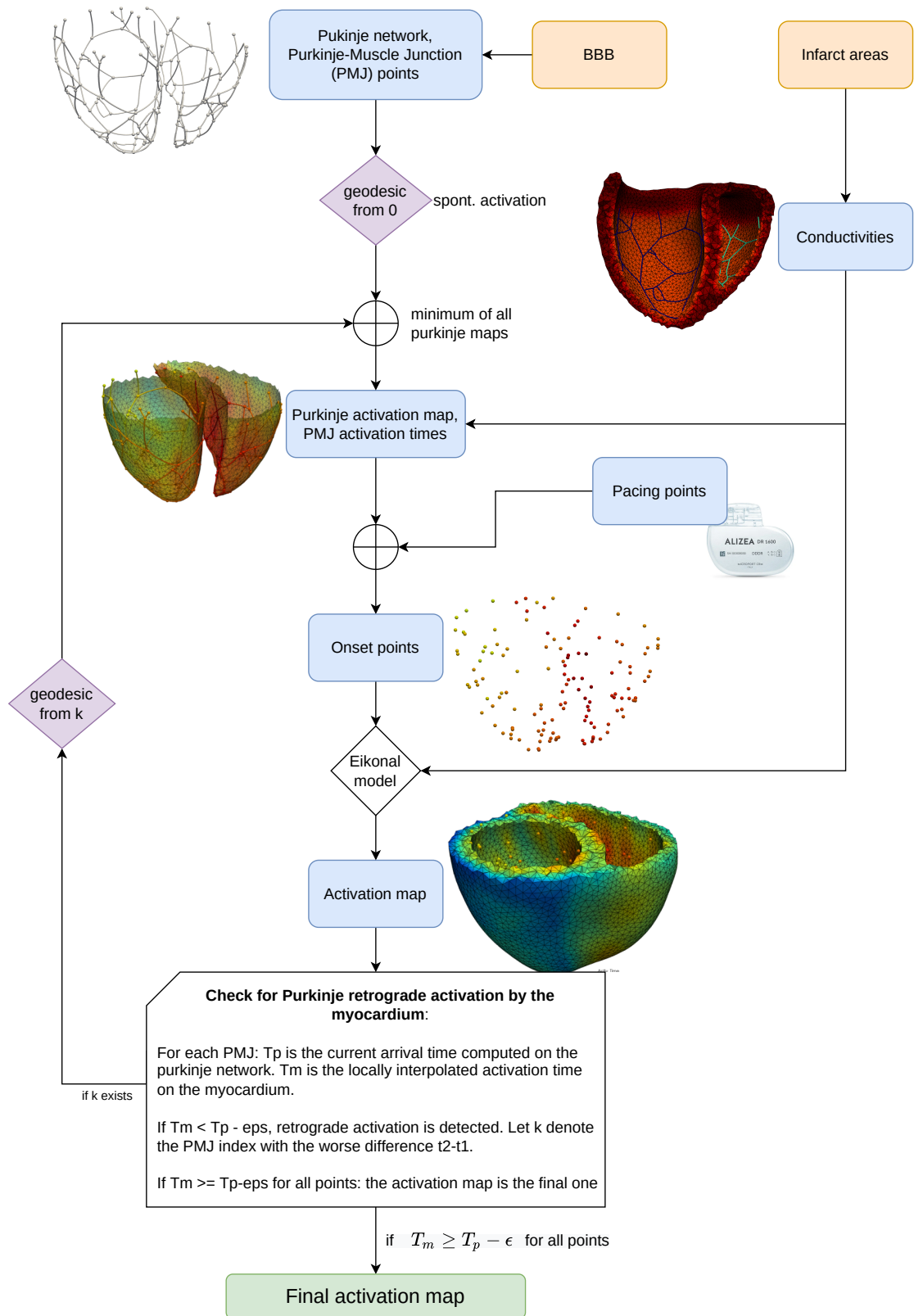


Fig. 3.18.: Description the ElecModel's eikonal module implementation. The anatomical data, including the biventricular mesh and the Purkinje network, have already been generated. At the top of this scheme, the Purkinje network may be modified in case of BBB, in all cases generating a set of Purkinje-Muscle Junction (PMJ) points. Similarly, myocardial infarction affects the local conductivity condition.

3.6.3 Simulating CRT

This section presents the simulation results for two pacing configurations on dilated geometry. In these simulations, the spontaneous activation has been deactivated (capture), so that the only source for the electrical depolarization are the stimulation points.

Fig. 3.19 shows the ECG tracings and the activation map for a LVFW pacing. As soon as it reached the endocardial Purkinje network, the depolarization quickly propagates through the LV to the septum, then is slowed down throughout the septum before reaching the RV Purkinje.

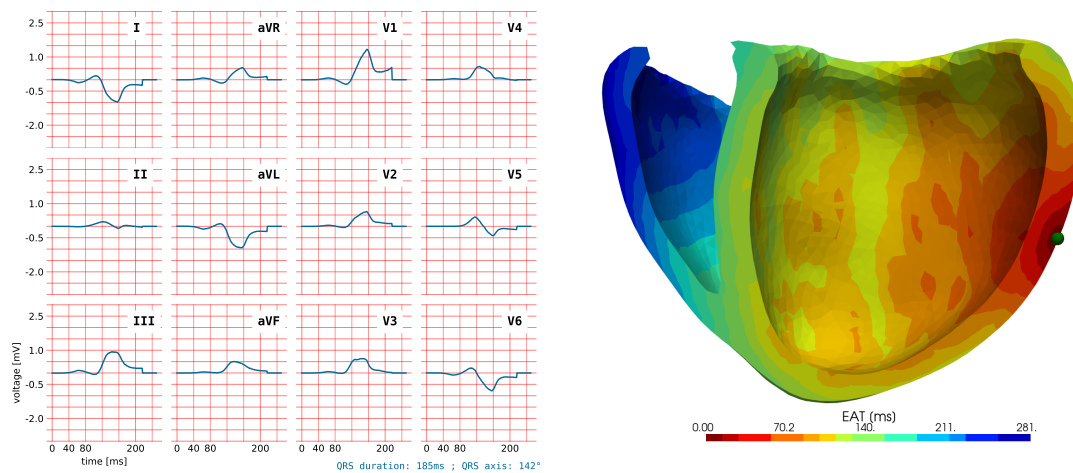


Fig. 3.19.: Electrophysiological simulation of a LVFW pacing on a DCM geometry, in capture. The stimulation point is located on the right of the figure (the green point on the IV epicardium). QRSd=185ms, QRSa=142°, max (EAT)=281ms.

Fig. 3.20 shows the ECG tracings and the activation map for a BiV pacing (RV septum and LVFW). With this pacing configuration, the QRS duration (99ms) is under the pathological 120ms threshold.

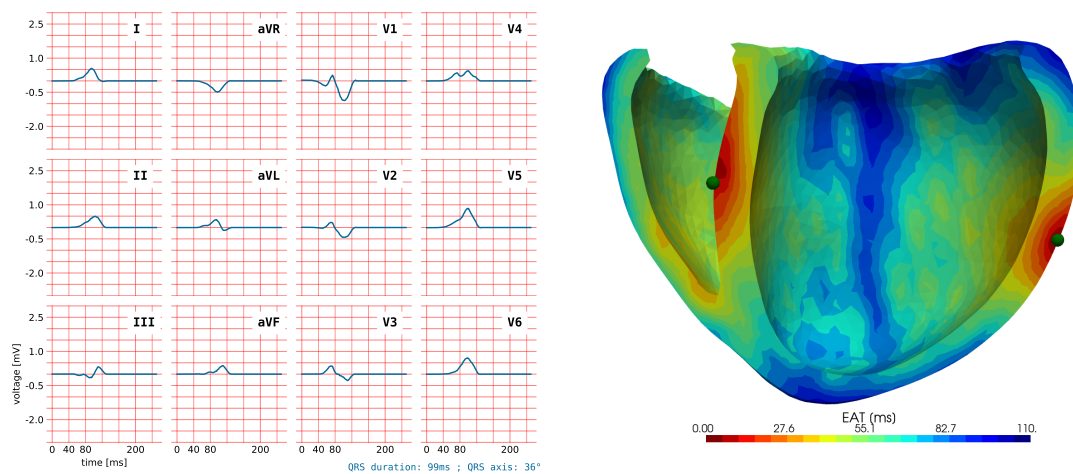


Fig. 3.20.: Electrophysiological simulation of a BiV pacing on a DCM geometry, in capture. QRSd=99ms, QRSa=36°, max (EAT)=110ms.

3.7 Conclusion

This electrophysiology model presented in this chapter is able to generate realistic activation map, reflecting the electrical activity at the organ scale. The anisotropic depolarization is computed using the Eikonal model on a rectilinear grid, which reduces the computation time for the generation of the activation map. Additionally, a fast ECG generation model has been presented and enables to characterize the biventricular depolarization through the QRS complex. Several tools allowing for the processing of these signals have been implemented and will also be used for the personalization of the model in chapter 5. A complete description of the electrophysiological simulation pipeline has been given in Fig. 3.18 and shows that it is possible to simulate various pathologies, including complete and incomplete BBB, fascicular blocks, and myocardial infarction.

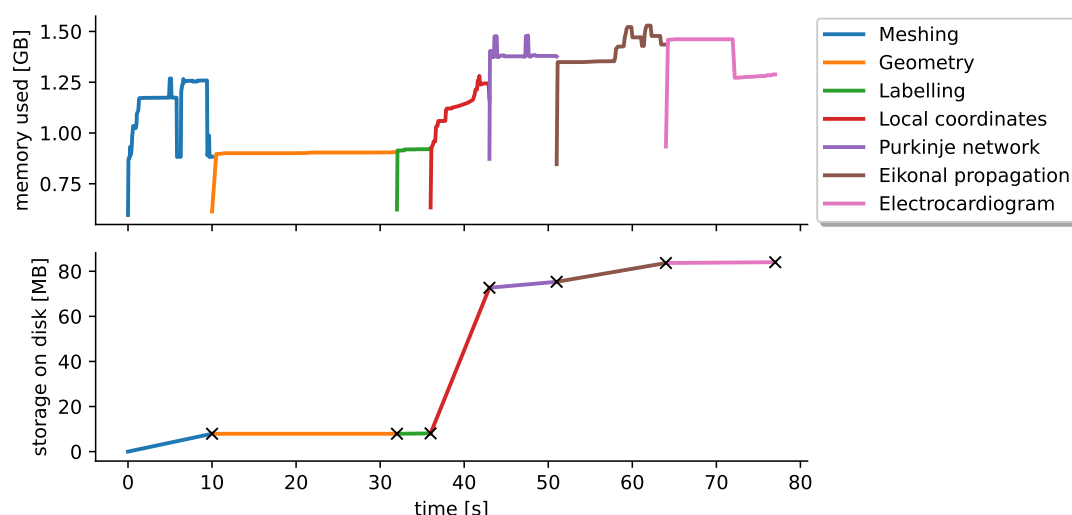


Fig. 3.21.: Resources used during an electrophysiological simulation of sinus rhythm.

Finally, Fig. 3.21 shows the resources used by the ElecModel during a sinus rhythm electrophysiological simulation, without the anatomical deformation model. The computation time of the electrophysiology model is less than 30s for this healthy simulation. If the activation map must be recomputed, as described in Fig. 3.18, the simulation will be longer (adding ten seconds per recomputation). It is also noted that the simulation's output is only 80MB of hard drive storage.

The output of the electrophysiology model consists both in the ECG tracings and the activation map, but only the latter is required for the mechanical simulations. Indeed, the arrival time of the depolarization wave indicates the beginning of the cells' contraction. Globally, both the anatomical and electrophysiological simulation results are required to run the mechanical simulation.

Electromechanical model

4.1	Solid mechanics	63
4.1.1	Lagrangian description of the finite strain theory	63
4.1.2	Elasticity theory	64
4.1.3	Balance equations	65
4.1.4	Weak formulation	65
4.1.5	Discretization of the weak formulation	66
4.1.6	Implicit integration scheme	68
4.2	Implementation in a simulation framework	70
4.2.1	Introduction to SOFA	70
4.2.2	Implementation's strategy	71
4.2.3	Biophysical material law	72
4.2.4	Active contraction	74
4.2.5	Heamodynamics	76
4.2.6	Constraint-based implementation of the valves system	78
4.2.7	Boundary conditions	80
4.2.8	Conclusion	81
4.3	Results	83
4.3.1	Normal heart	83
4.3.2	DCM with LBBB	85
4.3.3	Mechanical simulation of the CRT	85
4.3.4	Sensitivity analysis	86
4.3.5	Discussion	88
4.3.6	Computation time and influence of the discretization	89

The models presented in the previous chapters allow for the simulation of the electrical depolarization on a given geometry, at the organ scale. After the electrical depolarization, the muscle cells in the heart release ions that lead to sarcomere shortening and active muscle contraction. This contraction is the origin of the pumping function of the heart, but several other phenomena have been considered to fully characterize the mechanical cardiac function.

In the case of cardiac dyssynchrony, most often an electrical delay induces a prolonged QRS activation and causes cardiac segments to contract in a non-harmonious way, which

may lead to a reduction of the ejection fraction. However, some desynchronized hearts exhibit a QRS complex around or less than 120ms, thus included in the classically admitted normal range, but still present abnormalities in the contraction pattern, described as pure intraventricular dyssynchrony, and exhibiting some late segments still contracting although valves are closed [Cazeau et al., 2008]. These authors introduced then eighteen electromechanical indices that can be grouped together to provide an electromechanical assessment of the dyssynchrony [Cazeau et al., 2019]. While classical QRS-based assessments are associated with 30-35% non-responders, [Cazeau et al., 2000; Abraham et al., 2002] showed that the appropriate selection of electromechanical indices allows to describe dyssynchrony. With this model, they were able to improve the success rate from 65 to 85% [Cazeau et al., 2003].

An important part of the IPRC project relies on the implementation of this model and its coupling with the electromechanical heart model, in order to compute the delays on the simulated cardiac cycles. This chapter then presents the theoretical framework and the implementation of the heart model's mechanical part.

Analyzing the mechanical behavior of biological tissue may be challenging. Soft tissue are highly anisotropic and heterogenous, and they are often coupled with an electrophysiological activity. Moreover, the anatomical structures surrounding the heart, such as valves, chordae tendineae, pericardium and the arteries, add a layer of complexity to their modelling.

Early approaches for modelling the soft tissue behavior assumed a linear elastic behavior [Cotin et al., 2000]. However, deformations of biological materials are known to be of the order of 50%-100% [Mirsky, 1973], thus invalidating the assumptions inherent to the linear theory of small deformations. According to the analysis performed in [Yingchoncharoen et al., 2013], left ventricle global longitudinal strain is above 20% and global radial strain above 50%. The deformations are larger than a few percent and impose the large strain theory.

4.1 Solid mechanics

The area of continuum mechanics known as solid mechanics focuses on the motion and deformation of solid materials, under the action of both internal and external forces.

4.1.1 Lagrangian description of the finite strain theory

In continuum mechanics, the finite strain theory - also called large strain theory - deals with deformations in which strains and/or rotations are large enough to invalidate assumptions inherent in infinitesimal strain theory.

Let $\mathbb{E}^d = \text{span}\{\mathbf{e}_i\}$ be the orthonormal Euclidian vector space of dimension d . The simulated object is defined as the bounded domain $\Omega \subset \mathbb{E}^d$. $t = t_0$ defines the initial (rest or undeformed) position. The rest positions are $\mathbf{X}(t = t_0) \in \Omega(t_0)$, where the material coordinates, \mathbf{X} , are the independent variables of the system (reference configuration).

To get the position vector of a material point in the deformed domain at a time t (current configuration), we use the following rigid transformation

$$\mathbf{x}_t(\mathbf{X}) = \mathbf{R}_t \cdot \mathbf{X} + \mathbf{T}_t \quad (4.1)$$

where \mathbf{R}_t is the rotation matrix and \mathbf{T}_t the translation vector. Dropping the time notation \cdot_t , the displacement vector field is given by

$$\mathbf{u}(\mathbf{X}) = \mathbf{x}(\mathbf{X}) - \mathbf{X} \quad (4.2)$$

Deformation gradient

Let's derive the transformation \mathbf{x} with respect to the material coordinates:

$$\mathbf{F} = \nabla_{\mathbf{X}} \mathbf{x} = \mathbf{I} + \nabla_{\mathbf{X}} \mathbf{u} \quad (4.3)$$

The deformation gradient transforms a small segment $d\mathbf{x}$ from spacial to material coordinates: $d\mathbf{x} = \mathbf{F} \cdot d\mathbf{X}$. More generally, Nanson's formula is an important relation that can be used to relate areas in the current configuration to areas in the reference configuration and vice versa. This formula states that $da \cdot \mathbf{n} = JdA\mathbf{F}^{-T} \cdot \mathbf{N}$ where $J = \det \mathbf{F}$, da is an area of a region in the current configuration, dA is the same area in the reference configuration, and \mathbf{n} is the outward normal to the area element in the current configuration while \mathbf{N} is the outward normal in the reference configuration. Similarly, Nanson's formula for volume change implies $dv = JdV$.

Strain measures

The strain measures the change of shape between two particles in an infinitesimal closed space of continuous material.

The right Cauchy–Green deformation tensor is independent of the rotation:

$$\mathbf{C} = \mathbf{F}^T \mathbf{F} \quad (4.4)$$

The Green-Lagrangian strain tensor is a measure of how \mathbf{C} differs from \mathbf{I} :

$$\mathbf{E} = \frac{1}{2} (\mathbf{C} - \mathbf{I}) \quad (4.5)$$

4.1.2 Elasticity theory

The Cauchy stress tensor is used to express uniaxial and shear stresses across a surface with normal n . An infinitesimal force can be expressed as:

$$df_t = t \, da = \sigma^T \cdot n \, da = \sigma^T J \, dA \mathbf{F}^{-T} \cdot \mathbf{N} = \mathbf{P} \cdot \mathbf{N} \, dA \quad (4.6)$$

with \mathbf{P} the first Piola-Kirchhoff (FPK) tensor and σ :

$$\sigma = \begin{bmatrix} \sigma_x & \tau_{xy} & \tau_{xz} \\ \tau_{yx} & \sigma_y & \tau_{yz} \\ \tau_{zx} & \tau_{zy} & \sigma_z \end{bmatrix} \quad (4.7)$$

where σ and τ are the uniaxial and shear stresses.

To express the stress in a Lagrangian formulation $df_t = \mathbf{F} \cdot dF_t$:

$$dF_t = \mathbf{F}^{-1} \mathbf{P} \cdot \mathbf{N} \, dA = \mathbf{S} \cdot \mathbf{N} \, dA \quad (4.8)$$

where $\mathbf{S} = \mathbf{F}^{-1} \mathbf{P}$ is called the Second Piola-Kirchhoff (SPK) stress tensor and is symmetric.

Constitutive model

The relation between the amount of deformation and the response of the material is called the constitutive relation. An hyperelastic material is a type of constitutive relation

for which the relation between the strain and the stress is derived from a scalar-valued strain energy density function $W(\mathbf{F})$.

For an hyper-elastic material, the SPK tensor is defined as:

$$\mathbf{S} = \frac{\partial W}{\partial \mathbf{E}} \quad (4.9)$$

The FPK tensor is defined as:

$$\mathbf{P} = \frac{\partial W}{\partial \mathbf{F}} = \mathbf{F} \cdot \frac{\partial W}{\partial \mathbf{E}} \quad (4.10)$$

4.1.3 Balance equations

The equations that describe the deformation of a solid body in continuum mechanics are governed by a set of laws that relate the kinematic quantities of the system. In Lagrangian description:

Balance of Mass	$\rho_0 - J\rho = 0$
Balance of Linear Momentum	$\rho_0 \ddot{\mathbf{x}} - \nabla_{\mathbf{x}} \cdot \mathbf{P} - \rho_0 \mathbf{b} = 0$
Balance of Angular Momentum	$\mathbf{F} \cdot \mathbf{P}^T = \mathbf{P} \cdot \mathbf{F}^T$
Balance of Energy	$\rho_0 \dot{u} = \mathbf{S} \cdot \dot{\mathbf{E}} + \nabla_{\mathbf{x}} Q - \rho_0 \phi = 0$

with Q the heat flux vector, ϕ the heat source, and \mathbf{b} the vector of external forces that act everywhere within the domain.

Since the simulated myocardial tissue is assumed to have constant density throughout the simulation and is only represented by the symmetric SPK stress tensor, we will assume that the laws of conservation of mass and angular momentum are always respected. Moreover, heat is not considered in the current model. The only law remaining is the conservation of linear momentum.

4.1.4 Weak formulation

The balance of linear momentum constitutes a non-linear PDE with boundary conditions, where the displacement vector \mathbf{u} (from eq.4.2) is the unknown on the domain Ω . The FEM consists in using a piecewise approximation of \mathbf{u} , noted \mathbf{u}^h and defined over simple topological elements. The balance of linear momentum then reads

$$\rho_0 \ddot{\mathbf{x}} - \nabla_{\mathbf{x}} \cdot \mathbf{P}(\mathbf{u}^h) - \rho_0 \mathbf{b} = R \quad (4.11)$$

where R is the residual vector from the approximation error. To ensure that a unique solution does exist, the usual approach consists in multiplying the PDE by a test function w

and by integrating the resulting equation over the computational domain. The test function is chosen to be zero where an essential boundary condition is imposed. The weak formulation leads to a minimization of the residual R in the weak sense.

After converting the non-symmetric stress tensor \mathbf{P} to its symmetric form $\mathbf{P} = \mathbf{F}\mathbf{S}$, the weak formulation of the dynamical system is

$$\underbrace{\int_{\Omega_0} \mathbf{F}\mathbf{S} : \nabla_{\mathbf{X}} w \, dv}_{\text{Internal virtual work}} - \underbrace{\int_{\Omega_0} \rho_0 \ddot{\mathbf{x}} \cdot w \, dv}_{\text{Virtual inertia}} - \underbrace{\int_{\Omega_0} \rho_0 \mathbf{b} \cdot w \, dv - \int_{\Gamma_t} \mathbf{t} \cdot w \, ds}_{\text{Virtual load work}} = 0 \quad (4.12)$$

subject to $\mathbf{u}^h = \mathbf{u}_g$ on Γ_u . $\Gamma = \Gamma_t \cup \Gamma_u$ is the boundary of the computational domain Ω . The imposed traction \mathbf{t} and displacement \mathbf{u}_g are respectively the natural and essential boundary conditions.

4.1.5 Discretization of the weak formulation

Shape functions

To solve the weak formulation of equation 4.12, the domain Ω is split into n_e small geometrical elements. To ensure a continuous approximation of the functions and their derivatives over the elements, we define shape functions N_i , that form an interpolation of the element nodal values. For instance, to compute the approximation of the field \mathbf{u}^h and its derivative at a given location \mathbf{X} in an element:

$$\mathbf{u}_e^h(\mathbf{X}) = \sum_{i=0}^{n_e-1} N_i(\mathbf{X}) \mathbf{u}_i \quad \text{and} \quad \nabla_{\mathbf{X}} \mathbf{u}_e^h = \sum_{i=0}^{n_e-1} \mathbf{u}_i \otimes \nabla_{\mathbf{X}} N_i \quad (4.13)$$

Using $\mathbf{u} = \mathbf{x} - \mathbf{X}$ in $\nabla_{\mathbf{X}} \mathbf{u}$, the deformation gradient is expressed with

$$\mathbf{F}_e = \sum_{i=0}^{n_e-1} \mathbf{x}_i \otimes \nabla_{\mathbf{X}} N_i \quad (4.14)$$

which requires the spatial coordinates \mathbf{x} to be computed, as well as the precomputed shape function derivative.

Isoparametric elements

For simple geometrical elements (such as triangles or tetrahedra), it is possible to define a transformation mapping between the deformed element and a reference one, as

illustrated in Fig. 4.1. The isoparametric configuration Ω_\square has its coordinate system aligned with the euclidian basis, thus simplifying the computations.

$$\mathbf{X}_e(\xi) = \sum_{i=0}^{n_e-1} \mathbf{X}_i N_i(\xi) \quad (4.15)$$

with $\xi = [\xi, \eta, \zeta]$ the local (or canonical) coordinates in the reference configuration.

The term isoparametric refers to the property of the shape functions N_i to describe both the element's geometrical (e.g. the position vector field) shape as well as the displacements (e.g. the displacement vector field) within the element.

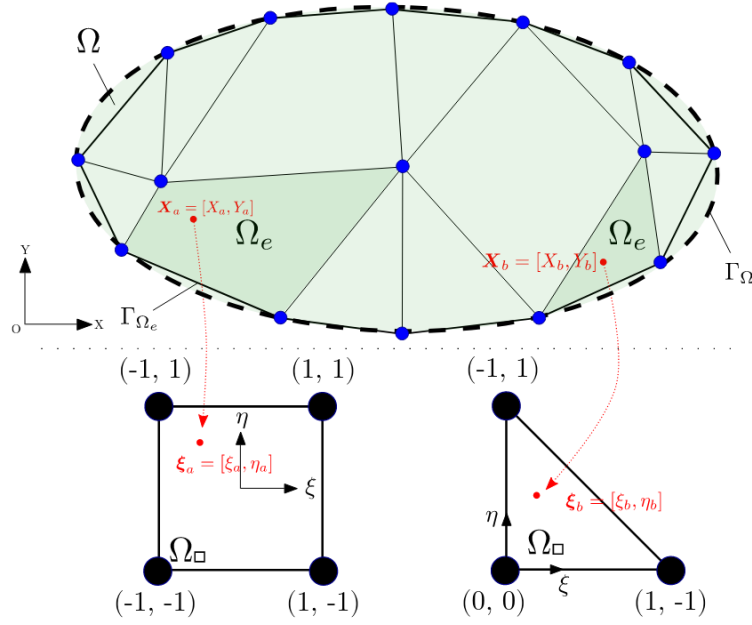


Fig. 4.1.: Transformation of the coordinates of a point in Ω_e to its canonical coordinates. Source: [Brunet, 2020].

The Jacobian of the transformation mapping is:

$$\mathbf{J}_e = \frac{d\mathbf{X}}{d\xi} = \sum_{i=0}^{n_e-1} \mathbf{X}_i \otimes \nabla_\xi N_i \quad (4.16)$$

which allows to compute the shape function's gradient with respect to material coordinates:

$$\nabla_{\mathbf{X}} N_i = \mathbf{J}_e^{-1} \nabla_\xi N_i \quad (4.17)$$

Then, the displacement gradient (eq.4.13) can be computed based on the displacement field and precomputed data depending on initial conditions:

$$\nabla_{\mathbf{X}} \mathbf{u}_e^h = \sum_{i=0}^{n_e-1} \mathbf{u}_i \otimes (\mathbf{J}_e^{-1} \nabla_{\xi} N_i) \quad (4.18)$$

Integration of the weak formulation

The integration of eq. 4.12 is performed on the discretized domain Ω . Any field function f can be approximated by a sum of integrals over element domains Ω_e , as well as on the reference element given the change of variable $d\mathbf{X} = \mathbf{J}_e d\xi$:

$$\int_{\Omega} f(\mathbf{X}) d\mathbf{X} \approx \sum_e \int_{\Omega_e} f(\mathbf{X}) d\mathbf{X} = \sum_e \int_{\Omega_{\square}} f(\xi) \mathbf{J}_e(\xi) d\xi \quad (4.19)$$

To actually compute the integrals, we use the Gauss numerical integration method. The integration is approximated by a weighted sum of the integrand taken at certain points inside the element. These points are called the Gauss - integration - points.

$$\int_{\Omega_{\square}} f(\xi) \mathbf{J}_e(\xi) d\xi \approx \sum_{I=1}^{n_I} f(\xi_I) \mathbf{J}_e(\xi_I) w_I \quad (4.20)$$

where ξ_I are canonical coordinates of the I^{th} Gauss points, and w_I its weight. A description of the shape functions N_i , their gradient with respect to canonical coordinates $\nabla_{\xi} N_i$, the location ξ_I of Gauss points and their weights w_I for various isoparametric elements can be found in the work of [Wriggers, 2008] and [Fortin et al., 2006].

For example, to compute the contribution of the internal virtual work inside an element e :

$$R(\mathbf{u}) = \int_{\Omega_e} \mathbf{F}_e \mathbf{S}_e \cdot \nabla_{\mathbf{X}} N_i dv \quad (4.21)$$

$$\approx \sum_{I=1}^{n_I} \mathbf{F}_I \mathbf{S}_I \mathbf{J}_e(\xi_I) w_I \cdot \nabla_{\xi} N_i \quad (4.22)$$

4.1.6 Implicit integration scheme

The discretized form of the weak solution eq. 4.12 is:

$$\mathbf{M}\ddot{\mathbf{u}} - \mathbf{R}(\mathbf{u}) - \mathbf{B} - \mathbf{T} = 0 \quad (4.23)$$

with $\mathbf{M}_{ij} = \int_{\Omega_e} \rho_0 N_i N_j d\mathbf{X}$ the mass matrix and ρ_0 the constant density, \mathbf{R} the internal forces (see eq. 4.22) and $\mathbf{B} + \mathbf{T}$ the external forces applied on the solid.

It can be transformed with $\ddot{\mathbf{x}} = \frac{\Delta \mathbf{v}}{\Delta t}$, $\mathbf{u} = \mathbf{x} - \mathbf{X}$, $\mathbf{F}(\mathbf{x}) = \mathbf{R}(\mathbf{u}) + \mathbf{B} + \mathbf{T}$

$$\mathbf{M} \Delta \mathbf{v} = \Delta t \cdot \mathbf{F}(\mathbf{x}) \quad (4.24)$$

This equation constitutes the main system that will be solved at each time step of the simulation. On the left hand side is the mass matrix and on the right hand side (RHS) the vector of external forces.

Using an implicit scheme ensures unconditional stability in the resolution of this system. The backward Euler scheme is used. It means that the RHS term will be computed at the next time step $t + \Delta t$. The approximation of $\mathbf{F}(\mathbf{x}(t + \Delta t))$ is given by a first order Taylor expansion:

$$\mathbf{M} \Delta \mathbf{v} = \Delta t \cdot \mathbf{F}(\mathbf{x}(t + \Delta t)) \quad (4.25)$$

$$= \Delta t \cdot \left(\mathbf{F}(\mathbf{x}(t)) + \Delta \mathbf{x} \cdot \frac{\partial \mathbf{F}}{\partial \mathbf{x}} \right) \quad (4.26)$$

$$= \Delta t \cdot \left(\mathbf{F}(\mathbf{x}(t)) + \Delta t \cdot \frac{\partial \mathbf{F}}{\partial \mathbf{x}} \mathbf{v}(t) + \Delta t \cdot \frac{\partial \mathbf{F}}{\partial \mathbf{x}} \Delta \mathbf{v} \right) \quad (4.27)$$

given that $\Delta \mathbf{x} = \Delta t(\mathbf{v}(t) + \Delta \mathbf{v})$ for an implicit scheme.

Rearranging the terms from the last equation and introducing the tangent stiffness matrix $\mathbf{K} = \frac{\partial \mathbf{F}}{\partial \mathbf{x}}$:

$$(\mathbf{M} - \Delta t^2 \cdot \mathbf{K}) \Delta \mathbf{v} = \Delta t \cdot \mathbf{F}(\mathbf{x}(t)) + \Delta t^2 \cdot \mathbf{K} \mathbf{v}(t) \quad (4.28)$$

This means that for each force acted upon the body, the formulation of both the forces $\mathbf{F}(\mathbf{x}(t))$ and their derivative with respect to nodes positions \mathbf{K} must be known.

Application to hyperelasticity

The tangent stiffness matrix, $\mathbf{K} = \frac{\partial \mathbf{R}}{\partial \mathbf{u}}$, has to be computed when using an implicit integration scheme:

$$\mathbf{K} = D\mathbf{R}(\mathbf{u}) \cdot \delta_u = \biguplus_e \sum_{i=0}^{n_e-1} \sum_{j=0}^{n_e-1} \int_{\Omega_e} \underbrace{\left[(\nabla_X^T N_i) \mathbf{S} (\nabla_X N_j) \mathbf{I} + \mathbf{B}_i^T \mathbf{C} \mathbf{B}_j \right]}_{\mathbf{K}_{ij}} \quad (4.29)$$

with \mathbf{B} a strain measure and the operator \biguplus_e defining the global system matrices assembly, which is described in [Brunet, 2020]. The stiffness matrix includes the rank-2 SPK tensor

\mathbf{S} and the rank-4 elasticity tensor $\mathbb{C} = \frac{\partial \mathbf{S}}{\partial \mathbf{E}}$. These two tensors, expressed in the reference coordinate system, fully describe the hyperelastic material.

4.2 Implementation in a simulation framework

In this section, two novel contributions are presented. First, a new implementation of the 3-element Windkessel model has been proposed and corrects the pressures profiles as compared to [Marchesseau, 2013]. The implementation of this model has been integrated within the Lagrangian constraint-based haemodynamic model resolution with a Crank-Nicolson scheme, in the `SofaCardiacModel` plugin. The second contribution consists in a new description of the mechanical model, through a fragmented scene-graph. This new structure reuses several components from SOFA core libraries and thus leads to less error-prone code, while using the latest SOFA version. Another important change is that the Lagrangian constraint-based haemodynamic model is integrated within the SOFA resolution pipeline and is now compatible with contacts resolution.

4.2.1 Introduction to SOFA

The mechanical model is implemented within SOFA (Simulation Open Framework Architecture), an open source framework intended for medical simulations [Allard et al., 2007; Faure et al., 2012]. The software is built to be modular, allowing several blocks to be developed independently and used in a uniformed way. The SOFA architecture relies on a multi-model representation, where all objects are connected with mappings. For instance, the myocardium can be decomposed into a tetrahedral volume implementing the finite element method (FEM) to solve the solid mechanics problem, an exterior triangle mesh allowing to compute contacts with the pericardium and a finer envelope for visualisation.

All these components are organized in a scene-graph, which is basically a python or xml file describing a tree-like structure where the leaves define components and their parameters. Each component implements a specific action and is called during the simulation by the core components of SOFA. Several components are required to run a mechanical simulation:

- **AnimationLoop**: this is the main component that triggers events and activates the required components in the scene-graph. Because our mechanical model uses Lagrangian constraints and collision, the `FreeMotionAnimationLoop` is necessary. It decomposes a simulation step into several computations and includes solving

all linear systems without constraints and solving all constraint-based systems separately [Duriez, 2013].

- **ODESolver**: implements the integration scheme, the temporal discretisation of the system. The `EulerImplicitSolver` implements the implicit Euler method.
- **LinearSolver**: implements the solving of $\mathbf{Ax} = \mathbf{b}$ linear systems and finding the solution $\mathbf{x}(t + \Delta t)$. For complex simulations, iterative methods are often preferred to direct ones and converge gradually to the solution vector \mathbf{x} by minimizing the residual $\mathbf{R} = \mathbf{Ax} - \mathbf{b}$. In SOFA and with iterative methods, the matrix \mathbf{A} is not inverted nor built, thus increasing performances. The `CGLinearSolver` implements the conjugate gradient (CG) method and is typically used.
- **Topology**: stores the connectivity and the mesh elements of the object.
- **MechanicalObject**: this is the main component storing all state vectors of an object and is templated on the degrees of freedom (DOFs) types.
- **ForceField**: all components inheriting from `BaseForceField` are adding either internal or external forces to the global system. For example, the components implementing the FEM for solid mechanics are internal force fields.

During the simulation, a series of algorithmic operations are performed independently from the graph structure and allow to compute mappings, propagate the simulation context, accumulate the forcefields, etc.. In SOFA, visitors are actions that are propagated to the graph, either top-down or bottom-up and that allow to perform these operations. For instance, the `SolveVisitor` is the action triggering the resolution of the system associated to a linear solver. Generally, all the components necessary to describe the cardiac scene are available in the `SofaCardiacModel` plugin.

4.2.2 Implementation's strategy

Various modules are required for the modelling of the heart's mechanical activity and are described in this section. Globally, the heart can be decomposed into four distinct modules, that, thanks to the modular approach offered by SOFA, can contribute independently to building the global system matrix and right hand side (RHS) vector:

1. the passive part corresponds to the work of the internal forces (section 4.2.3);
2. the active part is inherent to the modelling of contractile tissue, it refers to the models of force generation along the fiber directions and takes as input the electrophysiological activity described in the previous chapter (section 4.2.4);
3. the haemodynamic boundary condition, which includes the atria and aorta pressures, controls the valves system and thus the phases of the cardiac cycle (section 4.2.5);
4. other boundary conditions such as pericardium or other structures that hold the biventricular geometry in space (section 4.2.7).

The cardiac mechanical model developed in this chapter is based on the Bestel-Clement-Sorine (BCS) [Bestel et al., 2001] model, further improved by [Chapelle et al., 2012]. Its foundation relies on a multi scale physiological description of the myocardial muscle function, see Fig. 4.2. It describes both the passive and active components.

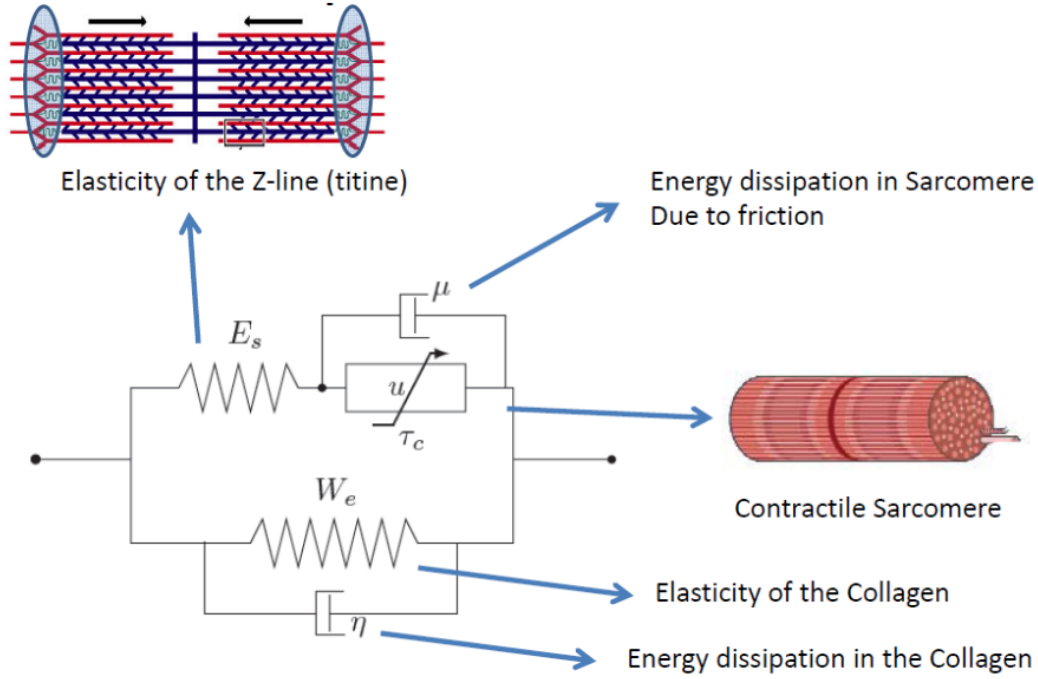


Fig. 4.2.: Rheological description of the electromechanical model as in [Bestel et al., 2001]. W_e is the strain energy of the extracellular matrix, associated with a dissipative term η . u is a control variable which is derived from the electrophysiological simulation and controls the contraction stress τ_c . μ accounts for the friction in the sarcomere while E_s represents the elasticity of the Z-discs (titin).

4.2.3 Biophysical material law

This section is dedicated to the modelling and implementation of the passive component of heart, that contributes to the internal forces that are generated upon deformation. The heart muscle is mainly composed of cardiomyocytes surrounded by an extracellular matrix, which presents a hyperelastic behavior. Note that the contribution of the extracellular fluid to the viscoelastic behavior of the myocardial tissue, investigated in [Yang et al., 1991], is neglected in this model.

Moreover, although several authors have used incompressibility constraints to model the myocardium, it has been reported that wall compressibility ranges from 15 to 20% in human hearts [Liu et al., 2021; Avazmohammadi et al., 2020].

Several hyperelastic material laws have been used to model the myocardium: orthotropic behavior taking into account both the fiber and sheet directions [Holzapfel et al., 2009;

Costa et al., 2001] ; isotropic such as in BCS model, or transversely isotropic such as the Guccione constitutive law [Guccione et al., 1995]. The latter is used in the cardiac benchmark proposed in [Land et al., 2015]. This benchmark allows to compare the simulation results of the cardiac model with those of other softwares and teams, for three problems with increasing complexity. It has been undertaken and allows to verify the implementation of the Guccione law and the tensor rotation framework (see Appendix B.3) in SOFA (not shown). Globally, adding the elasticity of the Z-discs, the passive behaviour of myocardial tissue in the BCS model is considered to be transversally isotropic.

The implementation of the material law is based on the work from [Brunet, 2020], namely the SofaCaribou plugin for SOFA. This plugin offers an interface for the implementation of the FEM, that is templated on the elements type. Linear and quadratic finite elements are supported on triangular, tetrahedral and hexahedral elements. Thanks to this implementation, only the SPK tensor and its derivative, the rank-4 elasticity tensor, are required to define the material law. The transformations of the state vectors from the deformed configuration to the undeformed one and to the isoparametric elements is already implemented, as well as the accumulation of these terms in the system matrix, depending on the topology.

Appendix A describes the derivation of a few hyperelastic material laws. Some laws are also implemented in the core of SOFA, their derivation usually comes from automatic differentiation tools. A first attempt at using the FEniCS [Scroggs et al., 2022] powerful automatic differentiation tools within SOFA has been proposed in [Mazier et al., 2022], using the Unified Form Language [Alnæs et al., 2014], a language for weak formulations of partial differential equations. Although promising, the link between SOFA and FEniCS is ambitious and some coding is still required to implement the material laws. Appendix A.2 presents an attempt at using the open source python project SymPy [Meurer et al., 2017] for the automatic differentiation of hyperelastic material laws, leading to the generation of a shared C++ library, then available as a SOFA dependency.

Finally, the results presented in this manuscript have been simulated using the polynomial Mooney-Rivlin material law because it offers a comparison with the previous work of [Marchesseau, 2013]. Fig. 4.12b shows a comparison on pressure and volume curves for different values of the material parameter c_1 . However, several laws have been implemented and calibrated on our mechanical model. The exponential laws such as Guccione or Costa laws exhibit an increased stiffness in systole as compared to polynomial laws, which helps in obtaining realistic mesh deformations.

Local basis for fibers anisotropy

Since several material laws are expressed in the local basis defined by the fiber directions, it is necessary to define a rotation tensor can be used to change the computational basis, see Appendix B.3. For example, $\Lambda = [\mathbf{f}_0, \mathbf{s}_0, \mathbf{n}_0]$ is the orthogonal rotation matrix that expresses the fiber, sheet and normal directions in the orthonormal basis of $\mathbb{E}^3 = \{\mathbf{e}_i\}$.

4.2.4 Active contraction

The second part of the BCS model aims at modelling the complex contraction phenomena that occurs after the electrical depolarisation: the muscle cells release ions, leading to sarcomere shortening. The contraction of the sarcomere can be derived, at the molecular scale, from the Hodgkin–Huxley filament model [Hodgkin et al., 1952]. At the macroscopic scale, the active contraction follows the law proposed by [Chapelle et al., 2012], where the active stress τ_c and stiffness k_c are controlled by an electrical input u , leading to a system of Ordinary Differential Equations (ODE):

$$\begin{cases} \dot{k}_c = -(|u| + \alpha |\dot{e}_c|) k_c + n_0 k_0 |u|_+ \\ \dot{\tau}_c = -(|u| + \alpha |\dot{e}_c|) \tau_c + \dot{e}_c k_c + n_0 \sigma_0 |u|_+ \end{cases} \quad (4.30)$$

where α is a constant related to the cross-bridge unbinding due to the deformation rate, k_0 and σ_0 are respectively the maximum stiffness and contraction. e_c corresponds to the fiber strain.

To this stress τ_c , we add one contribution to account for the fact that the binding-unbinding phenomenon dissipates energy by friction and viscous effects, which gives

$$\sigma_c = \tau_c + \mu \dot{e}_c \quad (4.31)$$

The reduction factor n_0 allows to take into account the Starling effect according to which the maximum active stress depends on the strain e_c . In this case, n_0 can be defined as a function of the history of e_c , e.g. to represent the effect of the previous maximum stretch

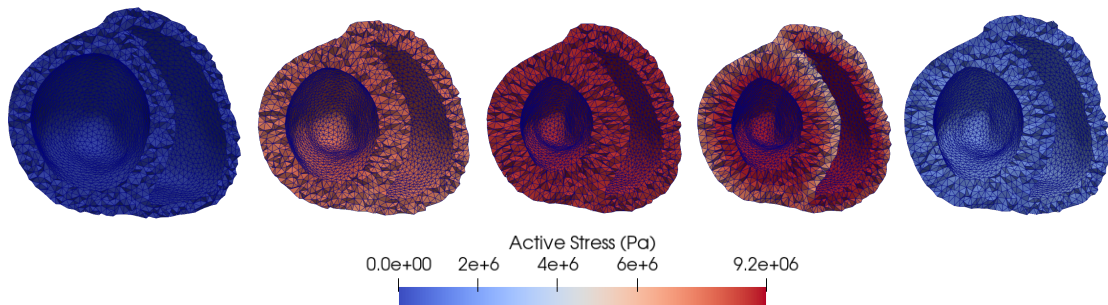


Fig. 4.3.: Mesh deformation and active stress over a cardiac cycle.

of the sarcomeres (preload) or some long-term effects spanning over several cardiac cycles.

The rheological model presented in Fig. 4.2, and in particular the two elastic components in series, gives an expression for the active stress that depends only on strain:

$$\sigma_c = \tau_c + \mu \dot{e}_c = E_s \frac{e_{1D} - e_c}{(1 + 2e_c)^3} (1 + 2e_{1D}) \quad (4.32)$$

From the second equality we extract e_c^{n+1} and we can use the first equality as the final form for the stress. This formulation will be added in `addForce` method of the contractile component.

SOFA implementation

The ODE system (eq. 4.30) is solved in a separate node in the scene graph. The `ContractionForce` manages the resolution of this system based on the components present in the graph (`BackwardEuler`, `CGSolver`, ...). For each `addForce` in the `ContractionForce`, the `SolveVisitor` visitor is triggered which builds the global system matrix (for all integration points), and solves it. The two-element vector at each integration point is then retrieved in `ContractionForce`.

To disable all visitor traversals in this node that could trigger the resolution of the ODE, it is set to a sleeping mode. Indeed, this resolution need to be done when the fiber strain has been computed in the `ContractionForce` component. The latter implements a `SingleLink` to the coupling node and is the only entry point to the resolution of the ODE (through the `SolveVisitor`).

Alternative contractile stress formulation

The exponential profile for the active stress, as given by the BCS model, leads to a rapid early contraction of the sarcomeres, and then a plateau where the fibers have reached their contractile limit, but cannot relax yet because their transmembrane potential is still in the depolarized state. At the beginning of the contraction, during the isovolumetric contraction phase, the pulmonary and aortic valves are closed ; as the ventricles contract without diminution of their volume, the pressure rapidly increases, until the pressure in the ventricles reaches that in the arteries, thus opening the valves. When the ejection starts, the blood flow in the arteries suddenly increases, the ventricular pressure drops and reaches a plateau for the remaining time of the APD. This is visible in Fig. 4.12c, for $a = 1$, corresponding to an almost exponential contraction stress as in the BCS model. However, in this case, the shape of the ventricular pressure is not realistic and should be more symmetric. The resulting LPEI (51ms) is also shorter than the expected physiological value of 80-90ms found in healthy patients.

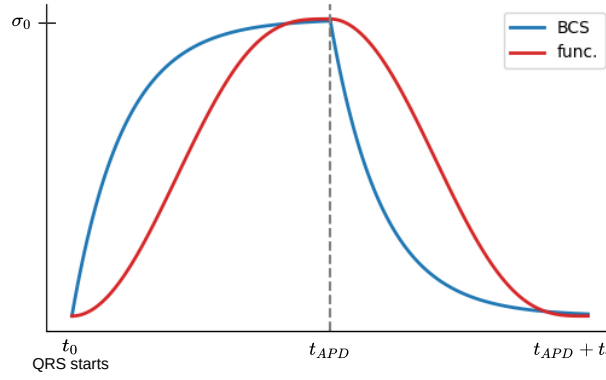


Fig. 4.4.: Comparison of the active stress σ_c obtained with the BCS model and the Kumaraswamy cumulative distributions (referred as ‘func.’). t_{APD} corresponds to 90% of the duration of the action potential while t_r represents the repolarization time.

These observations led to the redefinition of the active stress formulation, using two Kumaraswamy cumulative distributions, one for the contraction and a second one accounting for the active relaxation. A comparison of the active stress over time is presented in Fig. 4.4. It is visible that with this function, the contraction of the sarcomeres increases much slower than compared to the BCS solution.

The Kumaraswamy cumulative distribution transforms an input $x \in [0, 1]$ into a value $y \in [0, 1]$ and is parameterized with two coefficients, controlling the shape of the curve for both ends of the definition interval. Here, the coefficients a and b are associated with the contraction ($t < t_{APD}$) while g and h control the relaxation ($t > t_{APD}$), with t_{APD} the duration of the depolarization state of the cardiac cells. Most realistic ventricular pressure profiles were found using $a = 2$, $b = 1.5$, $g = 2$, $h = 3$. The influence of these parameters is presented in Fig. 4.12. This active stress model, although not incorporating physiological elements such as the Frank-Starling mechanism, is in good concordance with the active stress measures reported in [Liu et al., 2021], where the authors fit their cardiac model simulation results on ovine observations. Moreover, it offers a convenient method to benchmark different evolutions of the active stress and their influence on the model’s behavior.

4.2.5 Hemodynamics

Modelling the four cardiac phases

In the mechanical model, the cardiac phases are controlled by the different pressures in the heart chambers and relate the current state of both ventricles, which are treated similarly but independently:

1. Filling phase: the ventricular pressure P_v is below the atrial pressure P_{at} , the atrial valve (either mitral or tricuspid) is open and the ventricle fills with blood. At the end of this phase, the atrial contraction accounts for 20 to 30% of the filling [Kurapati et al., 2022] ;
2. Isovolumetric contraction phase: when the first cells start to contract, P_v exceeds P_{at} , leading to the closing of the atrial valve. Since all valves are closed, the ventricular volume remains constant during this phase, while P_v increases ;
3. Ejection phase: when P_v overtakes the aortic pressure P_{ar} , the gradient of pressure causes the (aortic or pulmonary) valve to open, leading to the ejection of blood through the arteries ;
4. Isovolumetric relaxation phase: when $P_v \leq P_{ar}$, all valves are closed and P_v drops rapidly due to the relaxation of the sarcomeres.

The following model is used to model the cardiac phases presented above:

$$Q = \begin{cases} K_{at} (P_v - P_{at}) - K_{var} (P_v - P_{ar}) & \text{for } P_v \leq P_{at} \\ -K_{var} (P_v - P_{ar}) - K_{vat} (P_v - P_{at}) & \text{for } P_{at} < P_v \leq P_{ar} \\ K_{ar} (P_v - P_{ar}) - K_{vat} (P_v - P_{at}) & \text{for } P_v > P_{ar} \end{cases} \quad (4.33)$$

where the ventricular flow Q is negative when blood enters the ventricle ($Q < 0$ during the filling phase, the blood flow is directed from atrium to ventricle). It is positive when blood leaves the ventricle ($Q > 0$ during the ejection phase, the blood flow is directed from ventricle to artery).

K_{ar} and K_{at} are coefficients controlling the resistance of the respecting valves to the flow. The smaller these coefficients are, the higher the pressure difference required to reach the same flow Q . K_{vat} and K_{var} are coefficients controlling valve regurgitation between the ventricle and the atrium or the artery, respectively. For instance, $Q = 0$ during the isovolumetric phases ($P_{at} < P_v \leq P_{ar}$) if $K_{vat} = K_{var} = 0$.

The system 4.33 constitutes a relation that has to be verified at each time step of the simulation, in particular at time $t + \Delta t$. It gives a relation between $Q^{t+\Delta t}$, $P_v^{t+\Delta t}$, $P_{ar}^{t+\Delta t}$ and $P_{at}^{t+\Delta t}$ which is seen as a constraint on the model and developed in section 4.2.6. The atrial pressure $P_{at}^{t+\Delta t}$ is analytically computed using sigmoidal functions, which also models the contraction of the atria. To compute $P_{ar}^{t+\Delta t}$, the model is a bit more complex as it relates the ejection flow, the compliance of the arteries and the resistance of the cardiovascular system. It is based on the Windkessel model.

Windkessel models

Although the heart ejects blood in a pulsatile way, the blood circulation in the cardiovascular system is relatively constant. The physiologist Otto Frank suggested that the pressure variations are related to the elasticity of the arteries [Kuhtz-Buschbeck et al., 2018]. Several models of the arterial flow have been proposed, including very detailed 3D (distributed) models, but we instead rely here on a so-called lumped 0D model. [Westerhof et al., 2009] proposes a good review on the Windkessel (WK) models.

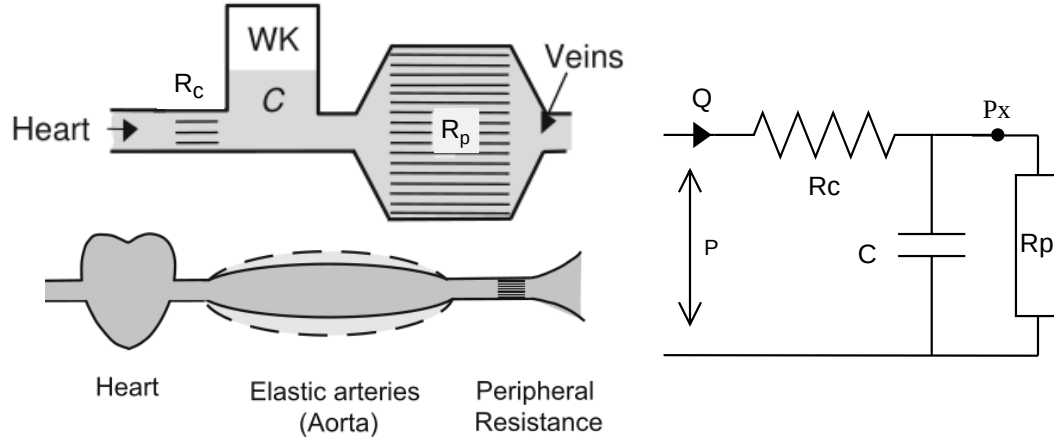


Fig. 4.5.: Concept of the Windkessel effect to model elastic reservoir and its electrical analogy. Thanks to the compliance of the large arteries and the peripheral resistance of the veins (modelled as electrical capacitance (C) and resistance (R_p)), the peripheral flow is rather constant. R_c is the aortic characteristic impedance [Westerhof et al., 2009].

While the 2-element WK model offers a good description of the exponential decay of the arterial pressure during diastole, it fails for systole. The 3-element WK includes an additional resistive element, leading to the following relation between aortic flow Q and pressure P :

$$R_p C \dot{P} = (R_p + R_c) Q + R_p C R_c \dot{Q} - P \quad (4.34)$$

4.2.6 Constraint-based implementation of the valves system

Lagrangian constraints

At any time of the simulation, the relation between the cavities' pressure and the blood circulation is given by the hemodynamic model (eq. 4.33). To ensure that this relation is verified at all times, it is added to the dynamical system (eq. 4.24) and solved as a Lagrangian constraint:

$$\mathbf{A} \Delta \mathbf{v} = \mathbf{b} + \mathbf{H}^T \boldsymbol{\lambda}$$

where \mathbf{H} holds the constraint directions and $\boldsymbol{\lambda}$ is a vector containing the Lagrangian multipliers, corresponding to the correction of pressure to apply along \mathbf{H} to guarantee

that the constraints are respected. Globally, $\mathbf{H}^T \lambda$ is the vector of constraint forces contribution.

Since our geometry has two ventricles, there are two constraints in the model and $\lambda \in \mathbb{R}^2$. \mathbf{H} corresponds to the volume derivative, such that $\mathbf{H}\mathbf{v}$ measures the flow \mathbf{Q} . The computation of the volume derivative for an open surface mesh is developed in Appendix B.2.

The joint resolution of dynamics and constraints is a classical problem in multi-body simulations and is therefore already implemented within SOFA. It has for example been used to model the interactions between medical devices and biological tissue in [Duriez, 2013], or in the simulation of soft robots [Coevoet et al., 2017; Bernardin et al., 2019]. The resolution process involves splitting the time step into two stages:

1. **Free motion:** a first deformed configuration is computed while considering that no constraint is imposed on the system, (i.e., $\lambda = 0$). This resolution leads to the definition of the free velocity $\mathbf{dv}^{\text{free}} = \mathbf{A}^{-1}\mathbf{b}$. After the free motion, we can compute the constraint violation $\delta^{\text{free}} = \Delta t \cdot \mathbf{H}\mathbf{v}^{\text{free}}$.
2. **Constraint correction:** the second stage of the time step consists in computing the correction due to the constraints ($\mathbf{b} = 0$), leading to $\mathbf{dv}^{\text{corr}} = \Delta t \mathbf{A}^{-1} \mathbf{H}^T \lambda$, with λ the unknown correction.

The resolution of the constraints is not performed in the motion space but is rather projected in the constraint space using the Schur complement. The constraint law is given by:

$$\delta = \underbrace{\Delta t^2 [\mathbf{H}\mathbf{A}^{-1}\mathbf{H}^T]}_{\mathbf{W}} \lambda + \delta^{\text{free}} - \delta^{\text{target}} \quad (4.35)$$

where $\mathbf{W} \in \mathbb{R}$ represents the coupling between the endocardial surface and the ventricular pressure.

$\delta^{\text{target}} = \mathbf{Q}^{t+\Delta t}$ is given by the hemodynamical model and depends on the value at the next time step of the ventricular pressure $\mathbf{P}_v^{t+\Delta t} = \lambda$, the atrial pressure $\mathbf{P}_{at}^{t+\Delta t}$ and the aortic pressure $\mathbf{P}_{ar}^{t+\Delta t}$. $\mathbf{P}_{at}^{t+\Delta t}$ is easily obtained since it follows an explicit formulation, but $\mathbf{P}_{ar}^{t+\Delta t}$ is derived from the Windkessel model and cannot be found directly. Indeed, its resolution depends on the flow $\mathbf{Q}^{t+\Delta t}$, variable that is already used in the hemodynamical model. We need to find an expression for δ^{target} that does not involve $\mathbf{Q}^{t+\Delta t}$, as it is the case with Windkessel model. To do so, the 3-element Windkessel ODE equation is manually solved with the Crank–Nicolson method, an implicit finite difference method that is unconditionally stable. The development of this resolution is presented in Appendix B.1. It leads to an discretized expression of the hemodynamical model that do not rely on $\mathbf{P}_{ar}^{t+\Delta t}$.

Once the constraint law (eq. 4.35) is defined, it only remains to compute the value of the Lagrangian multiplier λ . This is done by minimizing the constraint violation δ in the constraint space, and is solved using the Gauss-Seidel algorithm.

Implementation of the constraint in SOFA

The `FreeMotionAnimationLoop` implements the two steps constraints resolution and is therefore required, as well as a `GenericConstraintSolver` which handles the constraints resolution. A linear solver is required to compute \mathbf{A}^{-1} , it can be the same solver as the one used for the free motion step or any direct or iterative solver. In case of preconditioning, it can be judicious to use the same solver for the preconditioner and the constraints.

Additionally, a constraint law component implements the penalization term for the Gauss-Seidel minimization problem. The solution of this problem yields the value of the Lagrangian multiplier λ , the ventricular pressure to apply at the next time step on the endocardium, so that the hemodynamical model is verified at the beginning of the next time step.

4.2.7 Boundary conditions

Several boundary conditions are included in the mechanical model to restrain the displacement and deformation of the heart. First, to restrain the movement of the valves, a spring force is added to all nodes surrounding the valves, so that these nodes are attached to their initial position but can still have a displacement. The value of 9kPa for the spring stiffness associated to these nodes has been used and seems to be a good trade off between the mesh deformation and the numerical stability by keeping the mesh attached in space. Optionally, the same force field can be applied to the apex, a stiffness of 3kPa has been used. While these force fields do impact the mesh deformation, they do not degrade the pressure volume results.

Secondly, the pericardium is included as a surface surrounding the heart and helps in restraining the displacement of the mesh and the inflation of the ventricles. In SOFA, the pericardium and the epicardial surfaces are implemented as collision models, so that during the simulation, a force is generated for any two nodes intersecting with each other, preventing the penetration of these surfaces. The pericardial surface is fixed in space and is generated at 3mm from the epicardium. Collision is detected when a point on the epicardium approaches the pericardium by less than 1mm. Note that [Pfaller et al., 2018] emphasizes the importance of the stiffness of the pericardium in the mesh displacement but the deformation of the pericardium has not been studied here. Moreover, including the resolution of pericardial contacts in the simulation considerably slows down the computation, and is therefore not used in the simulation results shown in this study.

4.2.8 Conclusion

The implementation of this mechanical model in SOFA yields to a complex system but thanks to SOFA's modularity, components are clearly identified and can be benchmarked independently. The global SOFA scene graph describing the cardiac simulation is presented in Fig. 4.6. It shows the different nodes and their components, as well as the different mappings that connect the various objects of the simulation.

On the left, the root node contains all the general-purpose components related to visualization, collision detection, and the `FreeMotionAnimationLoop` that is required both for contacts and the hemodynamical constraint presented in section 4.2.6.

The first child node is called `MecaNode` and represents the biventricular geometry. It is composed of components related to the tetrahedral topology, the solvers for the system resolution, and all components relevant for the simulation of cardiac mechanics: the passive hyperelastic material, the active contraction, the boundary conditions and the constraints solver. On the same level as this node is the `Coupling` node. It implements the active ODE, which is solved using an implicit method and a dedicated solver.

The third level of nodes is composed of all objects that are dependent on the deformation of the main tetrahedral mesh, such as the epicardial collision mesh, the visualization mesh, and the endocardial surfaces. During the simulation, the deformation of the mesh is mapped to these child surfaces and any force applied onto them is mapped back to the `MecaNode` to be accumulated in the dynamical system. The two ventricles are implemented similarly but their parameters and initial conditions may be different. Generally, a ventricle implements all the algorithms necessary to compute the current phase based on pressure values, and to apply the hemodynamic constraint. The next section is dedicated to the presentation of the SOFA simulation results generated with this scene graph.

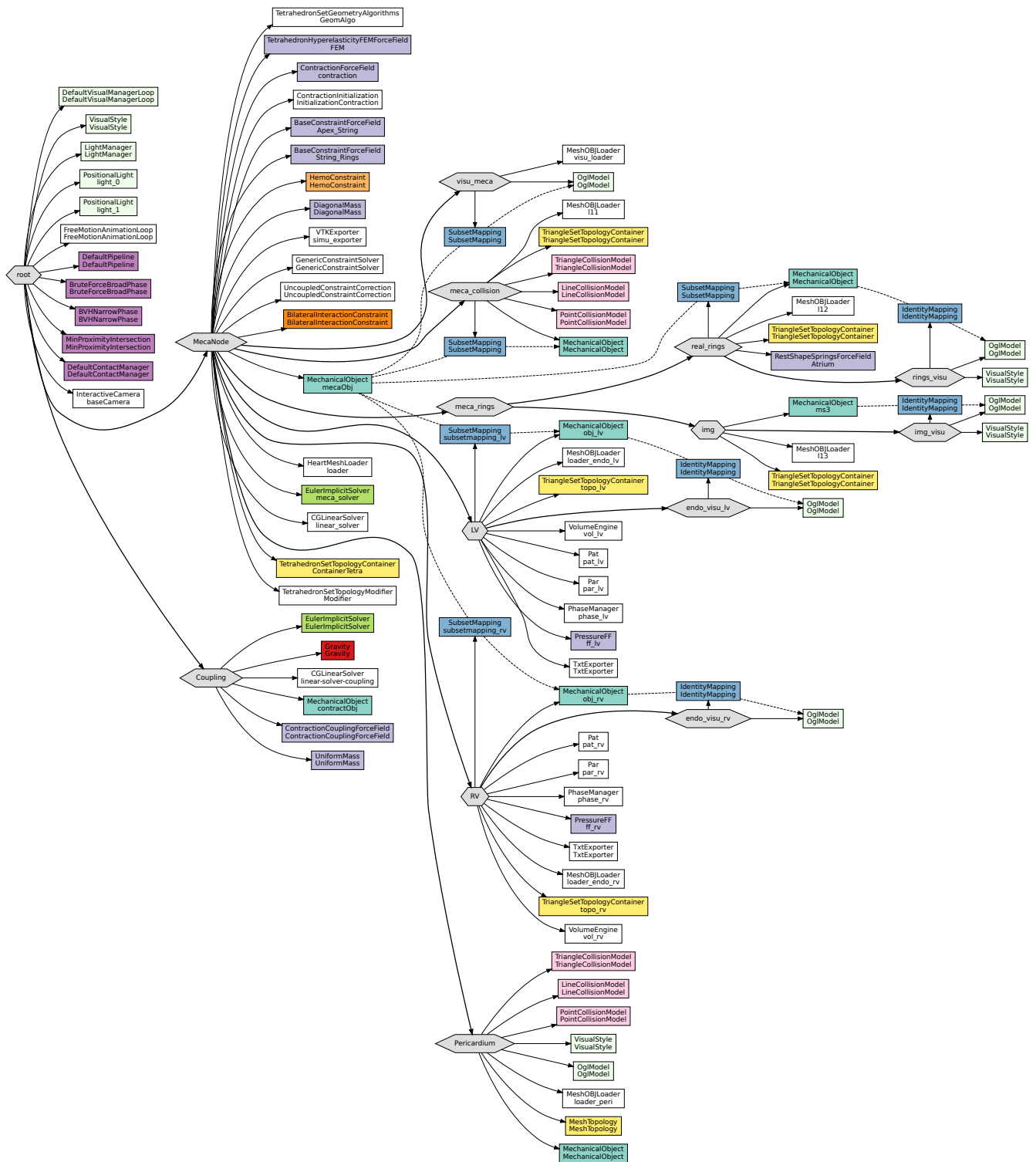


Fig. 4.6.: Complete SOFA scene graph describing the simulation of the heart. Nodes are represented by the hexagons while SOFA components are the rectangular boxes ; mappings are represented by dashed lines. The coupling node, `Coupling`, is used to solve the coupled ODE system and find the contractile stress. On the same level, `MecaNode` represents the object 'heart', with its tetrahedral topology. Its components implement the active and passive parts, as well as the resolution of the constraints (both the contacts and the volume constraint). Its `MechanicalObject` is mapped to child nodes: `lv` and `rv` are nodes representing both ventricles, `Pericardium` and `meca_collision` implement the contacts algorithms and `meca_rings` the boundary conditions. For each ventricle, a series of component load the triangular surface, compute the volumes, pressures and phase, and add their contribution to the constraints system. Component data and links are not displayed on this graph.

4.3 Results

4.3.1 Normal heart

Simulation results for both ventricles corresponding to the healthy electrophysiological case (Fig. 3.8) is presented in Fig. 4.7. The mechanical simulation starts at $t = 0$, time at which the first point on the activation map is depolarized. After a small electromechanical delay (about 10ms [Heikhmakhtiar et al., 2017]), fibers start to contract and the ventricular pressure to increase, reaching 120mmHg at its maximum. The duration of the isovolumetric contraction phase is 100ms, and the isovolumetric relaxation phase lasts 40ms. The arterial pressure shows an exponential decay around 80mmHg, except during the ejection phase, where it increases alongside the ventricular pressure to reach 110mmHg. Note that the atrial pressure has been included in this simulation.

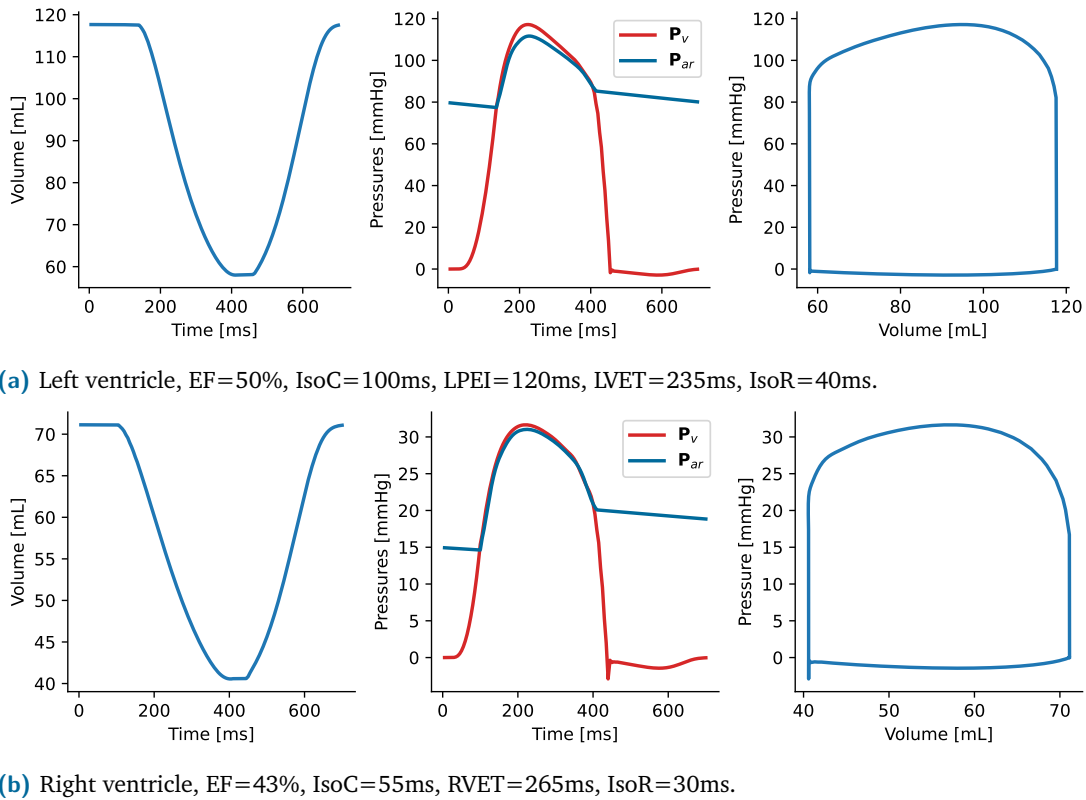


Fig. 4.7.: Volume and pressure curves resulting from the sinus rhythm simulation on healthy geometry. IVD=35ms, myocardial compression=7%.

In order to study the rotation during the contraction of the heart, several points have been selected on the endocardial and epicardial surfaces, as shown in Fig. 4.8. Three planes in the LV small axis are defined at the apex, mid and base of the BiV geometry. A ray tracing from the center of these planes gives the intersection with the mesh and the localization of the selected points. At the beginning of the simulation (i.e. in the rest position), we store the barycentric coordinates of these points with respect to the

underlying triangle or tetrahedral mesh. During the simulation, the deformation of the mesh is mapped to the points using the barycentric coordinates, so that the selected points move with the mesh.

At each simulation time step, these planes are recentered to their undeformed location, so that the center of each plane matches its original position. Then, the rotation of each point is determined by the angle formed between the rest and deformed configurations, with respect to the plane's center. The rotation of the mesh is visible on Fig. 4.8, where the selected points are grouped by localization: endocardium (red) and epicardium (blue).

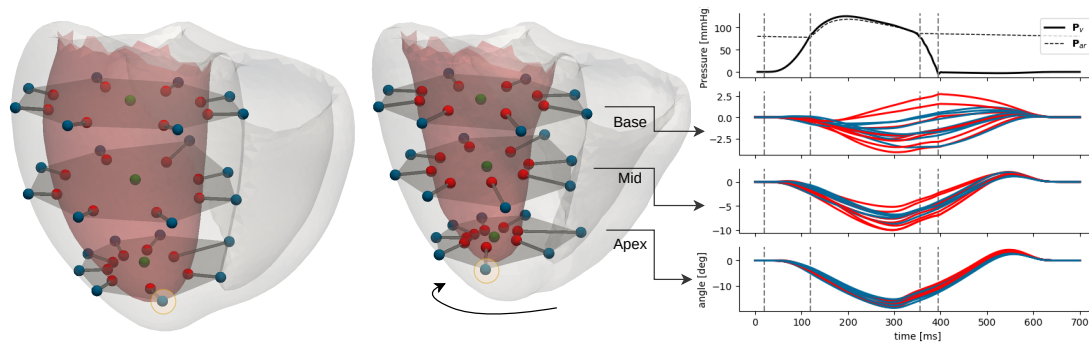


Fig. 4.8.: Mesh with selected points in end diastole (left) and end systole (center) and the rotation of the selected points at the apex, mid and base of the heart (right).

A rotation of -15° is present on the apex, and it ranges between -3 and 3° at the base.

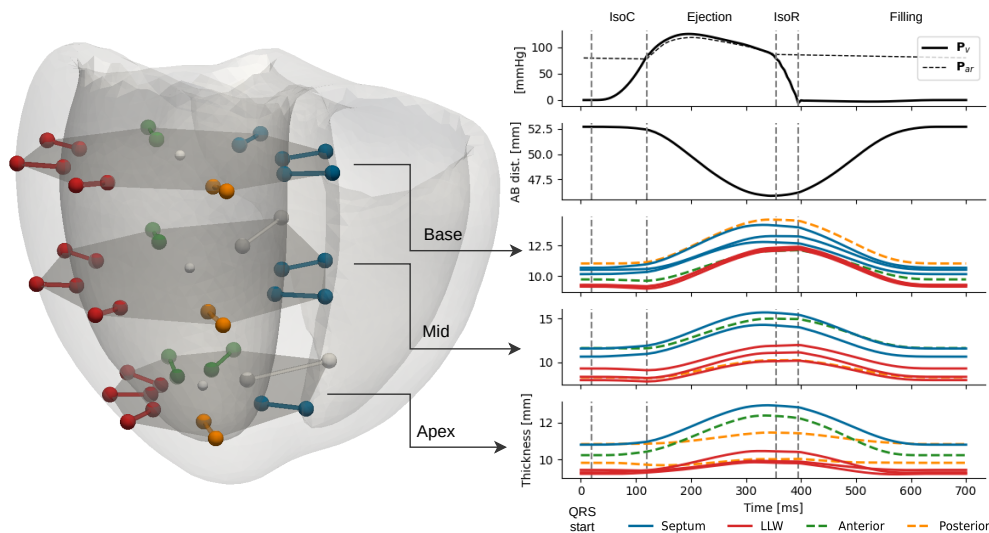


Fig. 4.9.: Evolution of the LV wall thickness and the apicobasal distance during the cardiac cycle.

Similarly, the thickness of the LV wall during the cardiac cycle is evaluated in Fig. 4.9. The thickness corresponds to the length of the transmural segments extracted with the ray tracing method, they are grouped by localization if the LV: LVFW (red), anterior wall (green), posterior wall (orange) and septum (blue).

4.3.2 DCM with LBBB

The results for the mechanical simulation of LBBB (corresponding to Fig. 3.15) is shown Fig. 4.10.

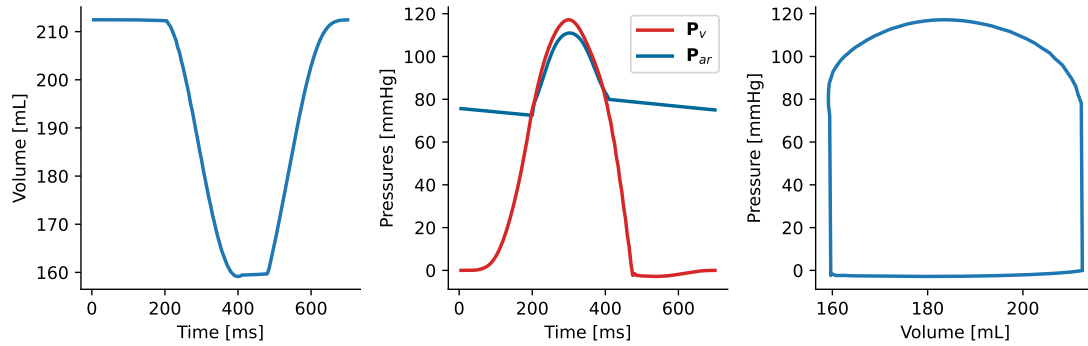


Fig. 4.10.: LV volume and pressure curves from the simulation of a pure LBBB on a DCM geometry. EF=25.1%, IsoC=185ms, LPEI=200ms, LVET=210ms, IsoR=65ms

For this simulation, the maximum fiber contractility has been calibrated so that the maximum ventricular pressure reached 120mmHg. These results show a prolonged isovolumetric contraction duration and an ejection fraction of 25%. A summary of the main observations is presented in Tab. 4.1.

4.3.3 Mechanical simulation of the CRT

In order to examine the effect of the CRT, a BiV pacing simulation is presented in Fig. 4.11. The spontaneous activation has been entirely deactivated (capture) so that the electrical activation only comes from the stimulation. As presented in section 3.6, the electrical signal first propagates within the myocardium before eventually reaching a node of the Purkinje network. No significant changes are observed as compared to the LBBB simulation without pacing. Again, Tab. 4.1 offers a summary of the main electromechanical indices.

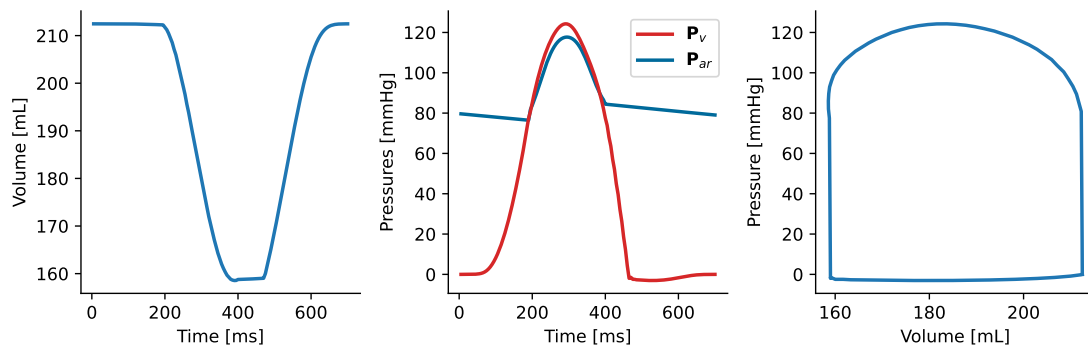


Fig. 4.11.: LV volume and pressure curves from the simulation on a DCM geometry, with a BiV stimulation. EF=25.4%, IsoC=170ms, LPEI=190ms, LVET=210ms, IsoR=65ms

Tab. 4.1 compares the simulation results for the three cases presented in this section: healthy scenario, LBBB and BiV stimulation. $\max\left(\frac{dP_v}{dt}\right)$ is an important index for the simulation since it provides a global measure of the contraction force. It is expected that the ventricular pressure increases more rapidly when all cardiac cells are contracting at the same time, while it is expected to be slower when different segments contract in a desynchronized way. The delay of the maximum contraction between the septum and LLW is given in the penultimate column. In the case of the LBBB simulation, the left lateral wall reaches its maximum contraction 40ms after the septum, while this delay is reduced to 5ms for the BiV pacing.

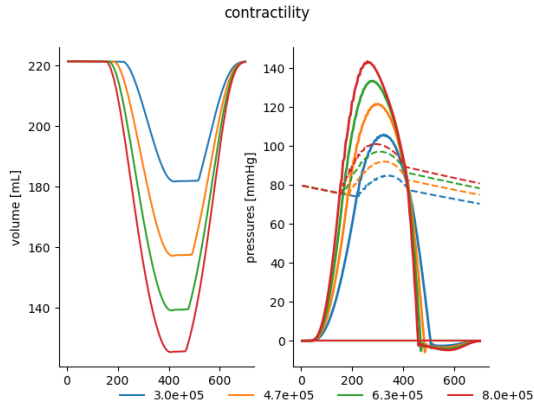
Scenario	Elec. results	Mechanical results	$\max\left(\frac{dP_v}{dt}\right)$ [mmHg/s]	QRSd [ms]	EF [%]	LPEI [ms]	Sept-LLW [ms]	IsoC [ms]
Healthy	Fig. 3.8	Fig. 4.7a	1522	77	51	135	10	100
LBBB	Fig. 3.15	Fig. 4.10	1069 (-30%)	172	25.1	200	40	185
BiV	Fig. 3.20	Fig. 4.11	1081 (+1.1%)	99	25.4	190	5	170

Tab. 4.1.: Evolution of the left ventricular pressure derivative and a few electromechanical indices of interest in CRT for different simulation scenarios.

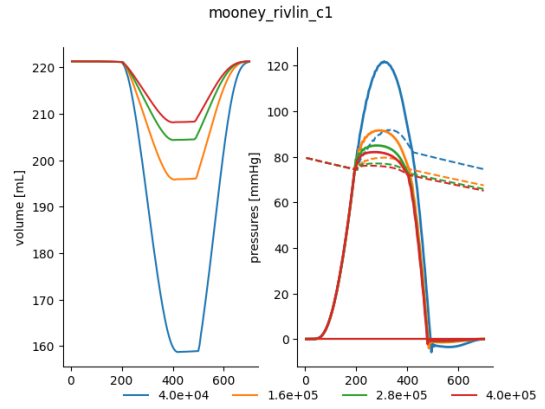
With these results, the benefit of the CRT is limited with an increase of $\max\left(\frac{dP_v}{dt}\right)$ of about 1%. However, it has been observed that different electromechanical coupling profiles yield values of this index up to 8%. It is possible that the active stress function plays a major role in the response to CRT but these properties have not been sufficiently explored to draw conclusions yet.

4.3.4 Sensitivity analysis

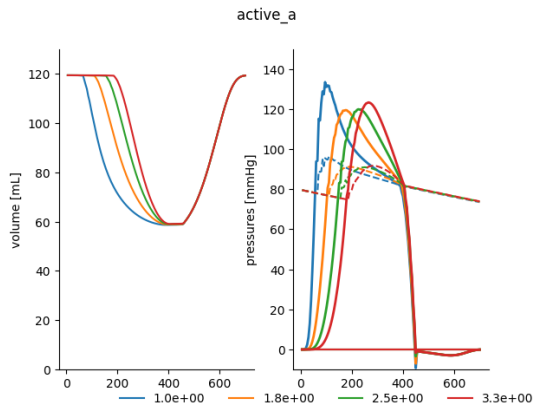
As for the electrophysiological model, a study of the influence of a few relevant parameters on the mechanical model is presented in Fig. 4.12. The passive component is represented by the material parameter c_1 of the Mooney-Rivlin constitutive law. Additionally, all the five parameters of the active contraction model based on the Kumaraswamy cumulative distribution are presented, including the maximum contractile force developed by the sarcomeres, the two parameters controlling the contraction, a and b , and the two controlling the relaxation, g and h , see section 4.2.4.



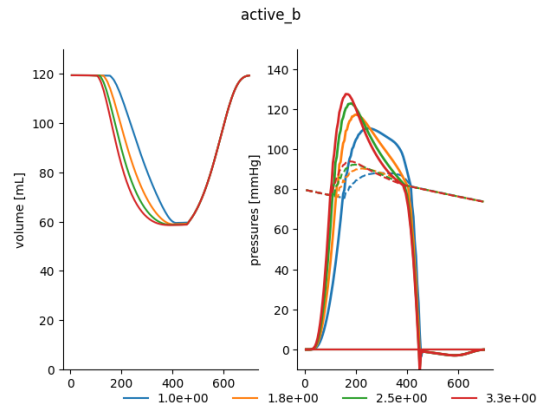
(a) Maximum contractility σ_0 [Pa]



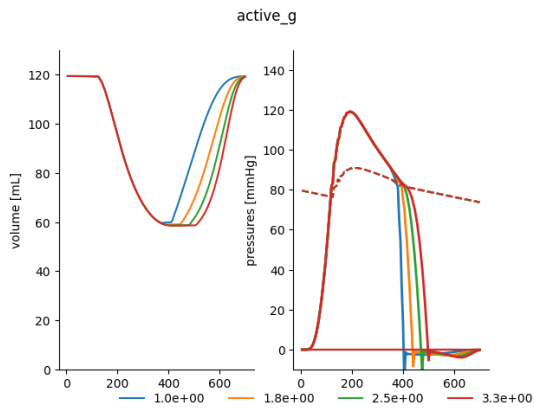
(b) Mooney-Rivlin stiffness parameter c_1 [Pa]



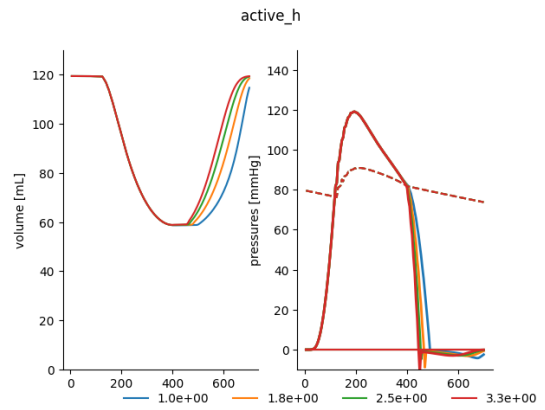
(c) Active contraction coefficient a



(d) Active contraction coefficient b



(e) Active relaxation coefficient g



(f) Active relaxation coefficient h

Fig. 4.12.: Results of the sensitivity analysis on the mechanical model. On the pressure plots, the dashed corresponds to the atrial pressure while the continuous lines represent the ventricular pressure.

Tab. 4.2 presents the correlation between the mechanical parameters and the indices computed on each model's output.

Tab. 4.2.: Results of the sensitivity analysis on the mechanical indices. EF: Ejection Fraction, LVET: Left Ventricle Ejection Time, LPEI: Left ventricle Pre-Ejection Interval, SD: Systole Duration, Iso.CT: Isovolumetric Contraction Time, Iso.RT: Isovolumetric Relaxation Time, IVD: InterVentricular Delay. R_p : arterial peripheral resistance, Z_c : characteristic impedance of the artery, C : total arterial compliance, K_{rs} : relaxation rate, K_{atp} : contraction rate, K : bulk modulus, σ : contractility, α : maximum fibres angle. Green: p-value<0.001, Yellow: p-value<0.01, Orange: p-value<0.1, Red: p-value>0.1.

	EF	LVET	LPEI	LPEI/LVET	SD	Iso.CT	Iso.RT	IVD
R_p	-0.42222	0.23128	0.02273	-0.11963	0.18141	0.02645	0.64766	-0.00766
Z_c	-0.03788	0.21657	0.00576	-0.10319	0.14087	0.00125	0.05784	-0.00157
LL	0.24441	0.58033	-0.00847	-0.36903	0.34962	-0.01144	-0.349	-0.00948
τ	0.32062	-0.29936	0.10974	0.304	-0.19011	0.10257	-0.48444	0.18499
K_{rs}	-0.02571	-0.03178	0.01345	0.01319	-0.02072	0.00205	-0.01778	0.02944
K_{atp}	0.07897	-0.02247	-0.4114	-0.39651	-0.25082	-0.41028	-0.00922	-0.30771
K	-0.02688	0.00409	0.03267	0.02106	0.00687	0.03839	0.02471	0.06666
σ	0.72809	-0.25892	-0.81655	-0.64763	-0.62813	-0.81896	-0.32104	-0.79371
α	-0.02548	-0.03125	0.02816	0.00826	-0.00697	0.01788	-0.00138	0.096

4.3.5 Discussion

The mechanical model presented in this section generates realistic simulations on healthy and pathological simulations. It is clear that the LBBB deteriorates the mechanical simulation results, both in terms of mesh deformation and on the pressure/volume curves. However, the BiV pacing simulation should have had a greater impact on the electromechanical indices, see Tab. 4.1. The gain on the pressure derivative is only 1% while [Dekker et al., 2004] and [Liu et al., 2002] reported a 15-20% increase of this index on stimulated hearts.

The sensitivity analysis performed with a healthy scenario helps in understanding the direct influence of the parameters on the model's behavior. First, the maximum contractility and the stiffness of the material both affect the maximum ventricular pressure and the stroke volume but are antagonistic and work against each other. As it is also visible in Tab. 4.2, σ_0 is negatively correlated with the duration of both isovolumetric phases, reflecting the fact that stronger contraction and relaxation lead to faster mesh deformations and greater inertia.

Similarly, the coefficient a in Fig. 4.12c (equivalent to K_{atp} in Tab. 4.2) is negatively correlated with the isovolumetric contraction duration. It is visible on the volume plot that the aortic valve opens later when the active stress rises slower, increasing the duration of the isovolumetric contraction phase. The parameter b controls the second half of the active stress function and has a major impact on the shape of the pressure

during the ejection. With a small b , the fibers will take more time to reach a high value of contraction, as it is visible on the volume. Inversely, when the fibers reach their maximum contraction quickly, the pressure exhibits a non-symmetrical shape, probably due to the inertia accumulated during the isovolumetric phase. The same remarks can be made on the relaxation phase regarding the coefficients g and h . With g (equivalent to K_{rs} in Tab. 4.2) small, the active stress decreases exponentially, thus leading to a rapid depressurization of the ventricles and a short isovolumetric relaxation phase.

Regarding the Windkessel parameters, it is clear from Tab. 4.2 that they are not correlated with non-ejection indexes such as LPEI or the isovolumetric contraction time. Since they control the shape of the arterial and ventricular pressures during the ejection, a strong correlation on the ejection time and ejection fraction was expected. The closing time of the aortic and pulmonary valves is also depending on those pressures, thus the correlation observed on the isovolumetric relaxation time. However, it can be observed that the fibres extremum angle do not seem to impact these model outputs.

The rotation patterns observed in Fig. 4.8 are in good accordance with [Taber et al., 1996; Sengupta et al., 2008] where the apex rotation angle lie between -20° and -10° . It has been reported in [Jadczyk et al., 2021] that the base shows an anti-clockwise rotation but it is very small on the graph, maximum 3° . The reduced rotation of the base can be explained by the two conditions applied near the valves: the spring force field (boundary conditions) restrain the motion and, because of the presence of fibrous tissue near the base, the conductivity and contractility of the cardiac cells are reduced in this area. The thickening of the myocardial wall is also within the reported range.

4.3.6 Computation time and influence of the discretization

This section presents several simulation results for a healthy scenario but where the mesh has been homogeneously discretized with different value of the mean edge length, ranging from 1mm to 6mm. The level of refinement of the mesh is an important

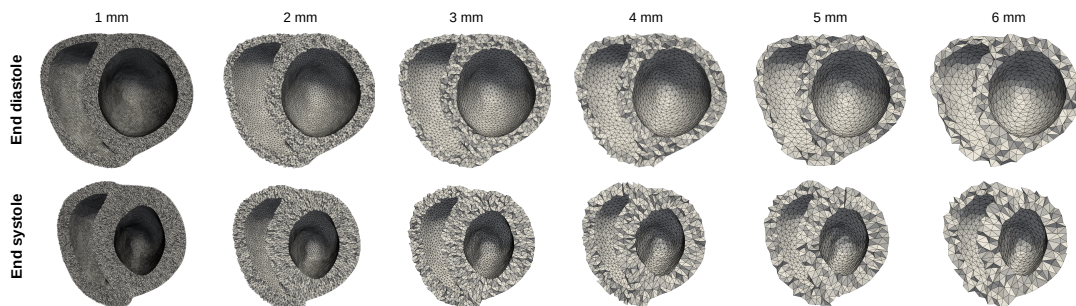


Fig. 4.13.: Biventricular geometry for different level of discretization, varying the mean edge length between one and six millimeters.

parameter when doing numerical simulations since coarse meshes can yield inaccurate results. Generally, the model solution will converge as the mesh density increases, but the computation time increases as a consequence. Tab. 4.3 presents the computation times for the selected meshes, ranging from a minute for the coarser mesh to sixteen hours for the finer one. Note that dilated geometries take a little more time to compute because there are more elements (about 25% more tetrahedra). Fig. 4.14 offers an overview of the meshes at the end diastole and end systole.

Mean edge length [mm]	Nb points	Nb tetrahedra	Computation time [min]
1	347k	2M	960 (16h)
2	58k	295k	50
3	18k	86k	20
4	8500	39k	7
5	5000	21k	2.5
6	3000	13k	1.3

Tab. 4.3.: Computation time for various mesh discretization on a healthy geometry.

Fig. 4.14 presents the influence of the mesh discretization on the rotation, volume and pressure results. On this healthy simulation, even for the coarser mesh the simulation is stable. A small difference can however be observed on the rotation values, up to 4°

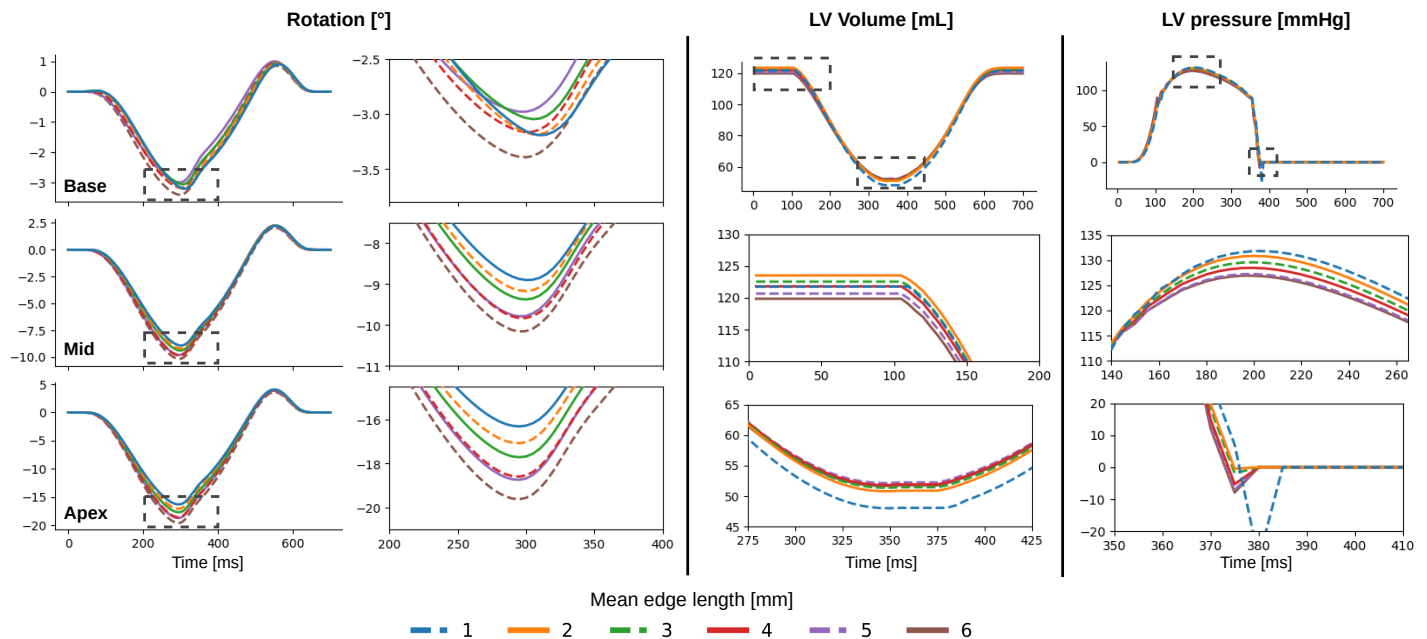


Fig. 4.14.: Effect of the mesh discretization on rotation, volume and ventricular pressure.

between the coarser and finer mesh, at the apex. Interestingly, it is the coarser mesh that exhibits the most rotation. It is counterintuitive since more tetrahedra in the cross wall section should capture more fiber directions and increase the leverage between endocardium and epicardium.

Finally, Fig. 4.15 presents the main operations that are executed during one time step of the simulation. Because we are using the free motion, the animation step is divided in two parts. The first stage consists in computing all forces applied on the heart and accumulating them in the system matrices. The computation of the active force includes the resolution of the coupling ODE and takes 100ms. Regarding the hyperelastic material law, the accumulation consists in iterating over all the Gauss nodes and computing the SPK and elasticity tensors, it takes 200ms. The resolution of the free motion takes 1.2s and yields the free position and free velocity of the mesh points ; it consists in the resolution of the dynamical system using the conjugate gradient method. The second stage of the free motion consists in solving the constraints to find the value of the Lagrangian multipliers. It includes building the constraints direction, projecting into the constraint space, solving the constraint law with the Gauss-Seidel algorithm, and applying the motion correction. At the end of the time step, the new state vectors are propagated to all nodes of the simulation using mappings. In this case, each time step was 4.8s and the whole simulation took 13min.

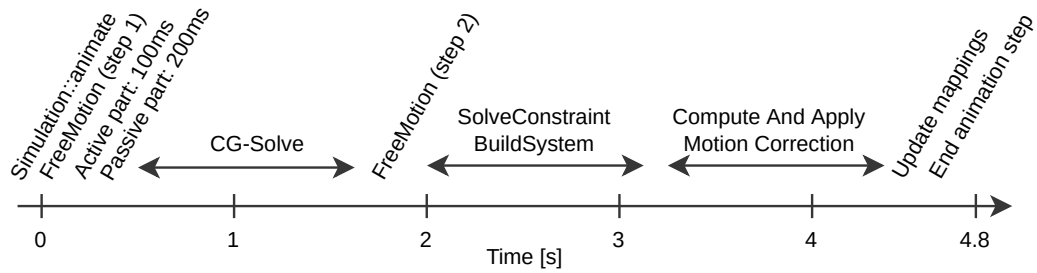


Fig. 4.15.: Time sequence during a time step of the mechanical simulation. During the first step of the freemotion, the computation of the active stress tensors and the passive hyperelastic material response take 300ms, 6.5% of the animation step. Then the resolution of the non-constrained system takes 1.2s, a quarter of the whole animation step. Finally, the resolution of the constraints takes approximately half of the iteration with 2.4s. For a 0.8s cardiac cycle and a time step $\Delta t = 5\text{ms}$, it gives a total simulation time of 13min.

Personalization of the electromechanical model

5.1	Personalization methods	95
5.1.1	Features extraction and dimension reduction	95
5.1.2	Personalized parameters	99
5.1.3	CMA-ES	102
5.1.4	Implementation of the optimization on a cluster	103
5.1.5	Regression with machine learning methods	103
5.2	Personalization of the model	106
5.2.1	Anatomical personalization	106
5.2.2	Electrophysiological personalization	106
5.2.3	Mechanical personalization	107
5.3	Prediction of the therapy response	108
5.3.1	Description of the protocol	108
5.3.2	Results	109
5.3.3	Discussion	110

This chapter presents two contributions. The first one is related to the definition of ECG features that enable the computation of the relative error between two QRS tracings. By using the segmentation of the QRS waves, it reduces errors related to QRS segmentation and signal noise, and relies instead on meaningful features. The second contribution consists in a personalization method which is based on learning a reduced representation of the model to estimate the parameters with regression methods. Together with the segmentation of QRS waves, it offers an efficient treatment of ECG by machine learning algorithms and focuses on fitting successive QRS waves rather than scattered points. This method is also used for the estimation of mechanical parameters based on meaningful cardiac indices for CRT. This personalization method is extremely fast as compared to optimization methods and would allow the whole personalized simulation flow to run in a clinical context.

This chapter presents how the cardiac electromechanical model developed previously can be personalized to a specific patient. This process consists in estimating the parameters

of the model so that the computed observations match the available measured patient data. Estimating model parameters is a complex inverse problem that has been addressed before but is impaired by high computational cost which increases with the number of parameters to estimate.

These algorithms are highly dependent on the initial set of parameters in order to converge. [Molléro et al., 2019] uses the unscented transform algorithm to calibrate the parameters but requires at least one iteration of parallelized model computations. Here we propose to use a set of precomputed models to generate a good approximation of the solution. This method requires high offline computational workload but has the advantage of generating a solution in less than a second.

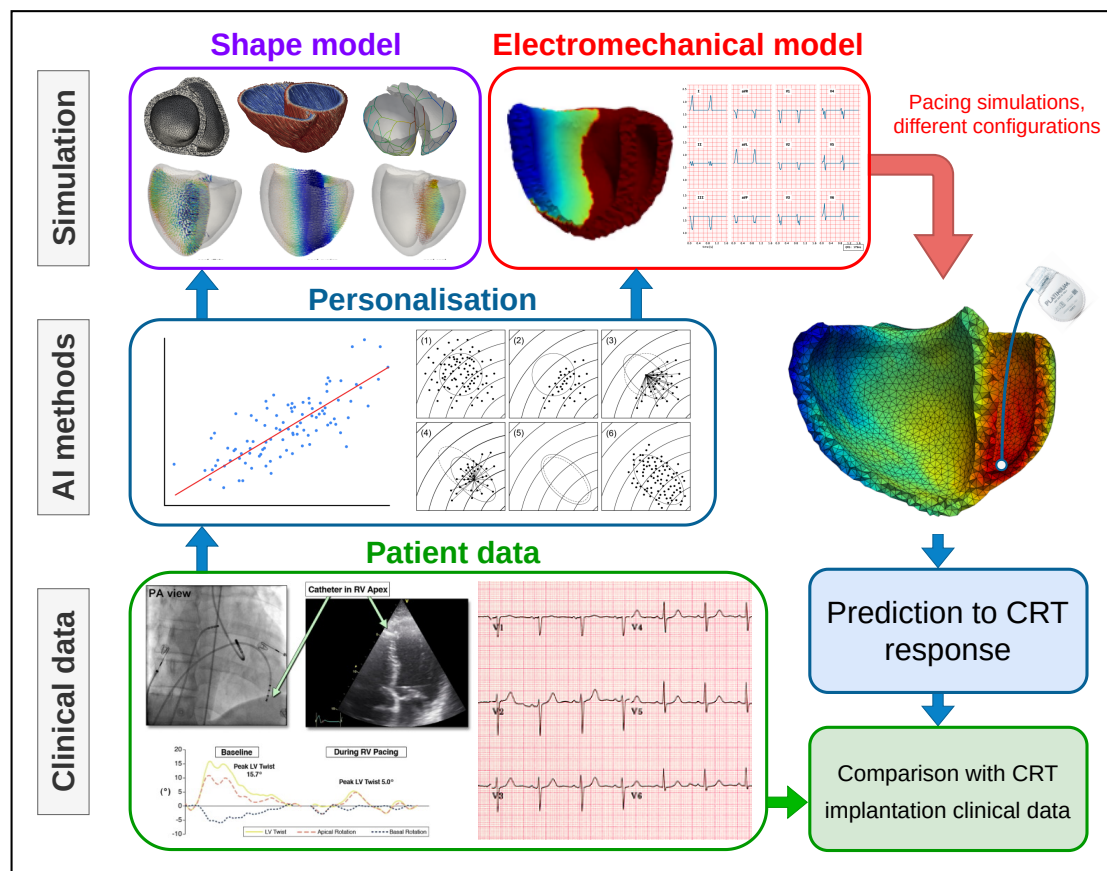


Fig. 5.1.: Global pipeline for patient-specific simulations and prediction to CRT response

Fig. 5.2 presents the whole data flow of the cardiac framework presented in this thesis. At the top of this diagram is the patient data that is used for the personalization of the model and is decomposed in four blocks:

1. Anatomical data extracted from echocardiography: it includes ventricles volume, wall and septal thickness, diameter and apicobasal distance,
2. Anatomical data extracted from the patient record or by the clinician: it includes general data about the shape of the patient's body,

3. Electrophysiological data, consisting in a numerical ECG from where the QRS axis will be segmented, and its duration and axis computed,
4. Mechanical data extracted from echocardiography, including the eighteen parameters presented in [Cazeau et al., 2019].

All the patient data is used as the target in the personalization methods. At the bottom of the diagram are represented the datasets that are used to train and test the machine learning algorithms. They are generated using a large number of simulations, followed by an extraction of meaningful features. The data flow starts with the template geometry which is fitted to patient data with the deformation model. Then, an activation map is produced so that the simulated ECG matches the patient's one. Finally, this electrical input is used on the personalized geometry to compute the personalized biomechanics. Optionally, it is possible to run the complete personalized model with several pacing configurations to compare the outcome, both in terms of electrophysiology and mechanics.

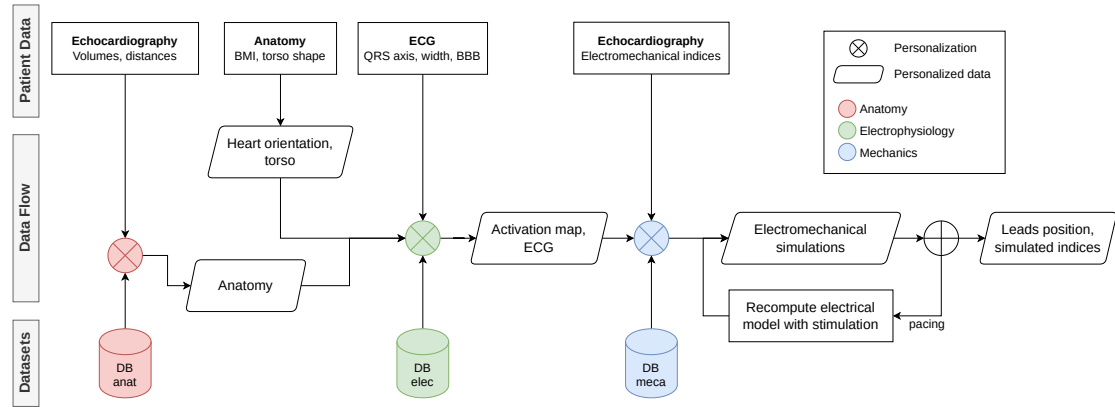


Fig. 5.2.: Data flow for the complete personalized cardiac model. The patient data is used at different steps of the pipeline for the estimation of patient-specific parameters. Learning algorithms can be trained based on several databases.

5.1 Personalization methods

This section introduces the different personalization methods that have been implemented. In any case, it is necessary to define first the parameters that will be estimated and the features that will best describe each model's output.

5.1.1 Features extraction and dimension reduction

Anatomical features

The anatomical features have already been presented in Tab. 2.1 since they constitute the main measures on the deformed mesh: ventricles' volume, septal thickness, diameter

and apicobasal distance. These five features offer a complete description of the deformed mesh for the selected cardiomyopathies.

Electrophysiological features

Several features can be considered to describe the ECG whether they are used for optimization or learning algorithms. In Fig. 5.3, three computation methods are introduced. The first method (left) is used in [Giffard-Roisin, 2017] and consists in the extraction of points of interest on the QRS, such as zero-crossings or signal extrema. This extraction can be performed on any QRS complex but is not robust to noisy signals containing a high number of extrema, or oscillations around 0mV. Also, the total number of features greatly depends on the quality of the signal, it can range from a few features to hundreds of them for the whole ECG, which makes it even more difficult to compute errors between tracings. Finally, this method yields features of different natures and comparing integers (such as number of zero-crossings) with scalars (such as maximum voltage) adds another layer of complexity.

The second method presented in Fig. 5.3 (center) has been proposed as an alternative to the first one and is also intended for optimization algorithms. Instead of a variable number of features, only the five segmented waves (Q, R, S, R', S') are included in the computation of the error, as well as the QRS duration, which is a global measure on the ECG. For each wave, we define a triangle formed by the peak and two points at half prominence. To define the error computation with this second method, let's consider two ECG that we seek to compare. k represents either the ECG that has been generated by the model, or the one coming from the patient data, referred as 'ref'. W_k refers to the waves of signal k , T_k to the triangle associated to each wave and $P_k(x)$ is the distance to the signal k at potential x , used when no matching wave is found in the signals. Taking the signals voltage difference ensures that even when no matching wave is found but the tracings are close, the error remains low. Algorithm 1 presents how the error between two ECG is computed.

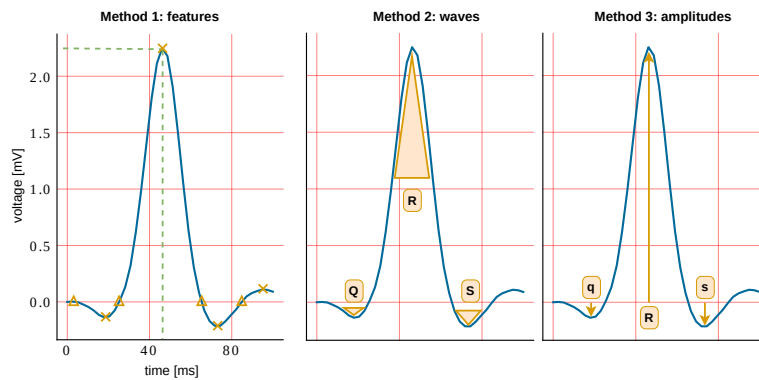


Fig. 5.3.: ECGs comparison methods. Method 1: features from [Giffard-Roisin, 2017] ; method 2: triangles at half-prominence ; method 3: waves amplitudes.

Algorithm 1 Computation of ECG error based on QRS waves

Ensure: both model and target ECG signals pre-processed

1. Segment one QRS in the ECG signal
2. Detect the Q, R, S, R', S' waves in signals based on peak sign and peaks detection algorithm
3. Compute the triangle T associated to each peak
4. For each derivation i , compute the error as follow:
for wave in (Q, R, S, R', S') **do**
 if wave in W_{ref} **then**
 if wave in W_{model} **then**
 $E_i+ = D(T_{model}, T_{ref})$ ▷ wave present in both QRS
 else
 $E_i+ = P_{model}(v_{ref})$ ▷ wave only in reference
 end if
 else
 if wave in model **then**
 $E_i+ = P_{ref}(v_{model})$ ▷ wave only in model
 else
 $E_i+ = \infty$ ▷ other waves
 end if
 end if
end for
5. Gather all derivations contributions

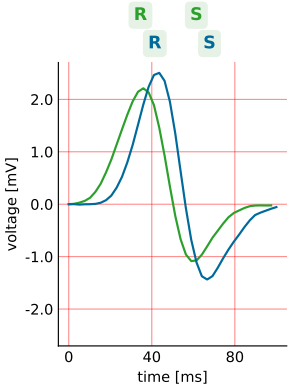
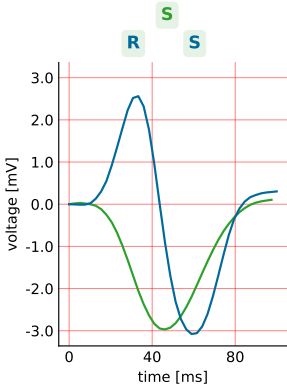
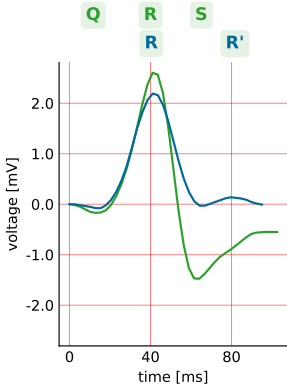
$$E_{tot} = \|E_i\|_{\infty}, \forall i \in \{I, \dots, V6\}$$

D is the distance between two triangles. It can be a direct measure such as the distance between the two barycenters, or a more elaborated metric, for instance including the areas or the deformation of the model's triangle as compared to the reference one. Similarly, the total ECG error can be computed from derivations error based on any metric such as L^{∞} or L^1 . Lastly, the difference between QRS durations can also be incorporated into the total error. In this case, special care must be given to the coefficients associated to each error since the scales might be different.

The third method presented in Fig. 5.3 (right) is derived from the second one and only includes the signed amplitude of the five waves, as well as the QRS duration. It is intended for machine learning algorithms since it provides a fixed 61-length vector of features that describes well the activation patterns in each derivation.

A last comparison method that is implemented consists in computing the Mean Squared Error (MSE) between the two signals and summing over all derivations. It is a good approximation of the error but has no physiological knowledge of the signal. For instance, two signals that have the same waves but a non-zero time shift will have a high MSE error. Tab. 5.1 presents a comparison of these methods.

Tab. 5.1.: Three comparisons of the four methods computing the error between two QRS tracings (in blue and green). For each method, the error is detailed

						
Features	t ext	0	t ext	0	t ext	0
	abs ext	0.043	abs ext	0.006	abs ext	0.084
Amplitudes	sign ext	0	sign ext	0	sign ext	0
	n ext	0	n ext	0.100	n ext	0.100
Waves	nb zeros	2	nb zeros	0.500	nb zeros	2
	sign first	0	sign first	1	sign first	0
MSE		0.131		0.052		0.091
Features	R	0.121	R	1.026	Q	0.020
	S	0.000	S	0.408	R	0.037
Amplitudes	QRS-W	0.012	QRS-W	0.003	S	1.132
		0.137		0.930	QRS-W	0
Waves						0.560
MSE	R:R	0.014	S:S	0.026	Q:	0.342
	S:S	0.008	:R	2.562	R:R	0.018
MSE		0.099		4.353	S:	1.476
					:R'	0.014
						2.661
		0.456		2.181		0.398

In Tab. 5.1, each column corresponds to a case example, where the error is computed between the blue and green ECG tracings. It can be observed that the two ECG in the first column are very close, they present the same waves (R and S). In the second column, the tracings are quite distinct, the R wave is not present in both signals. Finally, the example in the last column is more complex. The Q wave has not been detected in the blue signal because of its height, and the last waves are S and R' in the green and blue signals, respectively.

With the first method, the lowest error is obtained for the second example, which seems to have the worst correspondance between tracings. Regarding the waves method, the R wave has not been detected in the green signal, although it is present in the blue one. In this case, the error is computed based on the distance between both tracings, at the timestamp of the R wave, leading to an important penalization term for this wave. Similarly, the difference between the S and R' waves in the third columns generates a large error.

Mechanical features

The features used to quantify the output of the mechanical model are based on [Cazeau et al., 2019]. This choice comes from the fact that these parameters are meaningful for the current study since they are able to describe dyssynchrony and the response to CRT.

Because the beginning of the QRS and the time of each cardiac phase change is known during the simulation, the computation of the following mechanical features is straightforward: QRS-A, LPEI, RPEI, IVD, IsoC, LVET, IsoR, QRS-E (see Fig. 1.10 for a schematic view of these durations). To compute the time at which the maximum contraction of cardiac segments is reached, the points of interest defined in Fig. 4.8 are used by projecting their displacement onto the small axis plane, corresponding to the M-mode used in echocardiography. Then, from this peak contraction, the following features are found: SegC, DC, and the overlap (duration during which the cardiac segments are still contracting during the filling phase).

5.1.2 Personalized parameters

The models developed in this thesis, besides focusing on the computation time, target a few set of explainable parameters and are therefore adapted to personalization. This section presents the parameters that are selected for personalization. They have been chosen based on the sensitivity analysis presented in the previous chapters.

Anatomy

As for the anatomical features, there are already very few parameters that influence the output of the anatomical model so that the five parameters k_r , k_z , k_{dilate} , $k_{overlap}$ and k_{sept} can be estimated independently to produce meshes that feature the required data.

Electrophysiological personalized parameters

For the personalization of the ECG, the main parameters of the electrophysiological model are estimated:

- depolarisation delay of the Purkinje breakthrough points (corresponding to the InterV bundle delay parameter presented in Fig. 3.10),
- conduction velocity of the Purkinje network σ_{purk} (each ventricle),
- conduction velocity of the thin endocardial layer σ_{endo} (each ventricle),
- conduction velocity of the remaining myocardial tissue σ_{myo} (each ventricle),

which makes seven parameters to estimate. Note that although the conduction velocities are set globally in this chapter, it is possible to define them locally (for instance defining BBB or myocardial infarction). Other global parameters such as those related to Purkinje generation, fiber angles, anisotropy ratio, etc., are not included in the personalization.

The personalization of the Purkinje network generation model is not included in this study. A method to estimate the Purkinje activation from ECG tracings is available in [Giffard-Roisin et al., 2016; Barber et al., 2021].

Mechanical personalized parameters

Several parameters influence the mechanical model output, here are the most meaningful for the personalization:

- three elements of the Windkessel model (R_p , τ and R_c). Note that the parameters for the right ventricle are adjusted according to those of the left ventricle and are not included in the personalization,
- Mooney-Rivlin material parameters (the bulk modulus K and the stiffness $c1$),
- contraction a and relaxation g parameters,
- sarcomere maximum contractility σ_0 .

which makes eight parameters to estimate.

For all models, the selected parameter values are defined within ranges that depend on the simulated scenario. Given a patient's condition (healthy, LBBB, etc.), the search space is adapted to the condition in order to reduce the variability in the model's outcome. Tab. 5.2 presents the various model parameters that have been used for the constitution of the datasets.

	Name	Healthy		DCM + LBBB		Unit
		<i>baseline</i>	<i>range</i>	<i>baseline</i>	<i>range</i>	
Anat	k_r	1		1.15	0.9, 1.3	
	k_z	1		1	0.9, 1.1	
	k_{dilate}	0		3.6	0, 10	
Elec (LV)	Bundle delay	10	-20, 30	$+\infty$		ms
	σ_{purk}	3	0.1, 6	2.4	0.1, 4.8	m/s
	σ_{endo}	1.6	0.1, 4	1.3	0.1, 3.2	m/s
	σ_{myo}	0.8	0.1, 3	0.6	0.1, 2.4	m/s
Meca	contractility	6e5	2e5, 1e6	4e5	1e5, 1e6	Pa
	stiffness	4e4	2e4, 8e4	5e4	3e4, 1e5	Pa
	active a	2	0.5, 4	2	0.5, 4	
	active g	2	0.5, 4	2	0.5, 4	
	R_p	6e7	3e7, 3e8	8e7	3e7, 3e8	Pa·s/m ³
	τ	0.8	0.2, 4	0.8	0.2, 4	s
	R_c	3e6	1e6, 1e7	3e6	1e6, 1e7	Pa·s/m ³

Tab. 5.2.: Baseline and range of variation for the parameters selected for personalization.

5.1.3 CMA-ES

Now that we have defined the model parameters that we seek to estimate and the features that are used to evaluate the output of each model, a first optimization method is presented.

The Covariance Matrix Adaptation Evolution Strategy (CMA-ES) is an evolutionary algorithm for difficult non-linear non-convex black-box optimization problems [Hansen, 2006]. The parameters are sampled according to a multi-variate normal distribution. The covariance matrix of this distribution is iteratively updated such as the new set of parameters minimizes the cost function, see Fig. 5.4. The latter is built such that the output of the model with the current parameters fits the patient data, based on the features presented in the previous sections. Moreover, this personalization method is embarrassingly parallel, as all simulations are independent within an iteration. However, the full computation of the model is still necessary and, even in parallel, the CMA-ES method can take hours to converge.

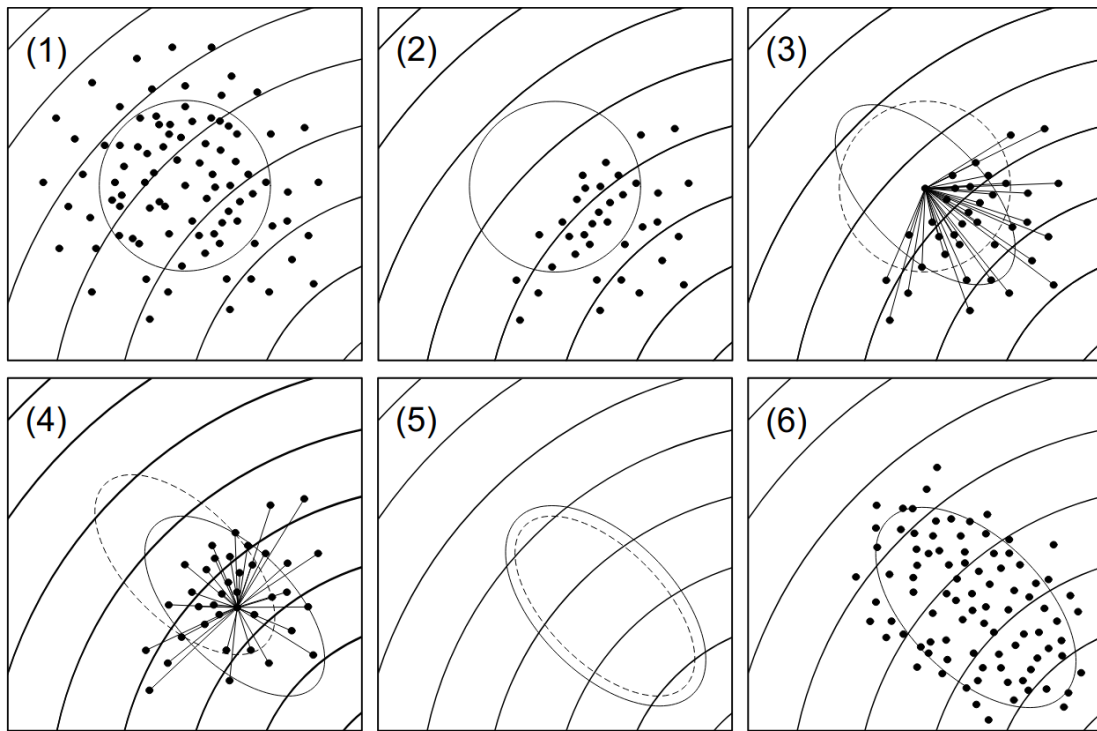


Fig. 5.4.: CMA-ES procedure: (1) Generate multiple candidate solutions. (2) Evaluate and rank the solutions based on the objective function. (3) Update the covariance matrix. (4) Shift the center of the distribution to the weighted mean vector. (5) Update step size. (6) Generate multiple candidates at the next step. Source: [Maki et al., 2019]

5.1.4 Implementation of the optimization on a cluster

Some details regarding the implementation of the CMA-ES method on a High Performance Computing (HPC) cluster are given in this section. Indeed, choosing the appropriate resources to run the optimization can be difficult. The available cluster uses OAR, a resource and task manager, to parallelize the cardiac model computations using queued jobs submissions. Throughout the CMA-ES generations, these jobs are managed by the python package dask [Rocklin, 2015], which handles the lifecycle of one model computation, (i.e., one member of the population in CMA-ES). Fig. 5.5 shows the resources used by the personalization of the ElecModel with the CMA-ES method.

Additionally, because the Purkinje and ECG generative models are parallelized using multithreading with disabled Global Interpreter Lock (GIL), it is necessary that each process has one and only one ElecModel instance running on one thread, so that the memory is not shared by several instances. The number of processes per cpu core is not limited but optimal performance is obtained near $n_{\text{proc}} \approx n_{\text{core}}$.

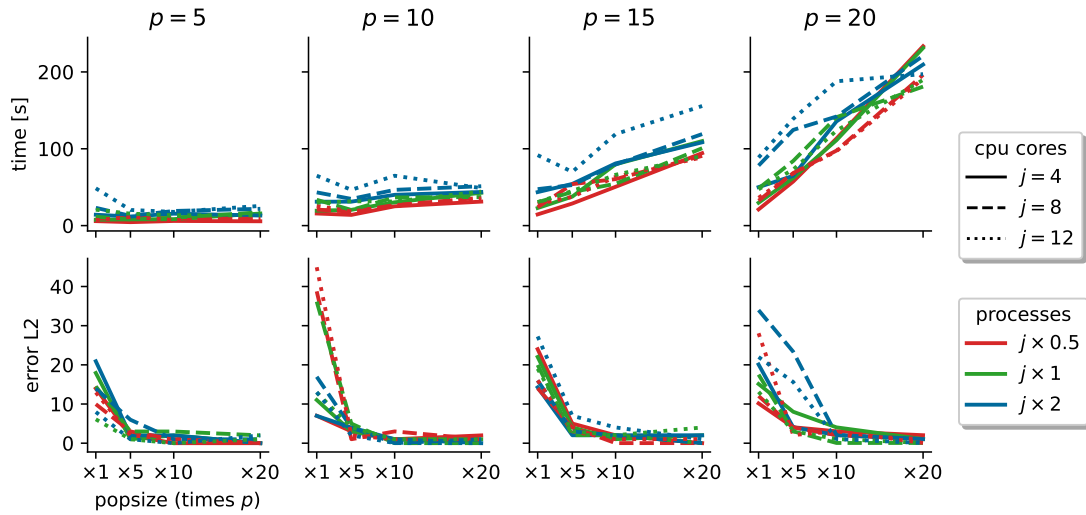


Fig. 5.5.: Comparison of the impact of the number of model parameters (p), required cores (j), number of processes on the error and computation time for a simple CMA-ES personalization of the electrophysiological model.

5.1.5 Regression with machine learning methods

To alleviate the need for the full model computation as in the CMA-ES method, the idea behind the tools presented in this section is based on the evaluation of a reduced representation of the model, that is much faster to compute. Using surrogate models for personalization has already been explored in [Mollero, 2017] and seems promising. In this work, a 0D model, surrogate to the 3D mechanical model, is used to iteratively

provide prior values in the CMA-ES personalization, thus speeding up the convergence of the estimation in a multi-fidelity manner. However, although they are based on the same equations, the OD and 3D models do not behave identically and further calibration work is needed to find a correspondance between both outputs. Furthermore, the computation times reached with this method are still high since the computation of the full model is still required sometimes. Additionally, this inverse problem is ill-posed, as different sets of parameters can produce similar output features. Therefore, regularization is needed to ensure uniqueness of the solution. In our personalization method, prior knowledge is based on the patient condition and is used when generating training data, therefore it acts as a regularization term in the objective function to be minimized.

The parameter estimation problem can be seen as a regression problem and is evaluated with supervised machine learning methods. Datasets composed of thousands of simulations output are generated offline. The parameters used in these simulations are sampled with the LHS method. Six datasets are constituted for the three models:

- anatomical dataset for the anatomical model containing healthy, DCM and hypertrophic geometries (500 cases),
- healthy electrophysiological dataset for healthy patients, on a healthy geometry (500 cases),
- LBBB electrophysiological dataset for LBBB patients, DCM (2000 cases),
- RBBB electrophysiological dataset for RBBB patients, DCM (2000 cases),
- healthy mechanical dataset for healthy patients (1000 cases),
- pathological mechanical dataset for desynchronized patients, DCM (1000 cases).

The datasets are scaled by their standard deviation so that all features have a standardized range of values. The mean is conserved since most of the values are not centered.

Three algorithms are implemented:

- Ridge: linear regression with penalization, a linear parametric method,
- K-nearest neighbors (k-NN) algorithm, a non-parametric method for weighted average among neighbors,
- Multi-layer Perceptron regressor (MLP), a simple neural network.

	Train MSE	Test MSE
Ridge	1.59	1.63
k-NN	1.54	1.55
MLP	1.45	1.77

Tab. 5.3.: Inverse problem.

	Train MSE	Test MSE
Ridge	1.30	1.20
k-NN	0.98	0.83
MLP	1.56	1.33

Tab. 5.4.: Forward problem.

The datasets are split in training and testing sets. Then, a 10-fold cross validation and grid search on algorithm-specific parameters are performed. The regression problem can either make a prediction of the parameters given the features, referred as the inverse problem ; or make a prediction of the model's output based on given parameters, referred as the forward problem. Tab. 5.3 and Tab. 5.4 present the train and test errors for the selected machine learning methods and for the inverse and forward problems applied to the electrophysiological model. The MSE corresponds to either the error computed on the estimated parameters (inverse method), or on the reduced representation of the ECG (forward method).

With the forward method, a CMA-ES optimization is performed on the reduced representation of the model given by the regression learning algorithm. In this way, we combine the speed of machine learning algorithms with the non-linear global minimization offered by the CMA-ES optimization method. From now on, this method will be referred as AI-CMA-ES.

Fig. 5.6 presents both the forward and the inverse methods, as well as the pure CMA-ES optimization. These three methods are alternatives and the personalization time is indicated on the right. In all cases, the personalization task consists in estimating parameters from the 61-length vector (amplitudes of five waves for the twelve derivations and the QRS duration) that constitutes the reduced representation of the ECG tracings.

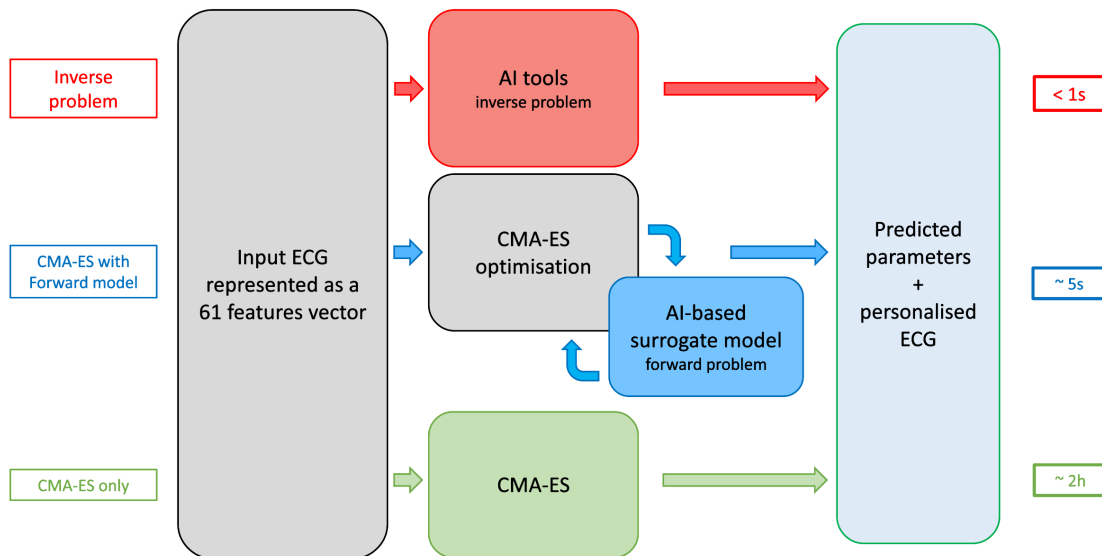


Fig. 5.6.: Implemented methods for the personalization.

5.2 Personalization of the model

This section presents some personalization results on the three models presented in the previous chapters.

5.2.1 Anatomical personalization

Using the datasets and methods presented in section 5.1.5, the personalization of the anatomical model have been performed first. Fig. 5.7 shows the errors on the test set for the AI-CMA-ES method. Fig. 5.7a shows the errors on the estimated parameters, relative to their variation range. Fig. 5.7b presents the relative errors on the anatomical features.

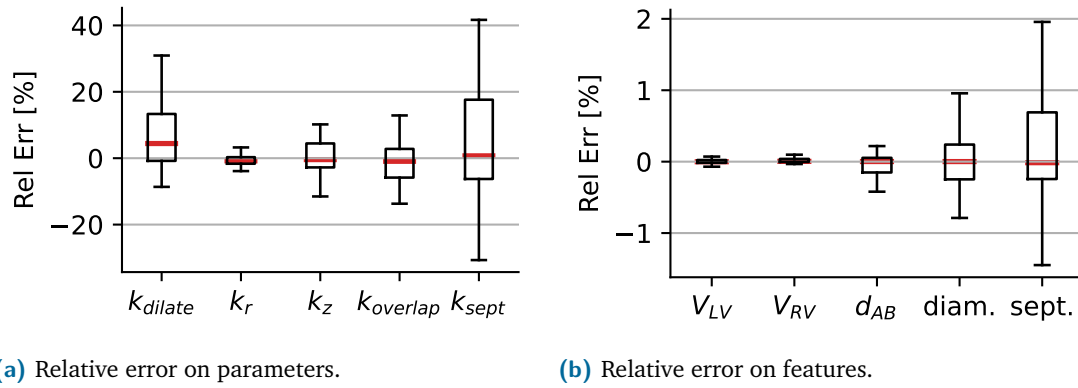


Fig. 5.7.: Anatomical parameters estimation and features prediction error on the test set using the forward personalization method (AI-CMA-ES).

5.2.2 Electrophysiological personalization

Fig. 5.8 presents the personalization results for both the inverse (top) and the forward (bottom) methods, with different metrics for healthy cases. The first column corresponds to the error in the QRS duration, it is around 25ms. The second and third columns are related to the five waves segmented on the QRS, they correspond to the number of waves that are present on both the target and generated ECG for the first column, and the waves that are present on the predicted ECG but not on the reference one, referred as 'false positives'. The fourth column corresponds to the metric defined in algorithm 1 and the last one to the MSE computed on the QRS signal.

There is not a significant difference between the errors obtained with the inverse parameters estimation and those obtained with the forward method coupled with CMA-ES, but the latter offers slightly best results and realistic ECG. The error on the QRS duration is divided by two and the waves error is better with the AI-CMA-ES method. It seems

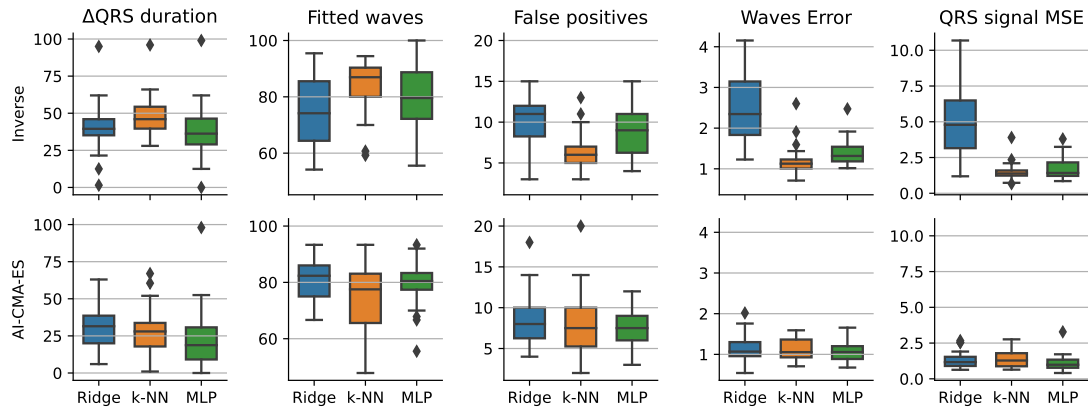


Fig. 5.8.: Errors of the electrophysiological personalization on healthy cases with the machine learning inverse estimation and with the forward AI-based CMA-ES method, presented for several metrics.

that using the CMA-ES optimization algorithm standardized the errors and reduced the differences between the ML methods. This might be due to the global convergence of CMA-ES that iteratively reduces the parameters space, used for ML predictions of the ECG features.

Overall, the best results were obtained with the MLP coupled with the CMA-ES optimization, in all the considered metrics. It has for instance the best ratio of fitted waves versus false positives. Since the relation the electrophysiological parameters and ECG features is highly non-linear, it was expected that k-NN and MLP make better approximations. Furthermore, it can be observed on Fig. 5.8 that the errors related to LBBB cases are higher than those of healthy cases.

5.2.3 Mechanical personalization

An example of the whole model personalization is presented in this section, through several case studies and with data coming from the dataset presented in section 1.3.3. In the first trial only the ejection fraction is included in the mechanical personalization, presented in Tab. 5.5. For this patient data, the anatomical and electrophysiological models have been personalized and yield acceptable results (error around 10% as

	Vol IV [mL]	QRSd [ms]	QRSa [°]	EF 1 [%]	EF 2 [%]
Target	250	150	-30	30	40
Model	249	160	10	26	38
Rel Err.	-0.4%	+6.6%	+11.1%	-13.3%	-5.0%

Tab. 5.5.: Results of the personalization for anat, elec and meca (EF).

compared with the target data). For the mechanical model, the parameters have been estimated trying to fit two examples of EF, 30 and 40%. After the personalization, the obtained EF are 26 and 38%, respectively.

A second experiment was run with more mechanical indices, as presented in Tab. 5.6. The choice of these indices lie in the fact that they are able to describe 87% of the dyssynchrony [Cazeau et al., 2019]. Again, the personalization of the anatomical and electrophysiological models yield satisfactory results, with an error inferior to 5%. Regarding the mechanical personalization, the LPEI has been largely overestimated by the method but the other indices are within acceptable range. The Sept-LLW index is mostly impacted by the electrical conduction velocities set on the LV, which might have been a little overestimated for this index. However, with a reduced LV conduction velocity, the LPEI would have been even higher.

	Vol LV [mL]	QRSd [ms]	QRSa [°]	EF [%]	QRS-E [ms]	LPEI [ms]	Sept [ms]	Sept-LLW [ms]
Target	250	210	0	35	576	170	514	-114
Model	249	220	0	31	615	265	465	-75
Rel Err.	-0.4%	+4.7%	0	-11.4%	+6.7%	+55.8%	-9.5%	-34.2%

Tab. 5.6.: Results of the personalization (for the mechanical model, only the EF and four indices that describe 87% of the dyssynchrony have been included in this personalization).

5.3 Prediction of the therapy response

This section presents the simulation experiment performed to evaluate the prediction of CRT response, based on real patient data.

5.3.1 Description of the protocol

The dataset provided by Microport CRM and presented in section 1.3.3 includes patient data for different pacing configurations. The CRT was gradually conducted, adding one lead at a time and up to three leads for the following steps: start, RV, LV, BiV, final. For each configuration, the localization of the stimulation is indicated, which enables to reproduce the stimulations in silico. Regarding the patient selection, we will focus on sinus rhythm patients with DCM. Fig. 5.9 shows the different pacing points on the DCM geometry. These points are selected according to the available patient data.

For each patient, several data (QRSd, QRSa, EF) are unknown at each step but only available before and after the implantation. Because the ECG has not been measured

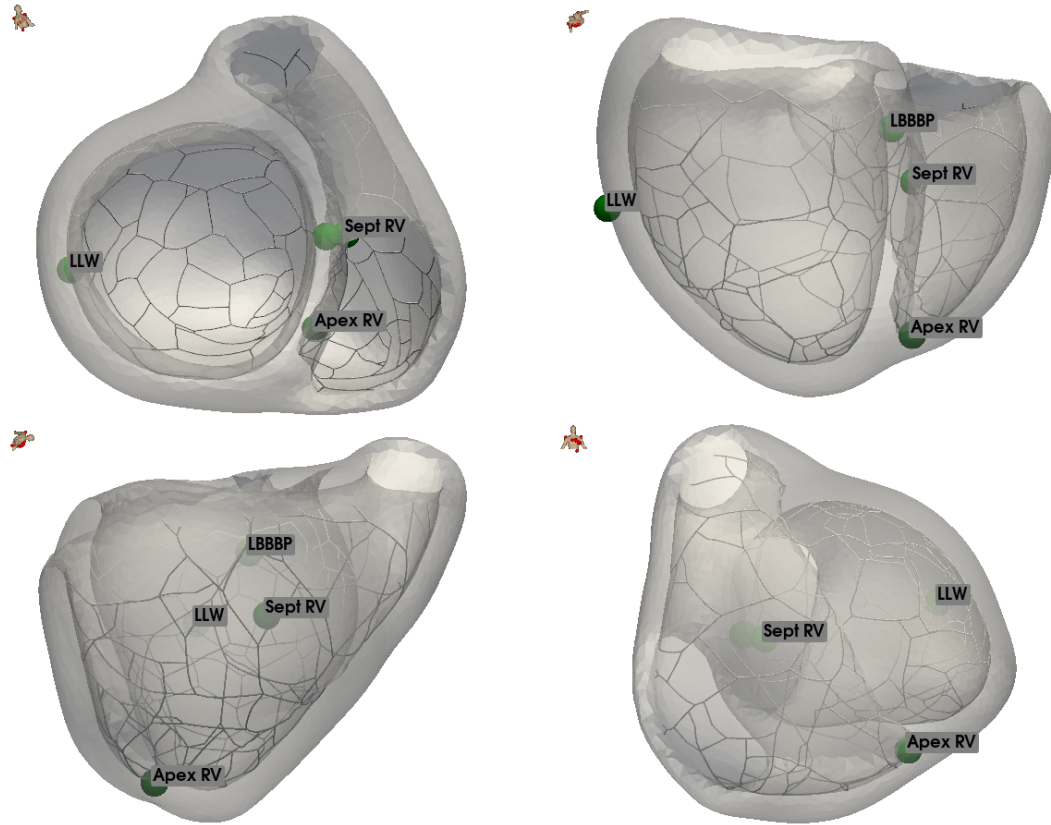


Fig. 5.9.: Localization of the pacing sites as per the patient data from different views.

with the data and is not available, an ECG with similar features is extracted from the ECG dataset presented in section 1.3.2. From this ECG and the available data before the implantation, the electrophysiological and mechanical models are personalized with sinus rhythm simulation. Then, for each pacing configuration, the corresponding stimulation protocol is simulated and the predicted electromechanical indices are extracted and compared to the patient data. It is important to note that all pacing simulations are done in full capture, thus overriding the spontaneous His activation.

5.3.2 Results

Fig. 5.10 presents the personalization and prediction of CRT response results for one patient of the dataset provided by Microport CRM. The models are personalized on the patient data before CRT ('start' step) and then used without any modification of the parameters, in the other steps of the implantation.

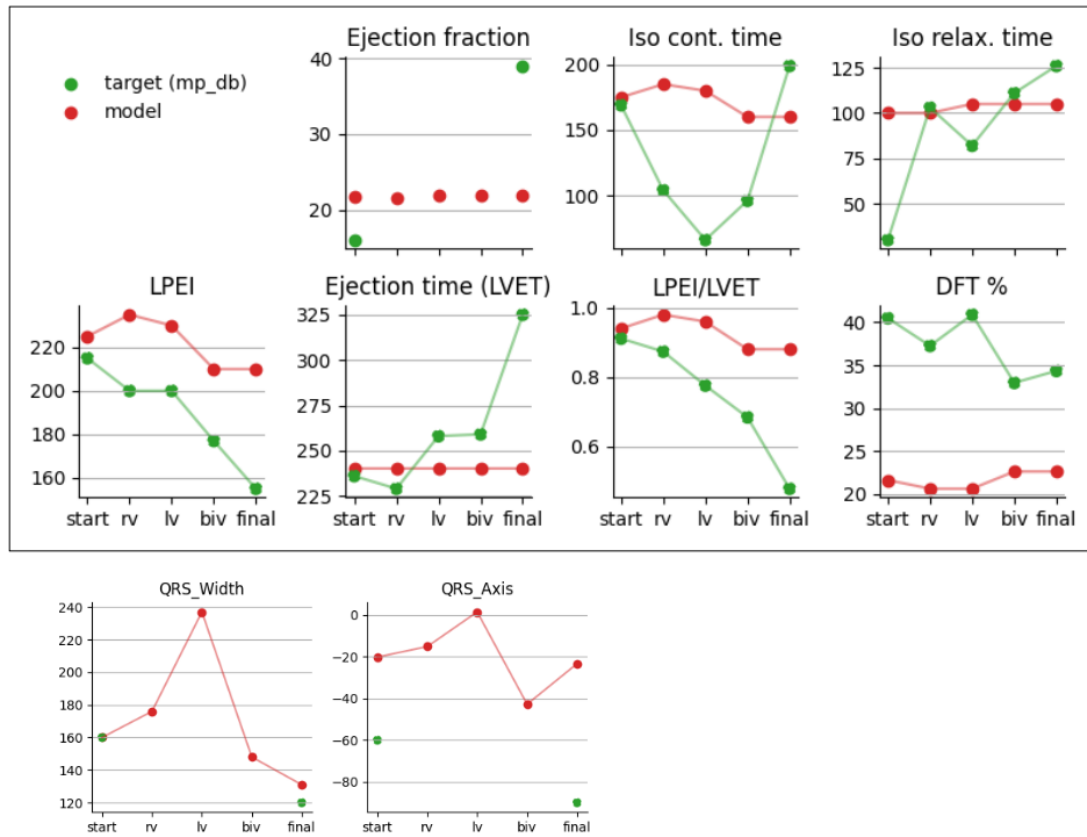


Fig. 5.10.: Results of the personalization and model prediction of CRT response (red) for one patient of the dataset (green). ‘start’: spontaneous activation, ‘rv’: stimulation in the RV septum, ‘lv’: LVFW stimulation, ‘biv’: RVFW+LVFW, ‘final’: TIV for this patient, RVSept+RVFW+LVFW.

5.3.3 Discussion

The results presented in Fig. 5.10 account for the simulation of the CRT, with different leads placement. First, we can observe that the personalization of the indices before the implantation lead to values close to the patient’s ones. The QRSd, LPEI, LVET and IsoC are all within a 10% range error.

The prediction follows the right trend for some indices (LPEI, LPEI/LVET). The LPEI is a good indicator of the early contraction, it increases for single lead stimulations (probably due to the capture and the propagation from one single point) as compared to the ‘start’ step (simulation personalized with QRSd=160ms and QRSa=-60°). For BiV and TIV stimulations, the LPEI and QRSd both decrease, sign that the recovered electrical activation has improved the results.

However, some changes are not properly captured. In particular the changes in iso-volumetric contraction duration are not large enough yet. This is probably due to the

electromechanical coupling and its interaction with the cardiac stiffness. Changes in activation pattern do not impact enough the contraction efficiency. The quasi constant state of the ejection fraction is in accordance with CRT results presented in section 4.3.3. It should also change more, this is probably due to the lack of post-systolic contraction in these diseased simulations. Adapting action potential duration and analyzing more the relaxation phase should help in improving this.

The lack of anatomical data (like imaging) and of the patient ECG also impacts the personalization possibilities, and therefore the prediction accuracy. Working with more complete clinical data would enable to better capture the patient-specific parameters.

Conclusions

6.1	Contributions	113
6.2	Models limitations	114
6.3	Further improving the computation time	116
6.3.1	Frame-based method	116
6.3.2	Physic-based deep learning	118
6.4	Conclusion	118

The general conclusions of this PhD work are presented in this chapter, as well as a global discussion on the models limitations and further improvements that could be made to increase the robustness of the model and the prediction to CRT.

6.1 Contributions

Overall, the 3D cardiac electromechanical model developed in this thesis is able to reproduce typical scenarios encountered in failing hearts and allows individual personalization from routine standardized patient data. This personalization is easy, fast and cheap to acquire. It is also possible to simulate different configurations of CRT pacing and observe the immediate potential response of the heart. The whole personalized flow takes 30min to run, which makes it compatible with clinical use.

The cardiac simulation framework features some tools that are helpful to start simulations such as an efficient mesh plotter, supporting animations, point and cell picking, camera orientation, and ray tracing. The latter is used in the processing of the input surface mesh to automatically label the cardiac structures. Robust meshing tools were also developed on top of MMG to provide good quality meshes, supporting heterogeneity and anisotropy. They have been used for instance in the deformation model, allowing for the fast and optimized generation of tetrahedral meshes and accounting for the minimal thickness of the myocardium.

Regarding the electrophysiological model, efficient algorithms were implemented and allow for action potential anisotropic propagation simulations to run in under 10s, as quick as the ECG generation model. The development of a Purkinje network and its interactions with the myocardium have been explored and allow to identify typical

deflections on the ECG. Finally, stimulation has been modelled and allows to introduce any number of pacing points as initial condition in the depolarization.

The mechanical model has been re-implemented using the latest versions of SOFA, based on previous works from the team. It allows to use a state-of-the-art constraints formulation within the model. To this end, an implicit discretization of the Windkessel model has been incorporated in the hemodynamic constraint law and is compatible with the computation of contacts and the global implicit solver. Several hyperelastic material laws can be implemented, either differentiated by hand or with automatic tools. It results in realistic simulations that feature expected observations, in terms of heart displacement, strain, wall thickness, and rotation.

Finally, because it defines a few set of explainable parameters, the model is adapted to personalization and a significantly faster personalization method has been developed. It uses machine learning algorithms to predict the model's output in a reduced space and optimization methods to minimize a global cost function, based on patient data. With this personalization method, the models can be customized in a few seconds without the need to perform the full 3D computations, which is attractable to clinical applications.

Because the cardiac model requires only few hardware resources, patients can be managed in parallel, even on laptops, making it possible to study cohorts of patients or even to treat all the patients of a clinician or all the patient data of an external database in a similar way. The complete model is interfaced with simple data exchange protocols such as the JSON text format and can therefore be easily installed on a server communicating with other services such as a web interface, APIs or databases. All parameters used in simulations and personalizations are written in JSON files as well, which simplifies data exchange even more between the different services.

Furthermore, the model has been completely containerized and can be run on any machine having Docker installed, with `docker-compose`. It is therefore extremely easy to use the tools developed in this thesis on any computer. Finally, extensive documentation is available and contains examples to start building cardiac simulations.

6.2 Models limitations

Although the implemented model includes several anatomical structures such as a biventricular geometry, the Purkinje network or the pericardium, the atria are not included. However, their impact is included in the model through the boundary conditions and the analytical pressure formulation. Also, the biventricular geometry used throughout this study present the same aspect, even after the deformation model: the valves are

located relatively at the same place, the walls are smooth and no segmentation artefact is present on the mesh. This is not a problem since no medical images segmentation is planned in the IPRC global project but rather the use of a single geometry that can be personalized by the deformation model. The change of the template geometry should result in a new calibration of all models. It should be noted that several biventricular geometries have been used with this model by members of the team without complications, but no validation has been performed.

Moreover, personalization of the Purkinje network from non-invasive data has not been assessed in this thesis but this complex task has been evaluated from ECG tracings in [Barber et al., 2021; Giffard-Roisin, 2017]. It could be an improvement as compared to the current implementation, in which there is a small variability in the generated networks. Because our Purkinje network starts at the same node on each geometry and has the same direction of propagation, it results in a preferential direction of growth, namely septal to LLW. With these settings, it is impossible for the electrical signal to originate from the His bundles and activate first the LLW, as it has been reported on vectocardiogram. Such homogeneity in the Purkinje activation may be the cause of the reduced variability observed on the generated ECG tracings as compared to real-world ECG data (Fig. 3.14). This network, however, offers a convenient way of defining the PMJ points and modelling BBB.

The conduction velocity imposed on the thin endocardial layer, which models the fast propagation due to subendocardial Purkinje fibers, might also be a strong assumption on the ability of the myocardium to globally conduct the electrical signal. Variants of this model have been tested, such as having only patches of isotropic high conductive tissue around PMJ points instead of the whole endocardial layer, but no conclusions were drawn from these simulations. The density of the Purkinje network has also been investigated: too many PMJ points led to non-realistic oscillations on the ECG tracings.

In a clinical context, the His branch is considered to be the preferred stimulating site since it activates all the intact Purkinje network and allows a quick propagation of the electrical signal to all segments of the heart. Clinicians report that finding the His branch can be quite challenging and that it is a matter of millimeters between pacing the fast conductive network, thus significantly increasing the patient's condition, or stimulating the myocardium and observing close to no improvement. In our model however, even a myocardial stimulation a few millimeters away from the His branch enters rapidly the network and depolarizes all segments which is closer to clinical observations of direct left bundle branch pacing.

Regarding the mechanical model, the response of stimulated hearts needs to be improved. While the improvement of the ejection fraction is typically low in the immediate postoperative period, it is still expected to improve by about 5%, which is not currently observed

in our model. The increase of the $\max\left(\frac{dP_v}{dt}\right)$ is also too small in the pacing simulations. This problem could have several causes in all models but the electrophysiological results suggest that this model behaves correctly to stimulation inputs. The reduced increase in $\max\left(\frac{dP_v}{dt}\right)$ in pacing simulations might be related to the calibration of the myocardial stiffness with the cells contractility. Indeed, without pacing, these two parameters balance each other but with stimulation, too stiff tissue could be an inhibitor to the stimulation benefits, by making it more difficult to contract significantly. Moreover, an increase in this index has been observed for different active stress functions, up to 8%, which suggests that the response to CRT could be related to the profile of contraction. It is possible that the ability of the cardiac cells to contract faster or slower is different in responder or non-responder patients, and is currently explored.

6.3 Further improving the computation time

6.3.1 Frame-based method

This section is based on the following paper:

Towards Hyper-Reduction of Cardiac Models using Poly-Affine Deformation. *Gaëtan Desrues, Hervé Delingette, Maxime Sermesant.* STACOM 2019: Statistical Atlases and Computational Models of the Heart, Oct 2019, Shenzhen, China.

Instead of the 3-coordinate vector displacement field classically used for each point of the mesh, we propose to use a poly-affine displacement field for which at each control node $\mathbf{q}_i, 1 \leq i \leq n$, the 12 DOFs are the 12 coefficients of the affine transformation $\mathbf{T}(\mathbf{q}_i) = \mathbf{T}_i \in \mathcal{M}_{3 \times 4}$ (3 coefficients for the 3D translation and 9 for the linear transformation combining rotation, scaling and shearing). This is well suited to a regional deformation approach, therefore with an important reduction in the total number of degrees of freedom.

The GMLS method was shown to be an efficient method to approximate globally a function from sparse discrete values with a minimization problem [Martin et al., 2010; Fries et al., 2004]. This problem seeks new shape functions $N_i(x)$ representing accurately the function over the whole domain.

$$\mathbf{T}(x) = \sum_{i=1}^n \mathbf{T}_i N_i(x) \quad (6.1)$$

In our framework, this mapping is used to compute the deformation gradients from vertices position at integration points. See [Martin et al., 2010] for an analytical formulation of $N_i(x)$.

Numerical integration in the frame-based framework

The elastic energy of a deformable solid is the work done by the elastic forces between the undeformed and deformed positions, integrated across the whole domain. The numerical integration of the elastic forces is classically performed at the tetrahedron level in regular finite element methods. In our approach, we partition the domain Ω into M integration regions V^m consisting of a set of tetrahedra. In the spirit of our affine frame control nodes, we use a high order integration rule called elastons introduced in [Martin et al., 2010] and generalized in [Gilles et al., 2013]. The classical integration approach assumes a constant force within each integration region V^m . The elaston framework relies on a first order Taylor expansion of the field to be integrated in order to reach a higher level of accuracy. More precisely, a field $f(x)$ is locally approximated as $f(x) \approx \mathbf{F}\tilde{p}$ where \mathbf{F} is a vector containing the value of the field and its derivatives at the center of V^m , and \tilde{p} is the polynomial basis of order α in dimension d , for example $[1, x, y, z]$ at order 1, in 3D. Finally, the integration is performed as :

$$\int_{\Omega} f(x) dx = \sum_m \int_{V^m} f(x_m) dx = \sum_m \mathbf{F}_m \int_{V^m} \tilde{p} dx \quad (6.2)$$

In our approach, the strain and stress are approximated by a first order polynomial function in the vicinity of each integration sample which is estimated thanks to a Generalized Moving Least Square (GMLS) interpolation scheme [Martin et al., 2010].

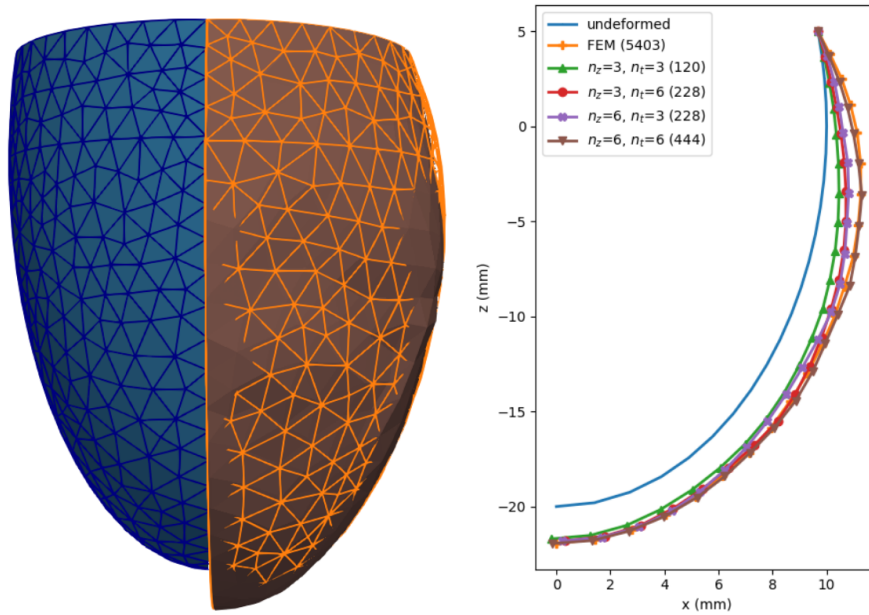


Fig. 6.1.: Left: ellipsoid at rest (blue with edges) and deformed with full (orange wireframe) and reduced (plain brown) models. Right: position of the points on the external surface in the plane $(x^+, 0, z) \cdot n_z$ corresponds to the number of zones on the vertical axis and n_t along the circumference of the ellipsoid (plus one zone for the apex). The number of DOFs of each model is indicated in parenthesis.

Fig. 6.1 presents the deformation of a simplified ventricular model using the frame-based model, after a pressure force has been applied on the endocardium. This approach, although promising, has several issues. As it is visible on the figure, the deformation of the ellipsoid is not uniform and the regions associated to each affine frame are clearly identifiable. Furthermore, the current deformation is very small but unrealistic profiles are obtained with higher pressure values. Finally, with this frame-based method, the boundary conditions are tricky to define since there are no DOFs on the boundary.

6.3.2 Physic-based deep learning

Another promising solution to reduce the computation time of the models is based on the use of deep learning, for instance physics-informed neural networks. Other approaches combine a simple physics-based model with deep learning, for instance in the cardiac electrophysiology context [Kashtanova et al., 2022], and approaches were explored for liver elastic deformations in [Brunet et al., 2019], or left-ventricular biomechanics in [Buoso et al., 2021].

6.4 Conclusion

Overall, the models developed in this thesis constitute a global cardiac simulation framework and progress towards building cardiac digital twins that can be used in CRT. The framework is to be integrated within the IPRC project and would contribute in a completely autonomous workflow for heart failure patients that will help clinicians into making better patient and treatment selection. The long term data acquisition and the use of mathematical models, together with artificial intelligence, constitute major advances in healthcare that can help patients lives, reduce the overall cost, and facilitate the clinical work.

Differentiation of the biomechanical material laws

A.1 Material laws

In the strain energy function of the hyperelastic material laws, an incompressibility penalty term can be incorporated to manage the compression of the deformable body. It is differentiated by hand:

$$W_V = \frac{\kappa}{2} (J - 1)^2 \quad \text{and} \quad \mathbf{S}_V = \kappa J (J - 1) \mathbf{C}^{-1} \quad \text{and} \quad \mathbb{T}_V = \kappa J \mathbf{C}^{-1} \otimes \mathbf{C}^{-1} \quad (\text{A.1})$$

It corresponds to the volumetric part of the strain energy. Any term that cancels for $J = 1$ is suitable for the incompressibility penalty constraint. Another expression in $\ln J$ gives:

$$W_V = \frac{\kappa}{2} (\ln J)^2 \quad \text{and} \quad \mathbf{S}_V = \kappa \mathbf{C}^{-1} \ln J \quad \text{and} \quad \mathbb{T}_V = \kappa \mathbf{C}^{-1} \otimes \left[\frac{1}{2} \mathbf{I} - \mathbf{C}^{-1} \ln J \right] \quad (\text{A.2})$$

A.1.1 Guccione material law

The constant material parameters describe the degree of anisotropy in each direction:

$$\mathbf{H} = \begin{bmatrix} b_f & b_{fs} & b_{fs} \\ b_{fs} & b_t & b_t \\ b_{fs} & b_t & b_t \end{bmatrix}$$

Let $\mathbf{\Lambda}$ be the rotation tensor as described in Appendix B.3.

The strain energy is defined with respect to the locally oriented Green-Lagrange strain tensor $\mathbf{E}_f = \mathbf{\Lambda}^T \mathbf{E} \mathbf{\Lambda}$:

$$W = \frac{\lambda}{2} (e^Q - 1) - \frac{\kappa}{2} (J - 1)^2 \quad \text{and} \quad Q = \mathbf{e}^T (H \circ \mathbf{E}_f \circ \mathbf{E}_f) \mathbf{e}$$

where \circ is the Hadamard product, here between two rank-2 tensors.

Let's now compute the derivatives of the strain energy.

$$\mathbf{Q} = \frac{\partial Q}{\partial \mathbf{E}_f} = 2\mathbf{H} \circ \mathbf{E}_f$$

$$\begin{aligned} \mathbb{Q} &= \frac{\partial \mathbf{Q}}{\partial \mathbf{E}_f} = 2 \frac{\partial (\mathbf{H} \circ \mathbf{E}_f)_{ij}}{\partial \mathbf{E}_{fkl}} \mathbf{e}_i \otimes \mathbf{e}_j \otimes \mathbf{e}_k \otimes \mathbf{e}_l \\ &= 2\delta_{ik}\delta_{jl}\mathbf{H}_{ij} \mathbf{e}_i \otimes \mathbf{e}_j \otimes \mathbf{e}_k \otimes \mathbf{e}_l \end{aligned}$$

Second Piola-Kirchhoff tensor

$$\mathbf{S}_f = \frac{\partial W}{\partial \mathbf{E}} = \lambda e^Q \mathbf{H} \circ \mathbf{E}_f$$

Elasticity tensor

$$\mathbb{T}_f = \frac{\partial \mathbf{S}_f}{\partial \mathbf{E}_f} = \lambda e^Q \left(\mathbb{Q} + \frac{1}{2} \mathbf{Q} \otimes \mathbf{Q} \right)$$

Projection on the euclidian basis

$$\mathbf{S} = \mathbf{\Lambda} \mathbf{S}_f \mathbf{\Lambda}^T \quad \text{and} \quad \mathbb{T} = \mathbf{\Lambda} \mathbb{T}_f \mathbf{\Lambda}^T$$

A.1.2 Fung material law

The Fung law is a generalisation of the Guccione law.

$$\mathbf{H} = \begin{bmatrix} b_{ff} & b_{sf} & b_{nf} \\ b_{fs} & b_{ss} & b_{ns} \\ b_{fn} & b_{fs} & b_{nn} \end{bmatrix}$$

$$W = \frac{\lambda}{2} (e^Q - 1) \quad \text{and} \quad Q = \mathbf{e}^T (\mathbf{H} \circ \mathbf{E}_f \circ \mathbf{E}_f) \mathbf{e} \quad (\text{A.3})$$

The derivation of the strain energy is performed with an automatic differentiation tool, described in Appendic A.2.

A.1.3 Mooney-Rivlin material law

The hyperelastic Mooney–Rivlin model is a special case of the generalized Rivlin model, it has a polynomial form.

Strain energy function

$$W = c_1 (I_1 - 3) + c_2 (I_2 - 3) \quad (\text{A.4})$$

Second Piola-Kirchhoff tensor

$$\mathbf{S} = 2(c_1 + c_2 I_1) \mathbf{I} - 2c_2 \mathbf{C} \quad (\text{A.5})$$

The elasticity tensor is null since $\frac{\partial I_1}{\partial \mathbf{C}} = \mathbf{I}$.

A.2 Automatic differentiation

SymPy is a Python library for symbolic mathematics. We implement the Fung constitutive material law with SymPy syntax.

```
1 b, L, E = MatrixSymbols(...)
2 Ef = L.T * E * L # Projected Green-Lagrange
3
4 # Strain energy
5 Q = (e.T * HadamardProduct(b, Ef, Ef) * e).doit()[0, 0]
6 W = 0.5 * c * (exp(Q) - 1)
7
8 S = diff(W, E) # SPK tensor
9 C = diff(S, E) # Elasticity tensor
```

Listing A.1: Python implementation: AutoDiffSOFAMaterial

and generate the corresponding C++ code (run time=5s) that we implement in a Sofa component inheriting HyperelasticMaterial.

```
1 /**
2  * Generated 'W' = Strain energy
3  */
4 Real W = ...
5
6 /**
7  * Generated 'S' = SPK
8  */
9 Eigen::Matrix<Real, 3, 3> S; S <<
10 ...
11
12 /**
13  * Generated 'T' = Tangent modulus
14  */
```



```
15 Eigen::Matrix<Real, 6, 6> T; T <<  
16 ...
```

Listing A.2: Python implementation: AutoDiffSOFAMaterial

Mechanical model computations

B.1 Constraint-based implementation of the Windkessel 3-element model in SOFA

Let's recall equation (4.34), with \mathbf{P}_{ar} the arterial pressure and \mathbf{Q} the arterial flow.

$$\tau \dot{\mathbf{P}}_{ar} = (R_p + R_c) \mathbf{Q} + \tau R_c \dot{\mathbf{Q}} - \mathbf{P}_{ar} \quad (\text{B.1})$$

We implement the Crank-Nicolson method, an implicit finite difference method that is numerically stable. For the ODE $\dot{y} = f(t, y)$, the Crank-Nicolson scheme reads

$$\frac{y^{i+1} - y^i}{\Delta t} = \frac{1}{2} \left[f(t, y^i) + f(t + \Delta t, y^{i+1}) \right] \quad (\text{B.2})$$

We will use a central finite difference scheme for $\dot{\mathbf{Q}}^i$ and a backward finite difference scheme for $\dot{\mathbf{Q}}^{i+1}$:

$$\dot{\mathbf{Q}}^i = \frac{\mathbf{Q}^{i+1} - \mathbf{Q}^{i-1}}{2\Delta t} \quad \text{and} \quad \dot{\mathbf{Q}}^{i+1} = \frac{\mathbf{Q}^{i+1} - \mathbf{Q}^i}{\Delta t}$$

With these definitions, applying the Crank-Nicolson scheme to equation (B.1) leads to

$$\underbrace{\left(\frac{\tau}{\Delta t} + \frac{1}{2} \right)}_{\alpha} \mathbf{P}_{ar}^{i+1} = \underbrace{\left(\frac{R_p + R_c}{2} + \frac{\tau R_c}{\Delta t} \right)}_A \mathbf{Q}^{i+1} + \underbrace{\left(\frac{R_p + R_c}{2} - \frac{\tau R_c}{\Delta t} \right)}_B \mathbf{Q}^i + \underbrace{\left(\frac{\tau}{\Delta t} - \frac{1}{2} \right)}_C \mathbf{P}_{ar}^i \quad (\text{B.3})$$

which gives an approximation of the arterial pressure at the next time step. Eliminating the next flow \mathbf{Q}^{i+1} will be done by the constraint.

The haemodynamic model during ejection states:

$$\mathbf{Q}^{t+\Delta t} = K_{ar} (\mathbf{P}_{ar}^{t+\Delta t} - \mathbf{P}_v^{t+\Delta t}) \quad (\text{B.4})$$

$$= K_{ar} \left[\frac{A}{\alpha} \mathbf{Q}^{t+\Delta t} + \frac{B}{\alpha} \mathbf{Q}^t + \frac{C}{\alpha} \mathbf{P}_{ar}^t - \mathbf{P}_v^{t+\Delta t} \right] \quad (\text{B.5})$$

$$= \frac{K_{ar}}{\beta} \left[\frac{B}{\alpha} \mathbf{Q}^t + \frac{C}{\alpha} \mathbf{P}_{ar}^t - \mathbf{P}_v^{t+\Delta t} \right] \quad (\text{B.6})$$

with $\beta = (1 - K_{ar}A/\alpha)$.

Let's recall the minimization problem of the constraint law presented in eq 4.35:

$$\mathbf{P}_v^{t+\Delta t} = \min_{\lambda} [\mathbf{W}\lambda + \delta^{\text{free}} - \delta^{\text{free}}] \quad (\text{B.7})$$

Although there is only one scalar equation defining the constraint imposed on each ventricle, this problem is solved with the Gauss-Seidel algorithm, an iterative method used to solve systems of linear equations. This implementation design allows to solve a system of several constraints. $\lambda = \mathbf{P}_v$ is the unknown solution. Here is the solution update for one iteration of the Gauss-Seidel algorithm, with δ^{target} replaced by the hemodynamic constraint law, including the discretized 3-element Windkessel model:

$$\lambda^{k+1} = \lambda^k - \frac{\delta^{\text{free}} - \Delta t \cdot \mathbf{Q}^{t+\Delta t}}{W} \quad (\text{B.8})$$

$$= \frac{\beta \Delta t^2}{\beta W + \Delta t K_{ar}} \left[W \lambda^k - \delta^{\text{free}} + \frac{K_{ar} \Delta t}{\alpha \beta} (B \cdot \mathbf{Q}^t + C \cdot \mathbf{P}_{ar}^t) \right] \quad (\text{B.9})$$

The following is the corresponding implementation in the SurfaceConstraintResolution component of the CardiacModel SOFA plugin. Note that for isovolumetric phases, $\delta^{\text{target}} = 0$ and eq B.8 becomes $\lambda^{k+1} = \lambda^k - \delta^{\text{free}}/W$.

```

1  /*
2   * Resolution of the constraint in SOFA for one iteration of the Gauss-
3   * Seidel algorithm
4   */
5  switch (phase) {
6
7  case Phase::FILLING:
8      lambda[line] = (lambda[line] - delta/W + dt*Kat*next_Pat/W) / (1 + dt
9      *Kat/W);
10     break;
11
12 case Phase::ISOCONTRACTION:
13     lambda[line] -= delta / W;
14     break;

```

```

15 case Phase::EJECTION:
16     // Backward Euler
17     // alpha = 1 - Kar * Rc;
18     // A = Kar*(1-dt/tau)*Par + Kar*dt/tau*( Rp+Rc-tau*Rc/dt )*Q;
19     // lambda[line] = (lambda[line] - delta/W + A/alpha/W) / (1+Kar/alpha
    // W);
20
21     // Crank-Nicholson
22     A = 0.5*(Rp+Rc) + tau*Rc/dt;
23     B = 0.5*(Rp+Rc) - tau*Rc/dt;
24     C_ = tau/dt - 0.5;
25     alpha = tau/dt + 0.5;
26     beta = 1 - Kar * A / alpha;
27     lambda[line] = (W*lambda[line]/dt - delta/dt + Kar/beta/alpha*(B*Q+C_
    *Par)) / (Kar/beta+W/dt);
28
29     break;
30
31 case Phase::ISORELAXATION:
32     lambda[line] -= delta / W;
33     break;
34 }

```

Listing B.1: Resolution of the constraint in SOFA for one iteration of the Gauss-Seidel algorithm

B.2 Volume's derivatives on an open mesh

To compute the volume on an open surface, we consider the closed surface constituted by the open one and a set of virtual triangles defined on boundary edges and the center of the valve. All operations related to boundary edges (such as computing the volume and it's derivatives) is included in the Python project `MeshObject` and in the C++ SOFA component `VolumeAlgorithms`.

Volume

For each hole n , we introduce a point C_n at the center of the valve.

$$C_n = \frac{1}{N_n} \sum_{k=0}^{N_n-1} Q_{H_n(k)}$$

$$V_i = \frac{1}{6} \left| Q_{T_i(0)}, Q_{T_i(1)}, Q_{T_i(2)} \right|$$

$$V_{\text{total}} = \sum_{T_i \in \mathcal{Z}} V_i + \sum_n \sum_{k=0}^{N_n-1} \frac{1}{6} |\mathbf{Q}_{H_n(k)}, \mathbf{Q}_{H_n(k+1)}, \mathbf{C}_n|$$

Volume derivative

$$\frac{\partial V}{\partial \mathbf{Q}_i} = \frac{1}{3} \sum_{T_j \supset \mathbf{Q}_i} \mathbf{A}(T_j)$$

$$\begin{aligned} \frac{\partial V}{\partial \mathbf{Q}_{H_n(i)}} &= \frac{1}{3} \sum_{T_j \supset \mathbf{Q}_{H_n(i)}} \mathbf{A}(T_j) \\ &+ \frac{\mathbf{Q}_{H_n(i)} \times \mathbf{Q}_{H_n(i+1)}}{6} + \frac{\mathbf{Q}_{H_n(i+1)} \times \mathbf{C}_n}{6} \\ &+ \frac{\mathbf{C}_n \times \mathbf{Q}_{H_n(i-1)}}{6} + \frac{\mathbf{Q}_{H_n(i-1)} \times \mathbf{Q}_{H_n(i)}}{6} \end{aligned}$$

B.3 Rotation of base vectors

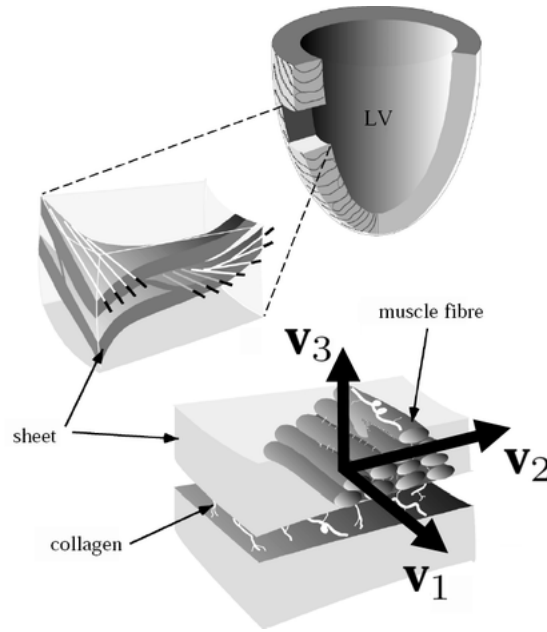


Fig. B.1.: Cardiac fiber structure. The direction $V_1 = f$ is the fiber direction ; $V_2 = s$ is the sheet direction ; $V_3 = n$ is the normal direction. Source: [LeGrice et al., 1995].

Let's note $\mathcal{E} = \{\mathbf{e}_i\}_{i \in \{1,2,3\}}$ the global base vectors in the Euclidian space. In the initial configuration, the material intrinsic base vectors is $\mathcal{E}_f = \{\mathbf{f}_i\}_{i \in \{f,s,n\}}$, following notations from Fig. B.1 with $V_1 = f$, $V_2 = s$ and $V_3 = n$.

The rotation matrix $\mathbf{\Lambda}$ expresses \mathcal{E}_f components in \mathcal{E} , stored as the column vectors matrix:

$$\mathbf{\Lambda} = [\mathbf{f}_f, \mathbf{f}_s, \mathbf{f}_n] = \begin{bmatrix} \mathbf{f}_{f_0} & \mathbf{f}_{s_0} & \mathbf{f}_{n_0} \\ \mathbf{f}_{f_1} & \mathbf{f}_{s_1} & \mathbf{f}_{n_1} \\ \mathbf{f}_{f_2} & \mathbf{f}_{s_2} & \mathbf{f}_{n_2} \end{bmatrix} \quad (\text{B.10})$$

so that $\mathbf{f}_k = \mathbf{\Lambda}_{ik} \mathbf{e}_i$.

We can ensure that the new basis \mathcal{E}_f is orthonormal:

$$\mathbf{f}_k \cdot \mathbf{f}_l = [\mathbf{\Lambda}_{ik} \mathbf{e}_i] \cdot [\mathbf{\Lambda}_{jl} \mathbf{e}_j] = \mathbf{\Lambda}_{ik} \mathbf{\Lambda}_{il} = \delta_{kl}$$

Now consider two vectors $v \in \mathcal{E}$ and $v' \in \mathcal{E}_f$ so that $v' = \mathbf{\Lambda}v$. The operator \mathbf{T} maps v to $\mathbf{T}v$ and in the rotated material frame, $\mathbf{T}' : v' \mapsto \mathbf{T}'v'$. The following defines the change of basis for second order tensors:

$$\mathbf{T}v = \mathbf{\Lambda}^T \mathbf{T}' \mathbf{\Lambda} v \quad \equiv \quad \mathbf{T}' = \mathbf{\Lambda} \mathbf{T} \mathbf{\Lambda}^T$$

Similarly, for fourth order tensors, the change of basis is defined by:

$$\mathbb{T}_{ijkl} = \mathbb{A}_{ijmn} \mathbb{T}_{mnop} \mathbb{A}_{klpq}^T \quad \text{with} \quad \mathbb{A}_{ijmn} = \mathbf{\Lambda}_{im} \mathbf{\Lambda}_{jn}$$

B.4 Notations and tensor operations

B.4.1 Second order tensor

Let \mathbf{A} be a symmetric 2nd order tensor and $\tilde{\mathbf{A}}$ its Voigt notation. We have the following notations:

$$\mathbf{A} = \begin{bmatrix} A_{11} & A_{12} & A_{13} \\ A_{21} & A_{22} & A_{23} \\ A_{31} & A_{32} & A_{33} \end{bmatrix} = \mathbf{A}_{ij} \mathbf{e}_i \otimes \mathbf{e}_j \quad \text{and} \quad \tilde{\mathbf{A}} = \begin{bmatrix} A_{11} \\ A_{22} \\ A_{33} \\ A_{23} \\ A_{13} \\ A_{12} \end{bmatrix} \quad (\text{B.11})$$

B.4.2 Forth order tensor

Let \mathbb{A} be a symmetric 4th order tensor.

$$\mathbb{A} = \begin{bmatrix} \begin{pmatrix} A_{1111} & A_{1112} & A_{1113} \\ A_{1121} & A_{1122} & A_{1123} \\ A_{1131} & A_{1132} & A_{1133} \end{pmatrix} & \begin{pmatrix} A_{1211} & A_{1212} & A_{1213} \\ A_{1221} & A_{1222} & A_{1223} \\ A_{1231} & A_{1232} & A_{1233} \end{pmatrix} & \begin{pmatrix} A_{1311} & A_{1312} & A_{1313} \\ A_{1321} & A_{1322} & A_{1323} \\ A_{1331} & A_{1332} & A_{1333} \end{pmatrix} \\ \begin{pmatrix} A_{2111} & A_{2112} & A_{2113} \\ A_{2121} & A_{2122} & A_{2123} \\ A_{2131} & A_{2132} & A_{2133} \end{pmatrix} & \begin{pmatrix} A_{2211} & A_{2212} & A_{2213} \\ A_{2221} & A_{2222} & A_{2223} \\ A_{2231} & A_{2232} & A_{2233} \end{pmatrix} & \begin{pmatrix} A_{2311} & A_{2312} & A_{2313} \\ A_{2321} & A_{2322} & A_{2323} \\ A_{2331} & A_{2332} & A_{2333} \end{pmatrix} \\ \begin{pmatrix} A_{3111} & A_{3112} & A_{3113} \\ A_{3121} & A_{3122} & A_{3123} \\ A_{3131} & A_{3132} & A_{3133} \end{pmatrix} & \begin{pmatrix} A_{3211} & A_{3212} & A_{3213} \\ A_{3221} & A_{3222} & A_{3223} \\ A_{3231} & A_{3232} & A_{3233} \end{pmatrix} & \begin{pmatrix} A_{3311} & A_{3312} & A_{3313} \\ A_{3321} & A_{3322} & A_{3323} \\ A_{3331} & A_{3332} & A_{3333} \end{pmatrix} \end{bmatrix}$$

$$= \mathbb{A}_{ijkl} \mathbf{e}_i \otimes \mathbf{e}_j \otimes \mathbf{e}_k \otimes \mathbf{e}_l$$

Fourth order rotation tensor in Voigt notation:

$$\tilde{\mathbb{A}} = \begin{bmatrix} \Lambda_{00}^2 & \Lambda_{01}^2 & \Lambda_{02}^2 & 2\Lambda_{01}\Lambda_{02} & 2\Lambda_{00}\Lambda_{02} & 2\Lambda_{00}\Lambda_{01} \\ \Lambda_{10}^2 & \Lambda_{11}^2 & \Lambda_{12}^2 & 2\Lambda_{11}\Lambda_{12} & 2\Lambda_{10}\Lambda_{12} & 2\Lambda_{10}\Lambda_{11} \\ \Lambda_{20}^2 & \Lambda_{21}^2 & \Lambda_{22}^2 & 2\Lambda_{21}\Lambda_{22} & 2\Lambda_{20}\Lambda_{22} & 2\Lambda_{20}\Lambda_{21} \\ \Lambda_{10}\Lambda_{20} & \Lambda_{11}\Lambda_{21} & \Lambda_{12}\Lambda_{22} & \Lambda_{11}\Lambda_{22} + \Lambda_{12}\Lambda_{21} & \Lambda_{10}\Lambda_{22} + \Lambda_{12}\Lambda_{20} & \Lambda_{10}\Lambda_{21} + \Lambda_{11}\Lambda_{20} \\ \Lambda_{00}\Lambda_{20} & \Lambda_{01}\Lambda_{21} & \Lambda_{02}\Lambda_{22} & \Lambda_{01}\Lambda_{22} + \Lambda_{02}\Lambda_{21} & \Lambda_{00}\Lambda_{22} + \Lambda_{02}\Lambda_{20} & \Lambda_{00}\Lambda_{21} + \Lambda_{01}\Lambda_{20} \\ \Lambda_{00}\Lambda_{10} & \Lambda_{01}\Lambda_{11} & \Lambda_{02}\Lambda_{12} & \Lambda_{01}\Lambda_{12} + \Lambda_{02}\Lambda_{11} & \Lambda_{00}\Lambda_{12} + \Lambda_{02}\Lambda_{10} & \Lambda_{00}\Lambda_{11} + \Lambda_{01}\Lambda_{10} \end{bmatrix}$$

(B.12)

B.4.3 Tensor operations

See [Ghosh et al., 2013] for a review on fourth order tensor operations.

\otimes defines the tensor product and \circ defines the Hadamard product. \mathbf{A} is a symmetric second order tensor. Here are some common operations on tensors:

- Major symmetry: $\mathbb{A}_{ijkl} = \mathbb{A}_{jilk}$
- Minor symmetry: $\mathbb{A}_{ijkl} = \mathbb{A}_{jikl} = \mathbb{A}_{ijlk}$
- Transpose: $(\mathbb{A}^T)_{ijkl} = \mathbb{A}_{klij}$

- Tensor derivative: $\left(\frac{\partial \mathbf{A}}{\partial \mathbf{B}}\right)_{ijkl} = \frac{\partial \mathbf{A}_{ij}}{\partial \mathbf{B}_{kl}}$
- Dyadic product (rank 1): $(\mathbf{u} \otimes \mathbf{v})_{ij} = u_i v_j$
- Dyadic product (rank 2): $(\mathbf{A} \otimes \mathbf{B})_{ijkl} = \mathbf{A}_{ij} \mathbf{B}_{kl}$

Additionally, the following relations are defined in [Brunet, 2020]:

$$\begin{aligned} \left(\frac{\partial \text{tr}(\mathbf{E})}{\partial \mathbf{E}}\right) &= \mathbf{I} \\ \left(\frac{\partial \mathbf{E}}{\partial \mathbf{E}}\right) &= \mathbf{I} \otimes \mathbf{I} \stackrel{\text{sym.}}{=} \mathbf{I} \bar{\otimes} \mathbf{I} \\ \left(\frac{\partial \mathbf{E}^{-1}}{\partial \mathbf{E}}\right) &= -\mathbf{E}^{-1} \otimes \mathbf{E}^{-1} \stackrel{\text{sym.}}{=} -\mathbf{E}^{-1} \bar{\otimes} \mathbf{E}^{-1} \\ \left(\frac{\partial J}{\partial \mathbf{E}}\right) &= 2 \left(\frac{\partial J}{\partial \mathbf{C}}\right) = 2 \left(\frac{1}{2} J \mathbf{C}^{-1}\right) = J \mathbf{C}^{-1} \\ \left(\frac{\partial f(\mathbf{E}) \mathbf{T}(\mathbf{E})}{\partial \mathbf{E}}\right) &= \mathbf{T}(\mathbf{E}) \otimes \frac{\partial f(\mathbf{E})}{\partial \mathbf{E}} + f(\mathbf{E}) \frac{\partial \mathbf{T}(\mathbf{E})}{\partial \mathbf{E}} \end{aligned}$$

Bibliography

- [Abraham et al., 2002] William T. Abraham et al. “Cardiac Resynchronization in Chronic Heart Failure”. In: *New England Journal of Medicine* 346.24 (2002-06), pp. 1845–1853. URL: <https://doi.org/10.1056/nejmoa013168> (cit. on p. 62).
- [Aliev et al., 1996] Rubin R. Aliev and Alexander V. Panfilov. “A simple two-variable model of cardiac excitation”. In: *Chaos, Solitons & Fractals* 7.3 (1996-03), pp. 293–301. URL: [https://doi.org/10.1016/0960-0779\(95\)00089-5](https://doi.org/10.1016/0960-0779(95)00089-5) (cit. on p. 35).
- [Allard et al., 2007] Jérémie Allard et al. “SOFA - an Open Source Framework for Medical Simulation”. In: *MMVR 15 - Medicine Meets Virtual Reality*. Vol. 125. Studies in Health Technology and Informatics. Palm Beach, United States: IOP Press, 2007-02, pp. 13–18. URL: <https://hal.inria.fr/inria-00319416> (cit. on p. 70).
- [Alnæs et al., 2014] Martin S. Alnæs et al. “Unified form language”. In: *ACM Transactions on Mathematical Software* 40.2 (2014-02), pp. 1–37. URL: <https://doi.org/10.1145/2566630> (cit. on p. 73).
- [Augustyniak, 2010] P Augustyniak. “Moving window signal concatenation for spectral analysis of ECG waves”. In: *2010 Computing in Cardiology*. 2010, pp. 665–668 (cit. on p. 41).
- [Avazmohammadi et al., 2020] Reza Avazmohammadi et al. “On the in vivo systolic compressibility of left ventricular free wall myocardium in the normal and infarcted heart”. In: *Journal of Biomechanics* 107 (2020-06), p. 109767. URL: <https://doi.org/10.1016/j.jbiomech.2020.109767> (cit. on p. 72).
- [Barber et al., 2021] Fernando Barber et al. “Estimation of Personalized Minimal Purkinje Systems From Human Electro-Anatomical Maps”. In: *IEEE Transactions on Medical Imaging* 40.8 (2021), pp. 2182–2194 (cit. on pp. 39, 100, 115).
- [Bennett et al., 2002] Jill A. Bennett et al. “Validity and reliability of the NYHA classes for measuring research outcomes in patients with cardiac disease”. In: *Heart & Lung* 31.4 (2002), pp. 262–270. URL: <https://www.sciencedirect.com/science/article/pii/S0147956302000031> (cit. on p. 11).

- [Bernardin et al., 2019] Antonin Bernardin, Christian Duriez, and Maud Marchal. “An Interactive Physically-based Model for Active Suction Phenomenon Simulation”. In: *SWS19 - SOFA Week Symposium*. Paris, France, 2019-11. URL: <https://hal.inria.fr/hal-02419381> (cit. on p. 79).
- [Berson et al., 1966] Alan S. Berson and Hubert V. Pipberger. “The low-frequency response of electrocardiographs, a frequent source of recording errors”. In: *American Heart Journal* 71.6 (1966-06), pp. 779–789. URL: [https://doi.org/10.1016/0002-8703\(66\)90599-0](https://doi.org/10.1016/0002-8703(66)90599-0) (cit. on p. 41).
- [Bestel et al., 2001] J. Bestel, Frédérique Clément, and Michel Sorine. “A Biomechanical Model of Muscle Contraction”. In: vol. 2208. 2001-10, pp. 1159–1161 (cit. on p. 72).
- [Boyden et al., 2010] Penelope A. Boyden, Masanori Hirose, and Wen Dun. “Cardiac Purkinje cells”. In: *Heart Rhythm* 7.1 (2010-01), pp. 127–135. URL: <https://doi.org/10.1016/j.hrthm.2009.09.017> (cit. on p. 6).
- [Brunet, 2020] Jean-Nicolas Brunet. “Exploring new numerical methods for the simulation of soft tissue deformations in surgery assistance”. Theses. Université de Strasbourg, 2020-11. URL: <https://hal.inria.fr/tel-03130643> (cit. on pp. 67, 69, 73, 129).
- [Brunet et al., 2019] Jean-Nicolas Brunet et al. “Physics-Based Deep Neural Network for Augmented Reality During Liver Surgery”. In: *Lecture Notes in Computer Science*. Springer International Publishing, 2019, pp. 137–145. URL: https://doi.org/10.1007/978-3-030-32254-0_16 (cit. on p. 118).
- [Buoso et al., 2021] Stefano Buoso, Thomas Joyce, and Sebastian Kozzerke. “Personalising left-ventricular biophysical models of the heart using parametric physics-informed neural networks”. In: *Medical Image Analysis* 71 (2021-07), p. 102066. URL: <https://doi.org/10.1016/j.media.2021.102066> (cit. on p. 118).
- [CAZEAU et al., 2000] S CAZEAU et al. “Multisite stimulation for correction of cardiac asynchrony”. In: *Heart* 84.6 (2000), pp. 579–581. eprint: <https://heart.bmj.com/content/84/6/579.full.pdf>. URL: <https://heart.bmj.com/content/84/6/579> (cit. on pp. 11, 12).
- [Cazeau et al., 2000] Serge Cazeau et al. “Effects of Multisite Biventricular Pacing in Patients with Heart Failure and Intraventricular Conduction Delay”. In: *New England Journal of Medicine* 344.12 (2000-03), pp. 873–880. URL: <https://doi.org/10.1056/nejm200103223441202> (cit. on pp. 12, 62).

- [Cazeau et al., 2003] S. Cazeau et al. “Echocardiographic Modeling of Cardiac Dyssynchrony Before and During Multisite Stimulation: A Prospective Study”. In: *Pacing and Clinical Electrophysiology* 26.1p2 (2003-01), pp. 137–143. URL: <https://doi.org/10.1046/j.1460-9592.2003.00003.x> (cit. on p. 62).
- [Cazeau et al., 2008] Serge J. Cazeau et al. “Responders to cardiac resynchronization therapy with narrow or intermediate QRS complexes identified by simple echocardiographic indices of dyssynchrony: The DESIRE study”. In: *European Journal of Heart Failure* 10.3 (2008-03), pp. 273–280. URL: <https://doi.org/10.1016/j.ejheart.2008.02.007> (cit. on p. 62).
- [Cazeau et al., 2019] Serge Cazeau et al. “Statistical ranking of electromechanical dyssynchrony parameters for CRT”. In: *Open Heart* 6.1 (2019), e000933 (cit. on pp. 12, 62, 95, 99, 108).
- [Cedilnik, 2018] Nicolas Cedilnik. “Fast personalized electrophysiological models from computed tomography images for ventricular tachycardia ablation planning”. In: *EP Europace* 20.suppl_3 (2018-11), pp. iii94–iii101 (cit. on pp. 25, 27).
- [Cedilnik et al., 2019] Nicolas Cedilnik and et al. “Fully Automated Electrophysiological Model Personalisation Framework from CT Imaging”. In: *FIMH 2019*. 2019, pp. 325–333 (cit. on p. 39).
- [Cha et al., 2020] Myung-Jin Cha et al. “Visualization of left ventricular Purkinje fiber distribution using widefield optical coherence microscopy”. eng. In: *International journal of clinical and experimental pathology* 13.12 (2020-12). PMC7791375[pmcid], pp. 3013–3020. URL: <https://pubmed.ncbi.nlm.nih.gov/33425102> (cit. on p. 6).
- [Chapelle et al., 2012] Dominique Chapelle et al. “An energy-preserving muscle tissue model: formulation and compatible discretizations”. In: *International Journal for Multiscale Computational Engineering* 10.2 (2012), pp. 189–211 (cit. on pp. 72, 74).
- [Chinchapatnam et al., 2008] Phani Chinchapatnam et al. “Model-Based Imaging of Cardiac Apparent Conductivity and Local Conduction Velocity for Diagnosis and Planning of Therapy”. In: *IEEE Transactions on Medical Imaging* 27.11 (2008-11), pp. 1631–1642. URL: <https://doi.org/10.1109/tmi.2008.2004644> (cit. on p. 37).
- [Clifford et al., 2006] Gari Clifford, Francisco Azuaje, and Patrick McSharry. *Advanced methods and tools for ECG data analysis*. Norwood, MA: Artech House, 2006-11 (cit. on p. 41).
- [Coevoet et al., 2017] E. Coevoet et al. “Software toolkit for modeling, simulation, and control of soft robots”. In: *Advanced Robotics* 31.22 (2017-11), pp. 1208–1224. URL: <https://doi.org/10.1080/01691864.2017.1395362> (cit. on p. 79).

- [Costa et al., 2001] K. D. Costa, J. W. Holmes, and A. D. McCulloch. “Modelling cardiac mechanical properties in three dimensions”. In: *Philosophical Transactions of the Royal Society of London. Series A: Mathematical, Physical and Engineering Sciences* 359.1783 (2001-06). Ed. by P. Kohl, D. Noble, and P. J. Hunter, pp. 1233–1250. URL: <https://doi.org/10.1098/rsta.2001.0828> (cit. on p. 73).
- [Cotin et al., 2000] Stéphane Cotin, Hervé Delingette, and Nicholas Ayache. “A Hybrid Elastic Model allowing Real-Time Cutting, Deformations and Force-Feedback for Surgery Training and Simulation”. In: *The Visual Computer* 16.8 (2000), pp. 437–452. URL: <https://hal.inria.fr/inria-00615105> (cit. on p. 62).
- [Dapogny et al., 2014] Charles Dapogny, Cécile Dobrzynski, and Pascal Frey. “Three-dimensional adaptive domain remeshing, implicit domain meshing, and applications to free and moving boundary problems”. In: *Journal of Computational Physics* (2014-04) (cit. on p. 24).
- [Daubert et al., 2017] Claude Daubert et al. “Pacing for hypertrophic obstructive cardiomyopathy: an update and future directions”. In: *EP Europace* 20.6 (2017-06), pp. 908–920. URL: <https://doi.org/10.1093/europace/eux131> (cit. on p. 55).
- [Dekker et al., 2004] A.L.A.J Dekker et al. “Epicardial left ventricular lead placement for cardiac resynchronization therapy: optimal pace site selection with pressure-volume loops”. In: *The Journal of Thoracic and Cardiovascular Surgery* 127.6 (2004-06), pp. 1641–1647. URL: <https://doi.org/10.1016/j.jtcvs.2003.10.052> (cit. on p. 88).
- [Desrues, 2022a] Gaëtan Desrues. *3D mesh analysis and visualisation, VTK helper, and more*. Version 1.95.0. 2022. URL: <https://gitlab.inria.fr/gdesrues1/meshobject> (cit. on p. 21).
- [Desrues, 2022b] Gaëtan Desrues. *Modelisation pipeline for 3D cardiac electrophysiological simulations*. Version 3.4.2. 2022. URL: <https://gitlab.inria.fr/gdesrues1/ElecModel> (cit. on p. 20).
- [Dijkstra, 1959] Edsger W Dijkstra. “A note on two problems in connexion with graphs”. In: *Numerische mathematik* 1.1 (1959), pp. 269–271 (cit. on p. 29).
- [Dobrzynski, 2012] Cecile Dobrzynski. *MMG3D: User Guide*. Technical Report RT-0422. INRIA, 2012-03. URL: <https://hal.inria.fr/hal-00681813> (cit. on p. 21).
- [Duriez, 2013] Christian Duriez. “Real-time haptic simulation of medical procedures involving deformations and device-tissue interactions”. Habilitation à diriger des recherches. Université des Sciences et Technologie de Lille - Lille I, 2013-02. URL: <https://tel.archives-ouvertes.fr/tel-00785118> (cit. on pp. 71, 79).

- [Durrer et al., 1970] Dirk Durrer et al. “Total Excitation of the Isolated Human Heart”. In: *Circulation* 41.6 (1970-06), pp. 899–912. URL: <https://doi.org/10.1161/01.cir.41.6.899> (cit. on p. 45).
- [Faure et al., 2012] François Faure et al. “SOFA: A Multi-Model Framework for Interactive Physical Simulation”. In: *Soft Tissue Biomechanical Modeling for Computer Assisted Surgery*. Ed. by Yohan Payan. Vol. 11. Studies in Mechanobiology, Tissue Engineering and Biomaterials. Springer, 2012-06, pp. 283–321. URL: <https://hal.inria.fr/hal-00681539> (cit. on p. 70).
- [Fortin et al., 2006] André Fortin and André Garon. *Les éléments Finis : de la théorie à la pratique*. <https://dms.umontreal.ca/~owens/MAT6450/elfind.pdf>. 2006 (cit. on p. 68).
- [Fries et al., 2004] Thomas-Peter Fries and Hermann Matthies. “Classification and Overview of Meshfree Methods”. en. In: *Informatik-Berichte der Technischen Universität Braunschweig* (2004), vol. 2003–03. URL: https://leopard.tu-braunschweig.de/receive/dbbs_mods_00001418 (cit. on p. 116).
- [Gao et al., 2020] Qijun Gao et al. “A new method to determine the QRS axis-QRS axis determination”. en. In: *Clin. Cardiol.* 43.12 (2020-12), pp. 1534–1538 (cit. on p. 44).
- [GHIO, 2004] S GHIO. “Interventricular and intraventricular dyssynchrony are common in heart failure patients, regardless of QRS duration”. In: *European Heart Journal* 25.7 (2004-04), pp. 571–578. URL: <https://doi.org/10.1016/j.ehj.2003.09.030> (cit. on p. 12).
- [Ghosh et al., 2013] Aurobrata Ghosh and Rachid Deriche. “4th Order Symmetric Tensors and Positive ADC Modelling”. In: *Visualization and Processing of Tensors and Higher Order Descriptors for Multi-Valued Data (Dagstuhl Seminar 11501)*. Ed. by Anna Vilanova, Carl-Fredrik Westin, and Bernhard Burgeth. Springer, 2013. URL: <https://hal.inria.fr/hal-00848513> (cit. on p. 128).
- [Giffard-Roisin, 2017] Sophie Giffard-Roisin. “Non-invasive Personalisation of Cardiac Electrophysiological Models from Surface Electrograms”. Theses. Université côte d’azur, 2017-12. URL: <https://hal.inria.fr/tel-01771476> (cit. on pp. 96, 115).
- [Giffard-Roisin et al., 2016] Sophie Giffard-Roisin et al. “Estimation of Purkinje Activation from ECG: an Intermittent Left Bundle Branch Block Study”. In: *7th International Statistical Atlases and Computational Modeling of the Heart (STACOM) Workshop, Held in Conjunction with MICCAI 2016*. Lecture Notes in Computer Science. In press. Athens, Greece, 2016-10. URL: <https://hal.inria.fr/hal-01372924> (cit. on p. 100).

- [Giffard-Roisin et al., 2017] Sophie Giffard-Roisin et al. “Noninvasive Personalization of a Cardiac Electrophysiology Model From Body Surface Potential Mapping”. In: *IEEE Transactions on Biomedical Engineering* 64.9 (2017-09), pp. 2206–2218. URL: <https://doi.org/10.1109/tbme.2016.2629849> (cit. on p. 37).
- [Gilles et al., 2013] Benjamin Gilles et al. “Frame-based interactive simulation of complex deformable objects”. In: *Deformation Models*. Ed. by Hidalgo González et al. Vol. 7. Lecture Notes in Computational Vision and Biomechanics. Springer, 2013, pp. 145–166. URL: <https://hal-lirmm.ccsd.cnrs.fr/lirmm-00806088> (cit. on p. 117).
- [Guccione et al., 1995] Julius M. Guccione, Kevin D. Costa, and Andrew D. McCulloch. “Finite element stress analysis of left ventricular mechanics in the beating dog heart”. In: *Journal of Biomechanics* 28.10 (1995-10), pp. 1167–1177. URL: [https://doi.org/10.1016/0021-9290\(94\)00174-3](https://doi.org/10.1016/0021-9290(94)00174-3) (cit. on p. 73).
- [Hansen, 2006] Nikolaus Hansen. “The CMA Evolution Strategy: A Comparing Review”. In: *Towards a New Evolutionary Computation*. Springer Berlin Heidelberg, 2006, pp. 75–102 (cit. on p. 102).
- [Heikhmakhtiar et al., 2017] Aulia Khamas Heikhmakhtiar et al. “Influence of LVAD function on mechanical unloading and electromechanical delay: a simulation study”. In: *Medical & Biological Engineering & Computing* 56.5 (2017-11), pp. 911–921. URL: <https://doi.org/10.1007/s11517-017-1730-y> (cit. on p. 83).
- [Hinton et al., 2011] Robert B. Hinton and Katherine E. Yutzey. “Heart Valve Structure and Function in Development and Disease”. In: *Annual Review of Physiology* 73.1 (2011-03), pp. 29–46. URL: <https://doi.org/10.1146/annurev-physiol-012110-142145> (cit. on p. 3).
- [Hodgkin et al., 1952] A. L. Hodgkin and A. F. Huxley. “A quantitative description of membrane current and its application to conduction and excitation in nerve”. eng. In: *The Journal of physiology* 117.4 (1952-08). PMC1392413[pmcid], pp. 500–544. URL: <https://doi.org/10.1113/jphysiol.1952.sp004764> (cit. on pp. 4, 74).
- [Holzapfel et al., 2009] Gerhard A. Holzapfel and Ray W. Ogden. “Constitutive modelling of passive myocardium: a structurally based framework for material characterization”. In: *Philosophical Transactions of the Royal Society A: Mathematical, Physical and Engineering Sciences* 367.1902 (2009-09), pp. 3445–3475. URL: <https://doi.org/10.1098/rsta.2009.0091> (cit. on p. 72).

- [Hwang et al., 2011] Min-Sig Hwang et al. “Non-invasive visualization of the complete cardiac conduction system using magnetic resonance microscopy”. In: *Journal of Cardiovascular Magnetic Resonance* 13.S1 (2011-02). URL: <https://doi.org/10.1186/1532-429x-13-s1-m1> (cit. on p. 6).
- [Jadczyk et al., 2021] Tomasz Jadczyk et al. “Local electromechanical alterations determine the left ventricle rotational dynamics in CRT-eligible heart failure patients”. In: *Scientific Reports* 11.1 (2021-02). URL: <https://doi.org/10.1038/s41598-021-82793-1> (cit. on p. 89).
- [Jokic et al., 1970] S. Jokic et al. “Efficient ECG Modeling using Polynomial Functions”. In: *Elektronika ir Elektrotechnika* 110.4 (1970-01), pp. 121–124. URL: <https://doi.org/10.5755/j01.eee.110.4.304> (cit. on p. 41).
- [Jolly et al., 2012] Marie-Pierre Jolly et al. “Automatic Segmentation of the Myocardium in Cine MR Images Using Deformable Registration”. In: *Statistical Atlases and Computational Models of the Heart. Imaging and Modelling Challenges*. Springer Berlin Heidelberg, 2012, pp. 98–108. URL: https://doi.org/10.1007/978-3-642-28326-0_10 (cit. on p. 14).
- [Karraz et al., 2006] G. Karraz and G. Mages. “Automatic Classification of Heartbeats using Neural Network Classifier based on a Bayesian Framework”. In: *2006 International Conference of the IEEE Engineering in Medicine and Biology Society*. IEEE, 2006-08. URL: <https://doi.org/10.1109/iembs.2006.259356> (cit. on p. 41).
- [Kashtanova et al., 2022] Victoriya Kashtanova et al. “APHYN-EP: Physics-based deep learning framework to learn and forecast cardiac electrophysiology dynamics”. In: *STACOM 2022 - 13th Workshop on Statistical Atlases and Computational Modelling of the Heart*. Singapore, Singapore, 2022-09. URL: <https://hal.inria.fr/hal-03894974> (cit. on p. 118).
- [Kawel et al., 2012] Nadine Kawel et al. “Normal Left Ventricular Myocardial Thickness for Middle-Aged and Older Subjects With Steady-State Free Precession Cardiac Magnetic Resonance”. In: *Circulation: Cardiovascular Imaging* 5.4 (2012), pp. 500–508. eprint: <https://www.ahajournals.org/doi/pdf/10.1161/CIRCIMAGING.112.973560>. URL: <https://www.ahajournals.org/doi/abs/10.1161/CIRCIMAGING.112.973560> (cit. on p. 21).
- [Klabunde, 2012] Richard E. Klabunde. *Cardiovascular physiology concepts*. 2nd ed. Includes bibliographical references and index. Philadelphia, PA: Lippincott Williams & Wilkins/Wolters Kluwer, 2012 (cit. on p. 6).

- [Kosta et al., 2021] Sarah Kosta and Pierre C. Dauby. “Frank-Starling mechanism, fluid responsiveness, and length-dependent activation: Unravelling the multiscale behaviors with an in silico analysis”. In: *PLOS Computational Biology* 17.10 (2021-10). Ed. by Alison L. Marsden, e1009469. URL: <https://doi.org/10.1371/journal.pcbi.1009469> (cit. on pp. 6, 35).
- [Kuhtz-Buschbeck et al., 2018] Johann P. Kuhtz-Buschbeck et al. “Rediscovery of Otto Frank’s contribution to science”. In: *Journal of Molecular and Cellular Cardiology* 119 (2018-06), pp. 96–103. URL: <https://doi.org/10.1016/j.yjmcc.2018.04.017> (cit. on p. 78).
- [Kurapati et al., 2022] Rahul Kurapati, Joseph Heaton, and David R. Lowery. *Atrial Kick*. StatPearls Publishing, Treasure Island (FL), 2022. URL: <http://europepmc.org/books/NBK482421> (cit. on p. 77).
- [Land et al., 2015] Sander Land et al. “Verification of cardiac mechanics software: benchmark problems and solutions for testing active and passive material behaviour”. In: *Proceedings of the Royal Society A: Mathematical, Physical and Engineering Sciences* 471.2184 (2015-12), p. 20150641. URL: <https://doi.org/10.1098/rspa.2015.0641> (cit. on p. 73).
- [LeGrice et al., 1995] I. J. LeGrice et al. “Laminar structure of the heart: ventricular myocyte arrangement and connective tissue architecture in the dog”. In: *American Journal of Physiology-Heart and Circulatory Physiology* 269.2 (1995-08), H571–H582. URL: <https://doi.org/10.1152/ajpheart.1995.269.2.h571> (cit. on p. 126).
- [Liu et al., 2002] Lili Liu et al. “Left ventricular resynchronization therapy in a canine model of left bundle branch block”. In: *American Journal of Physiology-Heart and Circulatory Physiology* 282.6 (2002-06), H2238–H2244. URL: <https://doi.org/10.1152/ajpheart.00684.2001> (cit. on p. 88).
- [Liu et al., 2021] Hao Liu et al. “The impact of myocardial compressibility on organ-level simulations of the normal and infarcted heart”. In: *Scientific Reports* 11.1 (2021-06). URL: <https://doi.org/10.1038/s41598-021-92810-y> (cit. on pp. 72, 76).
- [Lorensen et al., 1987] William E. Lorensen and Harvey E. Cline. “Marching cubes: A high resolution 3D surface construction algorithm”. In: *Proceedings of the 14th annual conference on Computer graphics and interactive techniques - SIGGRAPH '87*. ACM Press, 1987. URL: <https://doi.org/10.1145/37401.37422> (cit. on p. 21).
- [Lorenz et al., 2006] Cristian Lorenz and Jens von Berg. “A comprehensive shape model of the heart”. In: *Medical image analysis* 10.4 (2006), pp. 657–670 (cit. on p. 24).

- [Maki et al., 2019] Atsuo Maki et al. “Application of optimal control theory based on the evolution strategy (CMA-ES) to automatic berthing”. In: *Journal of Marine Science and Technology* 25.1 (2019-05), pp. 221–233. URL: <https://doi.org/10.1007/s00773-019-00642-3> (cit. on p. 102).
- [Malmivuo et al., 1995] Jaakko Malmivuo and Robert Plonsey. *Bioelectromagnetism - Principles and Applications of Bioelectric and Biomagnetic Fields*. 1995-10 (cit. on pp. 5, 6, 39).
- [Manuel D Cerqueira et al., 2002] and Manuel D. Cerqueira et al. “Standardized Myocardial Segmentation and Nomenclature for Tomographic Imaging of the Heart”. In: *Circulation* 105.4 (2002-01), pp. 539–542. URL: <https://doi.org/10.1161/hc0402.102975> (cit. on p. 27).
- [Marchesseau, 2013] Stéphanie Marchesseau. “Simulation de modèles personnalisés du coeur pour la prédiction de thérapies cardiaques”. Theses. Ecole Nationale Supérieure des Mines de Paris, 2013-01. URL: <https://pastel.archives-ouvertes.fr/pastel-00820082> (cit. on pp. 70, 73).
- [Marchesseau et al., 2012] Stéphanie Marchesseau et al. “Fast Parameter Calibration of a Cardiac Electromechanical Model from Medical Images based on the Unscented Transform”. In: *Biomechanics and Modeling in Mechanobiology* (2012), pp. 1–17. URL: <https://hal.inria.fr/hal-00813847> (cit. on p. 44).
- [Martin et al., 2010] Sebastian Martin et al. “Unified simulation of elastic rods, shells, and solids”. In: *ACM Transactions on Graphics* 29.4 (2010-07), pp. 1–10. URL: <https://doi.org/10.1145/1778765.1778776> (cit. on pp. 116, 117).
- [Martinez-Diaz et al., 2008] Jorge Martinez-Diaz et al. “Quick method for mean frontal QRS axis determination”. In: *Boletin de la Asociacion Medica de Puerto Rico* 100.4 (2008), pp. 19–24. URL: <http://europepmc.org/abstract/MED/19400525> (cit. on p. 44).
- [Martinez et al., 2018] Marine E. Martinez et al. “Role of the Purkinje-Muscle Junction on the Ventricular Repolarization Heterogeneity in the Healthy and Ischemic Ovine Ventricular Myocardium”. In: *Frontiers in Physiology* 9 (2018-06). URL: <https://doi.org/10.3389/fphys.2018.00718> (cit. on pp. 6, 37).
- [Mazier et al., 2022] Arnaud Mazier et al. *SONICS: Develop intuition on biomechanical systems through interactive error controlled simulations*. 2022. URL: <https://arxiv.org/abs/2208.11676> (cit. on p. 73).
- [Meurer et al., 2017] Aaron Meurer et al. “SymPy: symbolic computing in Python”. In: *PeerJ Computer Science* 3 (2017-01), e103. URL: <https://doi.org/10.7717/peerj-cs.103> (cit. on p. 73).

- [Mirebeau et al., 2019] Jean-Marie Mirebeau and Jorg Portegies. “Hamiltonian Fast Marching: A numerical solver for anisotropic and non-holonomic eikonal PDEs”. In: *Image Processing On Line* 9 (2019), pp. 47–93. URL: <https://hal.science/hal-01778322> (cit. on p. 36).
- [Mirsky, 1973] I Mirsky. “Ventricular and arterial wall stresses based on large deformation analyses”. en. In: *Biophys. J.* 13.11 (1973-11), pp. 1141–1159 (cit. on p. 62).
- [Mitchell, 2003] C Mitchell. “A two-current model for the dynamics of cardiac membrane”. In: *Bulletin of Mathematical Biology* 65.5 (2003-09), pp. 767–793 (cit. on pp. 35, 39, 40).
- [Mitra et al., 2007] M. Mitra and S. Mitra. “A Software Based Approach for Detection of QRS Vector of ECG Signal”. In: *3rd Kuala Lumpur International Conference on Biomedical Engineering 2006*. Ed. by Fatimah Ibrahim et al. Berlin, Heidelberg: Springer Berlin Heidelberg, 2007, pp. 348–351 (cit. on p. 44).
- [Mohammadi et al., 2016] Shabnam Mohammadi et al. “Study of the normal heart size in Northwest part of Iranian population: a cadaveric study”. In: *Journal of Cardiovascular and Thoracic Research* 8.3 (2016-09), pp. 119–125. URL: <https://doi.org/10.15171/jcvtr.2016.25> (cit. on p. 2).
- [Mollero, 2017] Roch Mollero. “Robust personalisation of 3D electromechanical cardiac models. Application to heterogeneous and longitudinal clinical databases”. Theses. COMUE Université Côte d’Azur (2015 - 2019), 2017-12. URL: <https://theses.hal.science/tel-01737200> (cit. on pp. 14, 103).
- [Molléro et al., 2019] Roch Molléro et al. “Population-based priors in cardiac model personalisation for consistent parameter estimation in heterogeneous databases”. In: *International Journal for Numerical Methods in Biomedical Engineering* 35.2 (2019-02), e3158. URL: <https://hal.inria.fr/hal-01922719> (cit. on p. 94).
- [Morgan et al., 1990] JP Morgan et al. “Abnormal intracellular calcium handling, a major cause of systolic and diastolic dysfunction in ventricular myocardium from patients with heart failure”. In: *Circulation* 81.2 Suppl (1990-02), pp. III21–32. URL: <http://europepmc.org/abstract/MED/2153479> (cit. on p. 10).
- [Munawar et al., 2018] Dian A. Munawar et al. “Predicted longevity of contemporary cardiac implantable electronic devices: A call for industry-wide “standardized” reporting”. In: *Heart Rhythm* 15.12 (2018). Focus Issue: Devices, pp. 1756–1763. URL: <https://www.sciencedirect.com/science/article/pii/S1547527118307215> (cit. on p. 54).

- [Nacif et al., 2011] Marcelo Souto Nacif et al. "Cardiac magnetic resonance imaging and its electrocardiographs (ECG): tips and tricks". In: *The International Journal of Cardiovascular Imaging* 28.6 (2011-10), pp. 1465–1475. URL: <https://doi.org/10.1007/s10554-011-9957-4> (cit. on p. 41).
- [Oliveira et al., 2016] Bernardo Lino De Oliveira and Joakim Sundnes. "COMPARISON OF TETRAHEDRAL AND HEXAHEDRAL MESHES FOR FINITE ELEMENT SIMULATION OF CARDIAC ELECTROMECHANICS". In: *Proceedings of the VII European Congress on Computational Methods in Applied Sciences and Engineering (ECCOMAS Congress 2016)*. Institute of Structural Analysis and Antiseismic Research School of Civil Engineering National Technical University of Athens (NTUA) Greece, 2016. URL: <https://doi.org/10.7712/100016.1801.9193> (cit. on p. 22).
- [Pekar et al., 2001] Vladimir Pekar et al. "Shape-model-based adaptation of 3D deformable meshes for segmentation of medical images". In: *Medical Imaging 2001: Image Processing*. Vol. 4322. SPIE. 2001, pp. 281–289 (cit. on p. 24).
- [Pfaller et al., 2018] Martin R. Pfaller et al. "The importance of the pericardium for cardiac biomechanics: from physiology to computational modeling". In: *Biomechanics and Modeling in Mechanobiology* 18.2 (2018-12), pp. 503–529. URL: <https://doi.org/10.1007/s10237-018-1098-4> (cit. on p. 80).
- [Pheiffer et al., 2017] Thomas Pheiffer et al. "Estimation of Local Conduction Velocity from Myocardium Activation Time: Application to Cardiac Resynchronization Therapy". In: *Functional Imaging and Modelling of the Heart*. Ed. by Mihaela Pop and Graham A Wright. Cham: Springer International Publishing, 2017, pp. 239–248 (cit. on p. 37).
- [Rehman et al., 2021] Ibraheem Rehman, Ali Nassereddin, and Afzal Rehman. "Anatomy, Thorax, Pericardium". eng. In: *StatPearls*. Treasure Island (FL): StatPearls Publishing, 2021-07. URL: <https://pubmed.ncbi.nlm.nih.gov/29489245> (cit. on p. 3).
- [Ribeiro et al., 2020] Antônio H. Ribeiro et al. "Automatic diagnosis of the 12-lead ECG using a deep neural network". In: *Nature Communications* 11.1 (2020-04). URL: <https://doi.org/10.1038/s41467-020-15432-4> (cit. on pp. 15, 16, 51).
- [Ricciardi et al., 2016] Danilo Ricciardi et al. "Impact of the high-frequency cutoff of bandpass filtering on ECG quality and clinical interpretation: A comparison between 40Hz and 150Hz cutoff in a surgical preoperative adult outpatient population". In: *Journal of Electrocardiology* 49.5 (2016-09), pp. 691–695. URL: <https://doi.org/10.1016/j.jelectrocard.2016.07.002> (cit. on p. 41).

- [Rocklin, 2015] Matthew Rocklin. “Dask: Parallel Computation with Blocked algorithms and Task Scheduling”. In: *Proceedings of the 14th Python in Science Conference*. Ed. by Kathryn Huff and James Bergstra. 2015, pp. 130–136 (cit. on p. 103).
- [Rodero et al., 2021] Cristobal Rodero et al. *Virtual cohort of 1000 synthetic heart meshes from adult human healthy population*. en. 2021. URL: <https://zenodo.org/record/4506930> (cit. on pp. 15, 22).
- [Sahli Costabal et al., 2016] Francisco Sahli Costabal, Daniel E. Hurtado, and Ellen Kuhl. “Generating Purkinje networks in the human heart”. In: *Journal of Biomechanics* 49.12 (2016). Cardiovascular Biomechanics in Health and Disease, pp. 2455–2465. URL: <https://www.sciencedirect.com/science/article/pii/S0021929015007332> (cit. on pp. 6, 27).
- [Saxton et al., 2021] Anthony Saxton, Muhammad Ali Tariq, and Bruno Bordon. “Anatomy, Thorax, Cardiac Muscle”. eng. In: *StatPearls*. Treasure Island (FL): StatPearls Publishing, 2021-08. URL: <https://pubmed.ncbi.nlm.nih.gov/30570976> (cit. on p. 3).
- [Schroeder et al., 2006a] Will Schroeder, William E Lorensen, and Kenneth W Martin. *The visualization toolkit : an object-oriented approach to 3D graphics*. 4th ed. Kitware, 2006 (cit. on p. 21).
- [Schroeder et al., 2006b] Will Schroeder, Ken Martin, and Bill Lorensen. *The Visualization Toolkit: An object-oriented approach to 3D graphics*. en. Ingram, 2006 (cit. on p. 21).
- [Scroggs et al., 2022] Matthew W. Scroggs et al. “Construction of Arbitrary Order Finite Element Degree-of-Freedom Maps on Polygonal and Polyhedral Cell Meshes”. In: *ACM Transactions on Mathematical Software* 48.2 (2022-05), pp. 1–23. URL: <https://doi.org/10.1145/3524456> (cit. on p. 73).
- [Sengupta et al., 2008] Partho P. Sengupta et al. “Twist Mechanics of the Left Ventricle”. In: *JACC: Cardiovascular Imaging* 1.3 (2008-05), pp. 366–376. URL: <https://doi.org/10.1016/j.jcmg.2008.02.006> (cit. on p. 89).
- [Serge, 2000] Cazeau Serge. “Multisite stimulation for correction of cardiac asynchrony”. In: *Heart* 84.6 (2000-12), pp. 579–581. URL: <https://doi.org/10.1136/heart.84.6.579> (cit. on p. 11).
- [Sermesant et al., 2007] Maxime Sermesant et al. “An anisotropic multi-front fast marching method for real-time simulation of cardiac electrophysiology”. In: *Proceedings of Functional Imaging and Modeling of the Heart 2007 (FIMH’07)*. Vol. 4466. LNCS. no address, United States, 2007, pp. 160–169. URL: <https://hal.inria.fr/inria-00616051> (cit. on p. 36).

- [Sermesant et al., 2012] M. Sermesant et al. “Patient-specific electromechanical models of the heart for the prediction of pacing acute effects in CRT: A preliminary clinical validation”. In: *Medical Image Analysis* 16.1 (2012-01), pp. 201–215. URL: <https://doi.org/10.1016/j.media.2011.07.003> (cit. on p. 39).
- [Shaffer et al., 2014] Fred Shaffer, Rollin McCraty, and Christopher L. Zerr. “A healthy heart is not a metronome: an integrative review of the heart’s anatomy and heart rate variability”. In: *Frontiers in Psychology* 5 (2014-09). URL: <https://doi.org/10.3389/fpsyg.2014.01040> (cit. on p. 2).
- [Spodick et al., 2008] David H. Spodick, Mary Frisella, and Sirin Apiyassawat. “QRS Axis Validation in Clinical Electrocardiography”. In: *The American Journal of Cardiology* 101.2 (2008-01), pp. 268–269. URL: <https://doi.org/10.1016/j.amjcard.2007.07.069> (cit. on p. 44).
- [Streeter et al., 1969] Daniel D. Streeter et al. “Fiber Orientation in the Canine Left Ventricle during Diastole and Systole”. In: *Circulation Research* 24.3 (1969), pp. 339–347 (cit. on p. 26).
- [Taber et al., 1996] Larry A. Taber, Ming Yang, and W. William Podszus. “Mechanics of ventricular torsion”. In: *Journal of Biomechanics* 29.6 (1996-06), pp. 745–752. URL: [https://doi.org/10.1016/0021-9290\(95\)00129-8](https://doi.org/10.1016/0021-9290(95)00129-8) (cit. on p. 89).
- [Talbot et al., 2013] Hugo Talbot et al. “Towards an Interactive Electromechanical Model of the Heart”. In: *Interface Focus*. The Virtual Physiological Human: Integrative Approaches to Computational Biomedicine 3.2 (2013-04), p. 4. URL: <https://hal.inria.fr/hal-00797354> (cit. on pp. 36, 39).
- [Tusscher et al., 2004] K. H. W. J. ten Tusscher et al. “A model for human ventricular tissue”. In: *American Journal of Physiology-Heart and Circulatory Physiology* 286.4 (2004-04), H1573–H1589. URL: <https://doi.org/10.1152/ajpheart.00794.2003> (cit. on p. 35).
- [Tusscher et al., 2008] K.H.W.J. Ten Tusscher and A.V. Panfilov. “Modelling of the ventricular conduction system”. In: *Progress in Biophysics and Molecular Biology* 96.1-3 (2008-01), pp. 152–170. URL: <https://doi.org/10.1016/j.pbiomolbio.2007.07.026> (cit. on p. 39).
- [Wallman et al., 2012] Mikael Wallman, Nicolas P. Smith, and Blanca Rodriguez. “A Comparative Study of Graph-Based, Eikonal, and Monodomain Simulations for the Estimation of Cardiac Activation Times”. In: *IEEE Transactions on Biomedical Engineering* 59.6 (2012-06), pp. 1739–1748. URL: <https://doi.org/10.1109/tbme.2012.2193398> (cit. on p. 36).

- [Wang et al., 2012] Yang Wang et al. “Learning-Based Detection and Tracking in Medical Imaging: A Probabilistic Approach”. In: *Deformation Models*. Springer Netherlands, 2012-10, pp. 209–235. URL: https://doi.org/10.1007/978-94-007-5446-1_9 (cit. on p. 14).
- [Watkins et al., 1993] Matthew W. Watkins and Martin M. LeWinter. “Physiologic Role of the Normal Pericardium”. In: *Annual Review of Medicine* 44.1 (1993). PMID: 8476238, pp. 171–180. eprint: <https://doi.org/10.1146/annurev.me.44.020193.001131>. URL: <https://doi.org/10.1146/annurev.me.44.020193.001131> (cit. on p. 4).
- [Westerhof et al., 2009] Nico Westerhof, Jan-Willem Lankhaar, and Berend E. Westerhof. “The arterial Windkessel”. In: *Medical & Biological Engineering & Computing* 47.2 (2009-02), pp. 131–141. URL: <https://doi.org/10.1007/s11517-008-0359-2> (cit. on p. 78).
- [Wriggers, 2008] Peter Wriggers. *Nonlinear finite element methods*. en. 2008th ed. Berlin, Germany: Springer, 2008-11 (cit. on p. 68).
- [Yang et al., 1991] Ming Yang and Larry A. Taber. “The possible role of poroelasticity in the apparent viscoelastic behavior of passive cardiac muscle”. In: *Journal of Biomechanics* 24.7 (1991), pp. 587–597. URL: [https://doi.org/10.1016/0021-9290\(91\)90291-t](https://doi.org/10.1016/0021-9290(91)90291-t) (cit. on p. 72).
- [Yezzi et al., 2003] A.J. Yezzi and J.L. Prince. “An Eulerian PDE approach for computing tissue thickness”. In: *IEEE Transactions on Medical Imaging* 22.10 (2003), pp. 1332–1339 (cit. on p. 25).
- [Yingchoncharoen et al., 2013] Teerapat Yingchoncharoen et al. “Normal Ranges of Left Ventricular Strain: A Meta-Analysis”. In: *Journal of the American Society of Echocardiography* 26.2 (2013), pp. 185–191. URL: <https://www.sciencedirect.com/science/article/pii/S0894731712007997> (cit. on p. 62).
- [Zettinig et al., 2014] Oliver Zettinig et al. “Data-driven estimation of cardiac electrical diffusivity from 12-lead ECG signals”. In: *Medical Image Analysis* 18.8 (2014). Special Issue on the 2013 Conference on Medical Image Computing and Computer Assisted Intervention, pp. 1361–1376. URL: <https://www.sciencedirect.com/science/article/pii/S1361841514000656> (cit. on p. 37).